

TURBULENT THERMAL CONVECTION IN A CELL
WITH ROUGH UPPER AND LOWER SURFACES

By

YIBING DU

Bachelor of Science
Tianjin University
Tianjin, China
1985

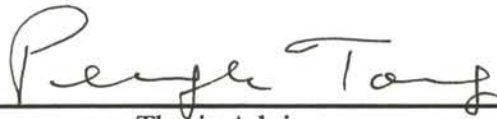
Master of Science
Tianjin University
Tianjin, China
1988

Submitted to the Faculty of the
Graduate College of the
Oklahoma State University
In partial fulfillment of
the requirements for
the Degree of
DOCTOR OF PHILOSOPHY
December, 1999

Thesis
1999D
D812t

TURBULENT THERMAL CONVECTION IN A CELL
WITH ROUGH UPPER AND LOWER SURFACES

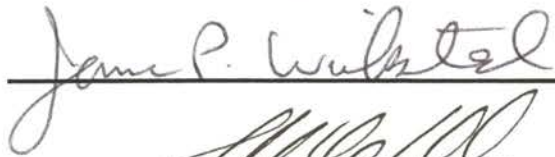
Thesis Approved:



Thesis Adviser











Dean of the Graduate College

ACKNOWLEDGMENTS

In writing this dissertation, I have been fortunate to receive support and assistance from many people. I wish to express my deep appreciation to them.

I would like to express my greatest gratitude to my thesis advisor Dr. Penger Tong, for his guidance, encouragement, assistance and support. During those years in the lab, he has been teaching me how to think as a physicist while helping me to learn many experimental techniques and writing skills. I am truly grateful to have the opportunity to work with him. It is a wonderful and rewarding experience for me. I am also profoundly thankful to the rest of my thesis committee: Dr. B. J. Ackerson, Dr. F. W. Chambers, Dr. H. L. Scott, and Dr. J. Wicksted, for helping me make my study plans and giving me insightful suggestions for my research work.

I have benefited tremendously from all the co-workers in our group. I thank George Kambouroglou for years of nice collaboration. Thanks also go to Xi Ye, Jiangquan Zhang, and Yixue Du for their help. I am also thankful to Mr. Mike Lucas and his team for fabricating the convection cells.

I wish to express my gratitude to everyone in this department for the great education I received at OSU. Thanks to Dr. X. Xie, Dr. J. H. Perk, and Dr. P. Westhaus, for their warm-hearted help to my academic career and to my life.

Special thanks go to my husband, Shenghong Yao. His love, patience and support help me through the most difficult times. His suggestions and criticism on my research work benefit me greatly. I can not express my appreciation for him enough in words.

I am extremely grateful for the love and support from my family on the other side of the earth. My parents, both are physics teachers, led me to the wonder world of physics. For all the years, they hold up and practice their ideal of pursuing knowledge and pass it onto their daughters. Their encouragement, expectation and trust have been a great inspiration in my whole life. I dedicate this thesis to my parents, Yuemin Du and Peizhi Huang.

TABLE OF CONTENTS

Chapter	Page
I. INTRODUCTION.....	1
II. BACKGROUND	5
2.1 Rayleigh-Benard convection	5
2.2 Nusselt number, Reynolds number and thermal boundary layers	9
2.3 Recent theoretical models	11
2.4 Recent experimental results	14
III. EXPERIMENTAL METHODS.....	16
3.1 Convection cells.....	16
3.2 Calibration of the temperature probes	22
3.3 Experimental setup	24
3.4 Data acquisition	26
3.5 Flow visualization.....	27
IV. BOUNDARY LAYER MEASUREMENTS AND FLOW VISUALIZATION.....	30
4.1 Heat transport measurements and flow visualization	30
4.2 Local temperature fluctuations and their histograms.....	42
4.3 Temperature profiles near the upper surface	51
V. TEMPERATURE FLUCTUATIONS AT THE CELL CENTER.....	66
5.1 Local temperature fluctuations and their statistics.....	66
5.2 Frequency power spectrum of temperature fluctuations.....	83
5.3 Energy dissipation in turbulent convection.....	90
VI. SUMMARY.....	95
BIBLIOGRAPHY.....	99

LIST OF FIGURES

Figure	Page
3.1 Thermal convection cells with smooth and rough surfaces	16
3.2 Cross-section of the lower plate	17
3.3 The structure of the top plate (cooling chamber)	20
3.4 Two lateral positions of the movable thermistor in the rough cell	21
3.5 A typical calibration curve for a thermistor	23
3.6 Temperature fluctuations of the top and bottom plates at $Ra = 2.8 \times 10^9$	25
3.7 Schematic diagram of the optical set-up for flow visualization measurements ...	29
4.1 Measured $NuRa$ as a function of Ra in the smooth and rough cells	31
4.2 (a) Sketch of the flow field near the upper rough surface. (b) A typical streak image of the TLC spheres taken near the cold rough surface at $Ra = 2.6 \times 10^9$	35
4.3 A streak image of the TLC spheres taken near the cold smooth surface at $Ra = 2.6 \times 10^9$	36
4.4 A streak image of the TLC spheres taken near the cold rough surface at $Ra = 2.6 \times 10^9$	37
4.5 A time sequence of the TLC particle images illustrating the eruption process of a thermal plume in the smooth cell at $Ra = 2.6 \times 10^9$	40

4.6	A time sequence of the TLC particle images illustrating the eruption process of a thermal plume in the rough cell at $Ra = 2.6 \times 10^9$	41
4.7	Typical time series measurements of temperature fluctuations near the upper (cold) plate in the smooth and rough cells.....	43
4.8	Comparison of the temperature histograms between the smooth and rough cells	44
4.9	Time series measurements of temperature fluctuations at the position V and position T	47
4.10	Comparison of the temperature histograms at the position V and position T	48
4.11	Measured temperature histograms at different values of z	49
4.12	Measured mean temperature profile $T(z)$ in the smooth cell and in the rough cell at the position V	52
4.13	Measured mean temperature profile $T(z)$ in the smooth cell and in the rough cell at the position T.....	53
4.14	Sketch of the thermal boundary layer near the rough surface	55
4.15	(a) Measured temperature profile $T(z)$ as a function of z/δ for three different values of Ra in the smooth cell. (b) Measured temperature profile $T(z)$ as a function of z for three different values of Ra in the rough cell at the position T.....	57
4.16	Measured temperature profile $T(z)$ as a function of z/δ for three different values of Ra in the rough cell at the position V.....	58
4.17	Measured boundary layer thickness in the smooth and rough cells.....	60

4.18	(a) Measured RMS temperature profile $T_{RMS}(z)$ in the smooth cell and in the rough cell at the position T with $Ra = 1.5 \times 10^9$. (b) Measured RMS temperature profile $T_{RMS}(z)$ in the smooth cell and in the rough cell at the position V with $Ra = 1.5 \times 10^9$	61
4.19	Measured $T_{RMS}(z)$ in the smooth cell and in the rough cell at the position T and position V for different values of Ra	63
5.1	Typical time series measurements of temperature fluctuations at the center of the A=1 smooth and rough cells	67
5.2	(a) Measured $H(\delta T)$ at the center of the A=1 smooth cell. (b) Measured $H(\delta T)$ as a function of $\delta T/\sigma$ for different values of Ra at the center of the A=1 smooth cell	68
5.3	Comparison of the temperature histograms between the A=1 smooth cell and the A=1 rough cell	70
5.4	Measured temperature histogram $H(\delta T)$ as a function of $\delta T/\sigma$ for different values of Ra at the center of the A=1 rough cell	71
5.5	(a) A streak image of the seeded TLC spheres taken in the A=1 rough cell.	74
5.5	(b) A streak image of the seeded TLC spheres taken in the A=1 smooth cell	75
5.6	Typical time series measurements of the temperature fluctuations at the center of the A=0.5 smooth cell and the A=0.5 rough cell	76
5.7	(a) Measured temperature histogram $H(\delta T)$ as a function of $\delta T/\sigma$ for different values of Ra at the center of the A=0.5 smooth cell. (b) Measured $H(\delta T)$ as a function of $(\delta T/\sigma)^{1.5}$ in the A=0.5 smooth cell	77

5.8	Comparison of the temperature histograms between the A=0.5 smooth cell and the A=0.5 rough cell.....	80
5.9	Measured temperature histogram $H(\delta T)$ as a function of $\delta T/\sigma$ for different values of Ra at the center of the A=0.5 rough cell.....	81
5.10	Normalized RMS value $\sigma/\Delta T$ as a function of Ra in the smooth and rough cells.....	82
5.11	(a) Measured power spectrum $P(f)$ as a function of f for three different values of Ra at the center of the A= 1 smooth cell. (b) Plots of $P(f)$ as a function of $f^{0.6}$ for the same data.	85
5.12	(a) Measured power spectrum $P(f)$ as a function of f for three different values of Ra at the center of the A= 0.5 smooth cell. (b) Plots of $P(f)$ as a function of $f^{0.6}$ for the same data.	86
5.13	Comparison of the power spectra in the A=1 smooth cell and in the A=1 rough cell	88
5.14	Measured power spectrum $P(f)$ as a function of f for three different values of Ra at the center of the A=1 rough cell. (b) Plots of $P(f)$ as a function of $f^{0.6}$ for the same data	89
5.15	(a) Cut-off frequency f_c as a function of Ra in the smooth cells and in the rough cells. (b) Normalized cut-off frequency $f_c H^2/\kappa$ as a function of Ra	92

CHAPTER I

INTRODUCTION

Turbulent flows over a rough surface are ubiquitous in nature. An example is convection in the atmosphere and oceans, where the underlying surfaces are almost always rough. The study of turbulence over a rough surface is of fundamental interest for understanding the structure and dynamics of turbulent boundary layers and is also relevant to many practical applications, ranging from effective heat transfer for a reentry vehicle to turbulent drag reduction of a commercial aircraft. Our current knowledge about the roughness effect on turbulent flows comes largely from experiments in wind tunnels and other open systems [1], where the disturbance flow produced by a rough wall is confined in the near-wall region and is quickly discharged to the down stream. Because of these reasons the surface roughness usually does not perturb the turbulent bulk region very much, and its effect can often be described by rescaling the relevant parameters with the surface roughness height k [2]. This situation makes the experimental study of turbulent boundary layers very difficult, because the coherent structures detached from the boundary layers are transient and their dynamics is vary fast. This is changed completely for flows in a closed cell, in which the disturbances produced by the boundaries are mixed into the turbulent bulk region. Turbulent Rayleigh-Benard convection is an example of such a closed system, which is an ideal system for the study of the boundary layer dynamics. Temperature as a scalar field can be measured and

visualized readily with high spatial and temporal resolutions. Moreover, the local temperature and flow visualization can be performed simultaneously, together with an accurate determination of the heat transport across the cell.

Turbulent Rayleigh-Benard convection has attracted much attention in recent years [3]. The discovery of scaling laws in the heat transport and the temperature statistics in Rayleigh-Benard convection [4, 5, 6] has stimulated many experimental [7-16], numerical [17-20], and theoretical [5, 21, 3] efforts aimed at explaining, verifying, and finding new scaling laws in the temperature and velocity fields. An important scaling law found in the so-called hard turbulence regime ($Ra > 10^8$) is that the normalized heat flux, or the Nusselt number Nu , scales with the Rayleigh number Ra as $Nu \sim Ra^{2/7}$. The experiment carried out by the Chicago group [4, 5] using helium gas at low temperature confirmed the significant deviation from the classical $Ra^{1/3}$ scaling, which was predicted by early theories [22, 23]. There are two salient features in turbulence convection. The first is the large scale circulation that spans the height of the convection cell and the second is intermittent bursts of thermal plumes from the thermal boundary layers [3]. These features are directly related to the transport of heat and momentum across the cell and have been adopted in several theoretical models [3] to explain the observed scaling laws in the heat flux and temperature statistics [4, 5]. While different theoretical models arrive at similar conclusions for the $Ra^{2/7}$ scaling, they have different assumptions and predictions for the velocity field in the turbulent bulk region and near the boundary.

A main issue of an unresolved theoretical debate is to understand whether the heat transport in turbulent convection is determined primarily by thermal plumes or by the large-scale circulation [3]. Recent experiments have shown that the $Ra^{2/7}$ scaling is a

robust and general feature of turbulent convection and is insensitive to details of the flow field in the convection cell. The $Ra^{2/7}$ scaling is found to remain unchanged under a variety of perturbations, such as horizontal shearing of a boundary layer [7, 8], vertical rotation of the whole convection cell [24], alteration of the large-scale circulation by introducing bluff obstacles on the conducting plate [25] and side wall [26], and changing the working fluids with different Prandtl numbers [13, 14, 25]. The $Ra^{2/7}$ scaling is also observed in a side-heated convection cell [27]. These experiments indicate that the heat transport in turbulent convection is controlled by the local dynamics near the thermal boundary layers and the current theory seems to be too restrictive in explaining the observed scaling laws.

To find the real mechanism of turbulent heat transport, it becomes important to alter the boundary conditions of the convection cell and to see how the structure and dynamics of the thermal boundary layers change with the boundary conditions. In this thesis, I present results of a novel convection experiment, which is carried out in a cell with rough upper and lower surfaces. The measured heat flux across the rough cell is found to be increased by more than 76%, when the Rayleigh number Ra becomes much larger than a transition value Ra_0 . Flow visualization and local temperature measurements reveal new dynamics for the emission of the thermal plumes. The experiment shows that the interaction between the horizontal shear flow (due to the large-scale circulation) and the rough surface creates a secondary flow (eddies) in the groove region. This secondary flow together with the large-scale circulation enhance the detachment of the thermal boundary layer from the tip of the rough elements. The extra thermal plumes detached from the rough surfaces are responsible for the enhanced heat transport. The striking

effect of the surface roughness provides new insights into the role played by the thermal plumes in determining the heat transport in turbulent convection. The discovery of the enhanced heat transport in the rough cell has important applications in engineering, geography, and meteorology. Understanding heat transport phenomena in thermal convection will shed new light on technological improvements for more efficient heat transfer in various industrial applications.

The remaining parts of the thesis are organized as follows. Chapter II provides a brief review on the recent theoretical and experimental developments of turbulent thermal convection. Experimental details are described in Chapter III. Chapter IV summarizes our boundary layer measurements and flow visualization results. Temperature measurements at the center of the cell are discussed in Chapter V. Finally, the work is summarized in Chapter VI.

CHAPTER II

THEORETICAL BACKGROUND

In this chapter I first give some background information on Rayleigh-Benard convection and then briefly review the recent theoretical and experimental developments of turbulent thermal convection.

2.1 Rayleigh-Benard Convection

Rayleigh-Benard convection is named after two scientists, Benard and Rayleigh, who studied thermal convection at the beginning of this century. Benard's experiment [28] was the first controlled study of thermal convection and Lord Rayleigh conducted the first theoretical analysis [29].

In a typical convection experiment, a closed cell filled with a fluid is heated from below and the top surface of the cell is kept at a constant temperature. The side-wall of the cell does not transfer any heat. Heat is continuously supplied at the bottom plate and a constant temperature difference ΔT is maintained across the cell. When ΔT is small, the heat can be transferred through the fluid by thermal conduction and the fluid does not move at all. When the temperature difference ΔT exceeds a critical value ΔT_c , Rayleigh-Benard convection will occur. In thermal convection the primary driving force is buoyancy. The cooler fluid at the top of the cell has a slightly larger density and tends to move downward under gravity. The warmer fluid at the bottom, on the other hand, has a

smaller density and can move upward. Once the fluid starts to move, the heat will be transported predominantly by convection.

In Rayleigh-Benard convection, the motion of the fluid can be described by the following equations:

Incompressibility equation:

$$\nabla \cdot \mathbf{v} = 0 \quad (2.1)$$

Momentum equation:

$$\left(\frac{\partial \mathbf{v}}{\partial t} + \mathbf{v} \cdot \nabla \mathbf{v} \right) = -\nabla p / \rho_0 + \nu \nabla^2 \mathbf{v} - \alpha \delta T g \hat{z} \quad (2.2)$$

Heat diffusion equation:

$$\frac{\partial T}{\partial t} + \mathbf{v} \cdot \nabla T = \kappa_d \nabla^2 T + \Phi \quad (2.3)$$

In the above, $\mathbf{v}(\vec{\mathbf{r}}, t)$, $p(\vec{\mathbf{r}}, t)$, and $T(\vec{\mathbf{r}}, t)$ are, respectively, the unknown velocity, pressure, and temperature fields, ρ_0 is the density of the fluid, g is the gravitational acceleration, ν is the kinematic viscosity of the fluid, $\alpha = \frac{1}{\rho} \frac{\partial \rho}{\partial T}$ is the thermal expansion coefficient, $\Delta T = T_{bottom} - T_{top}$ is the temperature difference between the top and bottom plates, and δT is the temperature fluctuation from the mean. The vertical coordinate is denoted as \hat{z} with the positive direction pointing downwards. The thermal diffusivity is given by $\kappa_d \equiv \frac{\chi}{\rho_0 C_p}$, where χ is the thermal conductivity and C_p is the heat capacity of the fluid. In Eq. (2.3), Φ is the dissipation function for the internally generated heat due to the viscous stress.

In deriving Eqs. (2.1) to (2.3), we have used the Boussinesq approximation [30], under which all the fluid properties, except for the density ρ , are assumed to be temperature independent. The time averaged density variation is small when compared with the density itself, and is neglected in all terms of the equations except for the buoyancy term. Equation (2.1) is obtained from the mass conservation equation, $\frac{\partial \rho}{\partial t} + \nabla \cdot (\rho \mathbf{v}) = 0$, simplified under the Boussinesq approximation. Equation (2.2) is the usual Navier-Stokes equation with a buoyancy force $-\alpha \delta T g \hat{z}$. The dissipation function Φ in Eq. (2.3) is negligible in our experiment.

Using the temperature difference ΔT , the cell height H , and the thermal diffusion time H^2/κ_d as the scaling variables for the temperature T , the length \mathbf{r} and the time t , Eqs. (2.1) - (2.3) can be written in the dimensionless form:

$$\nabla \cdot \mathbf{v} = 0 \quad (2.4)$$

$$\frac{1}{Pr} \left(\frac{\partial \mathbf{v}}{\partial t} + \mathbf{v} \cdot \nabla \mathbf{v} + \nabla p \right) = \nabla^2 \mathbf{v} - Ra \hat{z} \quad (2.5)$$

$$\frac{\partial T}{\partial t} + \mathbf{v} \cdot \nabla T = \nabla^2 T \quad (2.6)$$

In the above, the Rayleigh number Ra is defined as

$$Ra = \frac{g \alpha H^3 \Delta T}{\nu \kappa_d}, \quad (2.7)$$

and the Prandtl number is

$$Pr = \frac{\nu}{\kappa_d}. \quad (2.8)$$

It is seen from Eqs. (2.4) - (2.6) that the fluid parameters enter the convection problem only through two dimensionless parameters Ra and Pr . Different fluids with the same

values of Ra and Pr will show similar flow behavior, because the solutions for the velocity, temperature, and pressure fields depend only on these two parameters.

We now discuss the boundary conditions for the above equations. On the top and bottom plates as well as the side-wall, the flow velocity must be zero (no-slip condition): $\mathbf{v}_{sidewalls} = \mathbf{v}_{plates} = 0$. The temperature on the top ($z=0$) and bottom ($z=1$) plates is held constant: $T|_{z=0} = T_{top} = -1/2$; $T|_{z=1} = T_{bottom} = 1/2$. Because there is no heat flux going through the side-wall, the temperature gradient normal to the side-wall is zero: $(\hat{n} \cdot \nabla T)_{sidewall} = 0$. The geometry of the cell is specified by the aspect ratio A , which is the ratio of the lateral extent of the cell to the cell height H . In our experiment, the cell is cylindrical and $A \equiv \frac{Diameter}{H}$.

The Rayleigh number and the Prandtl number can be understood in terms of the buoyancy and diffusion. The time scale for the buoyancy force to move a fluid element from the lower plate to the upper plate is $\tau_b = \left(\frac{H}{g\alpha\Delta T} \right)^{\frac{1}{2}}$. The corresponding thermal diffusion time is $\tau_t = \frac{H^2}{\kappa_d}$, and the viscous diffusion time is $\tau_v = \frac{H^2}{\nu}$. The Rayleigh number Ra can be expressed as the time ratio of the two diffusion contributions to the buoyancy contribution:

$$Ra = \frac{\tau_t \tau_v}{\tau_b^2}. \quad (2.9)$$

The Prandtl number Pr can be written as the ratio of the thermal diffusion time to the viscous diffusion time,

$$\text{Pr} = \frac{\tau_t}{\tau_v}. \quad (2.10)$$

When Ra is small, the buoyancy force is not enough to overcome the viscous dissipation and thermal diffusions, and the fluid will remain stationary. When Ra is increased to a value above the critical Rayleigh number $Ra \approx 2 \times 10^3$, thermal convection will occur. As Ra is further increased, the flow will go through several transitions and become turbulent at $Ra \sim 3 \times 10^5$ [31].

2.2 Nusselt Number, Reynolds Number and Thermal Boundary Layers

In convection experiments, the Rayleigh number Ra and the Prandtl number Pr are the controlled parameters. There are two additional parameters, which are not controlled but reflect the responses of the fluid. The Nusselt number Nu , which measures the efficiency of the heat transport by convection, is defined as the ratio of the total heat flux, q_{total} , transported through the cell to the pure conductive heat flux q_{cond} :

$$Nu = \frac{q_{total}}{q_{cond}} = \frac{q_{total}}{k\Delta T / H}, \quad (2.11)$$

where k is the thermal conductivity of the fluid. The Reynolds number Re , which characterizes the velocity field, is defined as

$$Re = \frac{u_c H}{\nu}, \quad (2.12)$$

where u_c is a characteristic velocity in the convection cell.

In turbulent convection, the applied temperature difference across the cell is concentrated in two thin layers of the fluid adjacent to the top and bottom surfaces. In the central region of the cell, the temperature is homogenized by turbulent mixing. Near the

boundary, heat is transported primarily by conduction and one can show [11] that Nu is related to the thermal boundary thickness δ by:

$$Nu = \frac{H}{2\delta}. \quad (2.13)$$

Using a scaling argument [22, 23], one can write

$$\delta \sim H Ra^{-\beta}. \quad (2.14)$$

When Ra is large enough, δ should be a new length scale independent of the cell height H . This implies that $\beta = \frac{1}{3}$ because $Ra \sim H^3$. From Eqs. (2.13) and (2.14), we obtain the classic scaling relation for Nu :

$$Nu \sim Ra^\beta, \quad (2.15)$$

with $\beta = \frac{1}{3}$.

Many experimental studies have been carried out to examine the Ra dependence of the Nusselt number. In 1987, the Chicago group [4] conducted precise heat transport measurements using low temperature helium gas as a working fluid. They found that the convective flow undergoes a transition at $Ra \approx 4 \times 10^7$. When Ra is in the range between 5×10^5 and 4×10^7 , the flow is in the “soft-turbulence” regime and the measured Nu scales with $Ra^{\frac{1}{3}}$. When $Ra > 4 \times 10^7$, the flow changes to a “hard-turbulence” state and the measured $Nu \sim Ra^{\frac{2}{7}}$. They also found that the probability density function (PDF) of temperature fluctuations at the center of the cell changes its form when Ra is increased above 4×10^7 . In the soft turbulence regime, the temperature PDF is of Gaussian form. In the hard turbulence regime, however, the temperature PDF becomes a simple exponential function.

2.3 Recent Theoretical Models

There are two important features, which are found to coexist in a closed convection cell [32]. One is the coherent large-scale circulation, which produces a “wind” near the boundaries of the cell. The other is the intermittent burst of thermal plumes from the thermal boundary layers. While several theoretical models have been proposed to explain the scaling relation $N_u \sim Ra^{\frac{2}{7}}$, they have different assumptions and predictions for the velocity field in the turbulent bulk region and near the viscous and thermal boundary layers. Some models emphasize the effect of the thermal plumes on the heat transport, whereas others suggest that the large-scale circulation plays a dominant role in the turbulent heat transport.

Kadanoff and his coworkers proposed a scaling model, which involves the thermal plumes but ignores the large-scale circulation [5]. They assumed that the thermal plumes across the central region have a characteristic velocity u_c and a temperature difference Δ_c . Therefore, the heat flux across the cell is:

$$Q \sim u_c \Delta_c \sim Ra^\beta \quad (2.16)$$

It is further assumed that there is a mixing zone in between the thermal boundary layer and the central region, in which the thermal plumes break off from the boundary layer and accelerate to a terminal velocity u_c in the central region. This mixing zone is much thicker than the boundary layer but is thin when compared with the height of the cell. The terminal velocity u_c is obtained by balancing the viscous force ($\sim u_c \nu / \delta^2$) with the buoyancy force ($\sim g \alpha \Delta T$). Therefore, we have

$$u_c \sim \frac{g \alpha \Delta T \delta^2}{\nu}. \quad (2.17)$$

In the central region, the molecular diffusion for the heat and the momentum diffusion is small and can be ignored when compared with the turbulent mixing and drag. Using a simple dimensional argument, one can show that the characteristic velocity is [5]:

$$u_c \sim (\alpha g \Delta_c H)^{\frac{1}{2}} \quad (2.18)$$

The characteristic velocity u_c and the temperature difference Δ_c are all assumed to scale with Ra:

$$\frac{\Delta_c}{\Delta T} \sim Ra^\gamma \quad (2.19)$$

$$\frac{u_c H}{\nu} \sim Ra^\varepsilon \quad (2.20)$$

From (2.14)-(2.20), one finds that the scaling exponents obey the following relations:

$$\beta = \varepsilon + \gamma, \quad (2.21)$$

$$\varepsilon = 1 - 2\beta, \quad (2.22)$$

$$\varepsilon = \frac{1}{2}(1 + \gamma). \quad (2.23)$$

The solutions for these equations are: $\beta=2/7$, $\gamma=-1/7$, and $\varepsilon=3/7$.

In the model proposed by Shraiman and Siggia [21], the heat transport is assumed to be determined solely by the large-scale circulation near the thermal and viscous boundary layers. Their analysis is valid when the thermal boundary layer is submerged underneath the viscous sublayer for $Pr > 1$. By averaging the heat equation (2.6) with the insulating lateral boundaries, the Nusselt number is found to be related to the thermal dissipation:

$$Nu \equiv \langle v_z T \rangle_A - \partial_z \langle T \rangle_A = \langle (\nabla T)^2 \rangle_\nu, \quad (2.24)$$

where $\langle \rangle_A$ and $\langle \rangle_V$ denote averages over a plane with $z=const$ and the entire volume.

Because the flow is entirely buoyancy driven, averaging the equation for the total energy

$(\mathbf{v}^2 / 2 - zTRaPr)$ yields

$$\langle (\nabla \mathbf{v})^2 \rangle = (Nu - 1)Ra. \quad (2.25)$$

Within the viscous sublayer, the mean flow has a linear profile $u_x = z/\tau$ with $0 \leq z \ll 1$

and $u_z \sim O(zu_x)$. For a unit-aspect-ratio cell, the Nusselt number then can be computed

from Eq. (2.6):

$$Nu \sim 1/\delta \sim \tau^{-1/3}. \quad (2.26)$$

Here δ is the thermal boundary layer thickness. Shraiman and Siggia assume that the

velocity boundary layer near the conducting plates has a typical log profile similar to that

in a turbulent boundary layer, and is given by

$$v(z) = u^* (2.5 \ln(z/z^*) + 6.0) \quad (2.27)$$

with $z^* = Pr/u^*$. The characteristic velocity u^* is related to the large-scale Reynolds

number by

$$u^* = Pr Re / [2.5 \ln(Re) + 6.0]. \quad (2.28)$$

Under these approximations, Shraiman and Siggia obtain the following scaling relations:

$$Nu \sim Pr^{-1/7} Ra^{2/7}, \quad (2.29)$$

$$Re \sim Pr^{-5/7} Ra^{3/7} [2.5 \ln(Re) + 6.0]. \quad (2.30)$$

Although the assumptions for the heat transport are completely different from those used

by Kadanoff and coworkers, the solutions for the scaling exponents β and ε remain the

same.

2.4 Recent Experimental Results

The main difference between the two theoretical models discussed in Sec. 2.3 is whether the heat transport in turbulent convection is determined primarily by the thermal plumes or by the larger-scale circulation. Many experiments have been carried out recently aimed at examining the real mechanism of the heat transport. Various alterations to the boundary layer or to the large-scale circulation were introduced in order to see how the heat transport is affected.

Solomon and Gollub placed the convecting fluid over a layer of mercury which was driven electromagnetically to provide a moving boundary layer [8]. Recirculating large-scale flow is enhanced artificially near the lower boundary layer and the Nusselt number Nu is found to increase as much as 70%. The experiment supports the idea that the non-classical scaling relation of Nu with Ra is due to the advection of heat from the boundary layers by the large-scale flows.

In the experiment carried out by Ke-Qing Xia and Siu-Lung Lui [26], staggered fingers are put on the sidewall of a convection cell. It is found that the large-scale flow pattern is modified to a distorted asymmetric four-roll circulation. The temperature probability density function (PDF) at the cell center is changed to a double-peaked function, which can be fitted by the superposition of two Gaussians. However, the heat transport across the cell is found to be the same.

Shen and Tong have conducted a convection experiment in a closed cell with rough upper and lower surfaces [33, 34]. The heat flux is found to be increased by ~20%, when the Rayleigh number becomes larger than a transition value. Light scattering is used to examine the velocity fluctuations at the cell center and the results reveal that the main

effect of the surface roughness is to increase the emission of thermal plumes. In this thesis, flow visualization and systematic temperature measurements are performed in order to further investigate the surface roughness effect. The results reveal that the interaction between the large-scale circulation and the surface roughness creates a secondary flow (eddies) inside the grooves. This secondary flow together with the large-scale circulation enhance the detachment of the thermal boundary layer near the tip of the rough elements and produce more thermal plumes.

CHAPTER III
EXPERIMENTAL METHODS

3.1 Convection Cells

The experiment is conducted in a vertical cylindrical cell filled with water. Figure 3.1 shows the sketch of the smooth and rough cells used in the experiment. The side-wall of the cells is made of a transparent Plexiglas ring with an inner diameter of 20cm. Two Plexiglas rings with the same diameter but having two different heights of 20cm and 40cm are used, respectively, to extend the Rayleigh number range. The corresponding aspect ratios ($A=\text{diameter}/\text{height}$) are 1.0 and 0.5. The top and bottom plates are made of brass and are electroplated with a thin layer of gold on their surfaces to prevent corrosion.

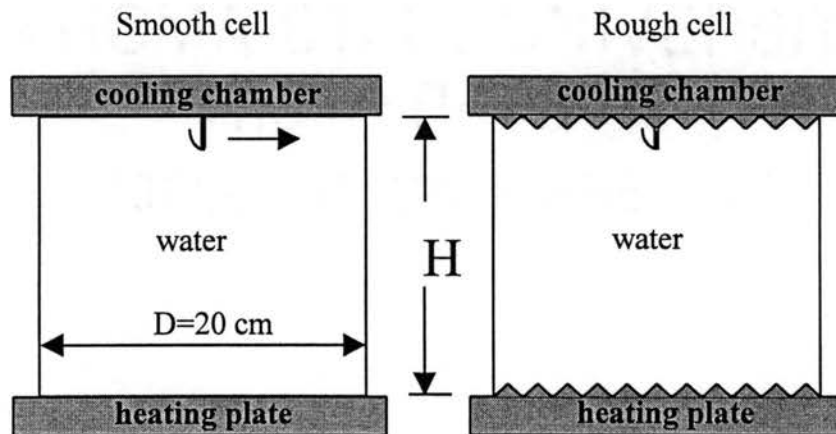


Figure 3.1 Thermal convection cells with smooth and rough surfaces.

Two silicone rubber film heaters (Omega, SRF 7/10) are connected in parallel and sandwiched on the backside of the bottom plate to provide a constant and uniform heating (see Fig.3.2). The electric resistance of each heater is $33.4\ \Omega$. A DC power supply (Sorenson DCS 150-7) with a 0.1% long-term stability is used to provide the heating power. The voltage applied to the heaters varies from 20V to 90V, and the corresponding heating power is in the range between 24W and 485W. To record the temperature of each plate, we embed a thermistor beneath the surface of each plate. The thermistor has a room temperature resistance of 5 KOhms (Omega 44034) and is located near the center of the plate.

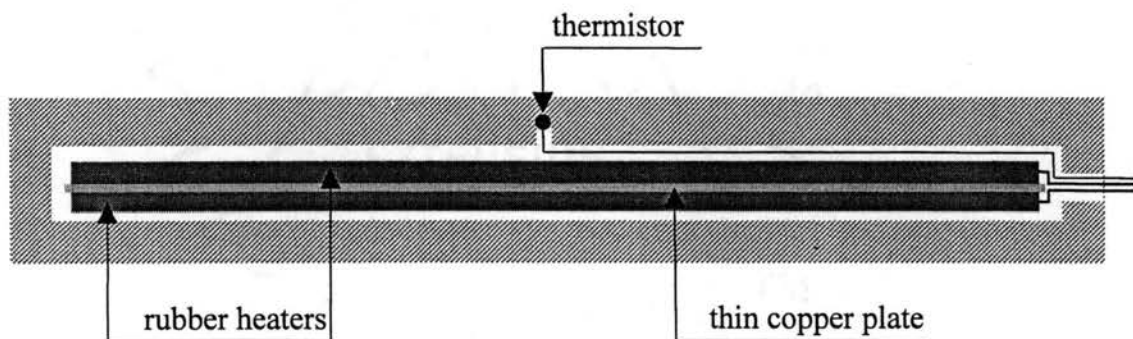


Figure 3.2. Cross-section of the lower plate.

The upper side of the top plate is in contact with a cooling chamber (see Fig.3.3), whose temperature is maintained by circulating cold water from a temperature-controlled bath/circulator (NESLAB RTE-110). The temperature stability of the circulator is within 0.01°C . To further increase the cooling power of the whole flow system, a flow-through cooler (NESLAB FTC 350A) is connected in series to the down stream side of the cooling chamber. As shown in Fig. 3.3, cold water is fed into the cooling chamber

through two opposing inlets on the side of the chamber and flows out of the chamber through two outlets on the top of the chamber.

As shown in Fig. 3.1, the two convection cells are identical except one has smooth upper and lower surfaces (“smooth cell”) and the other has rough upper and lower surfaces (“rough cell”). To facilitate the construction of the rough cell, we fabricate a pair of identical rough surfaces from two separate brass plates and then attach them firmly on to the smooth top and bottom plates by small screws. Care has been taken to ensure that the smooth side of each rough plate is in good thermal contact with the substrate. The rough surface is made by woven V-shaped grooves and each of them has a vertex angle of 90° . The spacing between the grooves is such that a square lattice of pyramids is formed on the surface. The height of the pyramids (the roughness height h) is 9.0 mm and their spacing is $2h$. To compare the heat transport measurements, we also use another pair of rough surfaces which have the same surface structure but the roughness height is $h=3.2\text{mm}$. The height of the Plexiglas rings used for the rough cell is adjusted slightly, so that the base-to-base distance between the two opposing rough surfaces is the same as the height of the corresponding smooth cells. To measure accurately the temperature of the rough surfaces, we embed two additional thermistors (Omega 44034) on each rough plate.

A small movable thermistor (Thermometrics, AB6E3-B10KA202J) is installed inside the cell in order to measure the temperature of the convecting fluid as a function of distance z from the upper (cold) plate. A thin stainless tube of diameter 1.1mm is installed through the center of the cooling chamber to guide the temperature probe and

the connecting wires into the cell. The tube is mounted on a micrometer-controlled translation stage so that the local temperature $T(z)$ of the fluid can be measured as a function of the distance z with an accuracy of 0.2mm. In the rough cell, we measure the temperature profile $T(z)$ at two different lateral positions. As shown in Fig. 3.4, one position is directly below the tip of a central pyramid (“position T”) and the other is inside the “valley” in between the two crossing grooves at the center of the top plate (“position V”). The response time of the thermistor probe is 13ms.

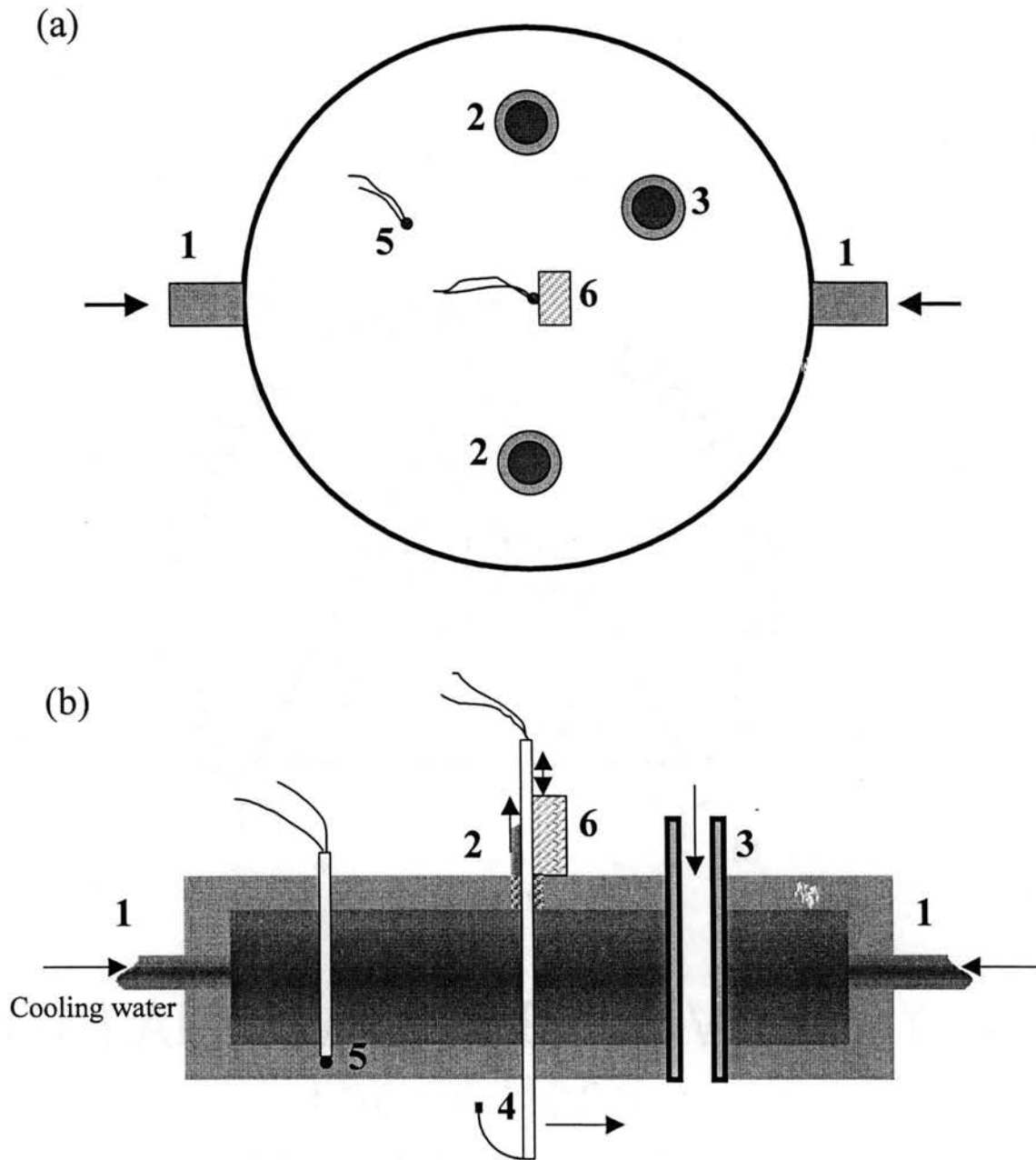


Figure 3.3. The structure of the top plate (cooling chamber): (a) top view, (b) side view (cross-section). 1. Inlet, 2. Outlet, 3. Filling tube, 4. Movable thermistor assembly, the horizontal arrow indicates the flow direction of the large-scale circulation, 5. Top plate thermistor, 6. Translation stage.

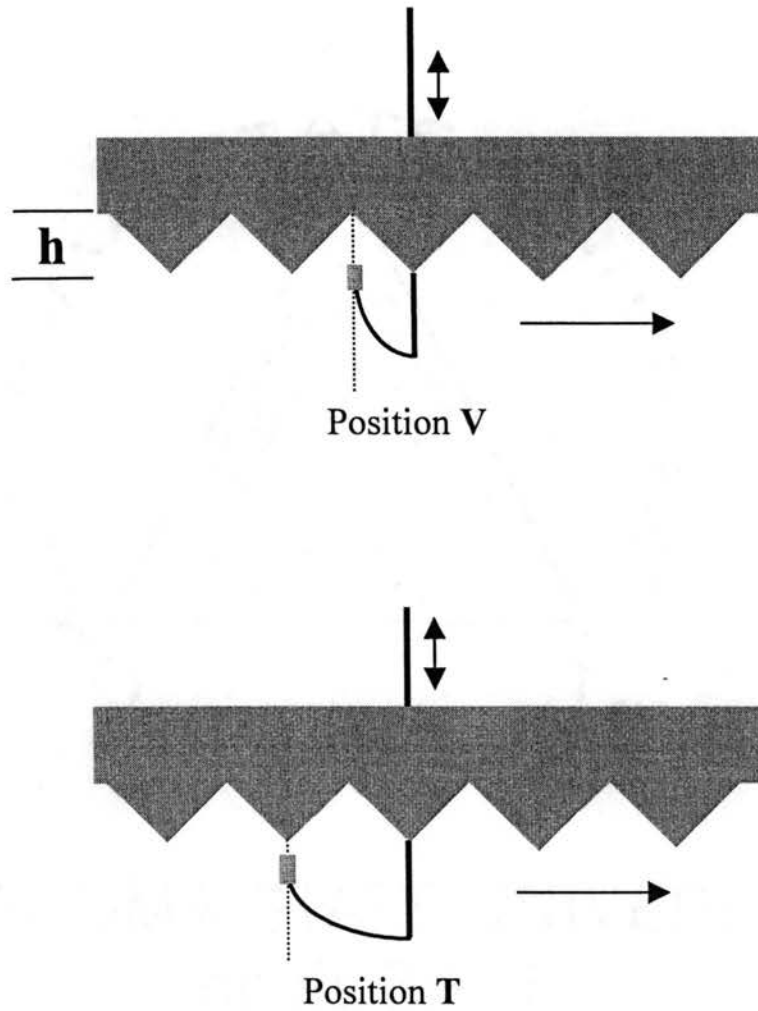


Figure 3.4 Two lateral positions of the movable thermistor in the rough cell. The horizontal arrows indicate the direction of the local flow.

3.2 Calibration of the temperature probes

All the thermistors used in the experiment are calibrated individually. A water bath (NESLAB RTE-211), with a long term temperature stability of 0.01°C is used for the calibration. During the calibration, a precision thermometer (YSI 4600) with an accuracy of 0.01°C is used to read the temperature of the water bath. The corresponding resistance of each thermistor is then recorded. Figure 3.5 shows a typical calibration curve for a thermistor. The solid circles are the measured resistance values at each temperature and the solid line is the fitting curve using the Steinhart-Hart equation: [35]

$$\frac{1}{T} = A + B \ln R + C(\ln R)^3,$$

where T is the temperature in Kelvin degrees, R is the resistance of the thermistor, A , B , and C are fitting parameters. This equation is used to convert the measured resistance to the local temperature, once the thermistor is calibrated.

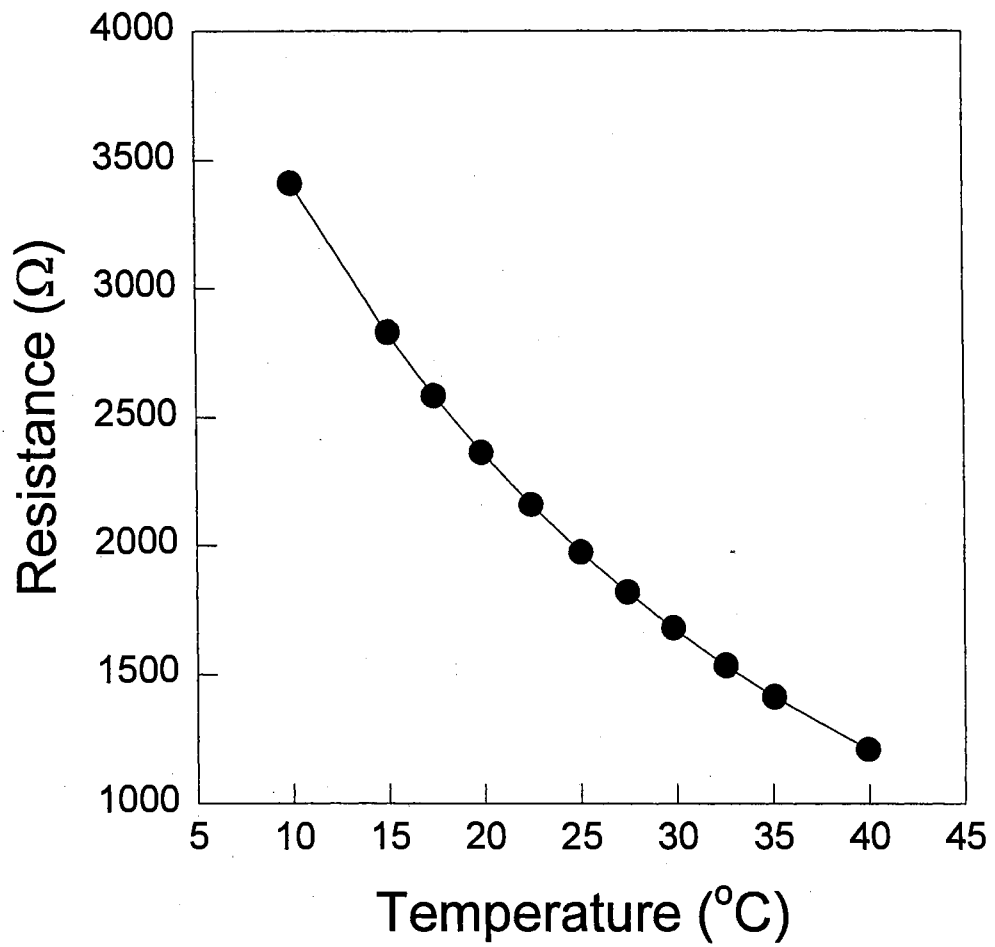


Figure 3.5 A typical calibration curve of a thermistor.

3.3 Experimental setup

Distilled water is used as the convecting fluid and is filled into the cell through a filling tube of 9.3 mm in diameter (see Fig.3.3). To eliminate air bubbles in the cell, we first degas water by setting the temperature of the top plate at room temperature and the heating power supply at 90V, which is the highest voltage used in the experiment. As the temperature of water increases, air bubbles appear gradually on the bottom plate. We shake the cell and force the bubbles to rise to the top plate. We then add water and let the bubbles come out of the cell from the filling tube. This procedure lasts about one day. The voltage of the power supply is then decreased gradually to 20V, which is the lowest voltage used in the experiment. As the temperature decreases, the volume of water is reduced and more water is added to ensure that no air bubble gets into the cell from the filling tube. With the degas procedure, all the bubbles are removed from the cell and they will not reappear later when a higher voltage (up to 90V) is used in the experiment.

The whole convection cell is then wrapped by three layers of thermal insulating rubber sheets to reduce the heat exchange with the surrounding environment. In this way, all the heat produced by the heaters attached to the bottom plate is transferred through water to the top plate. The vertical heat flux is then calculated from the electric power required to keep the lower plate at a constant temperature. In the experiment, the temperature difference between the top and bottom plates varies between 4°C and 50°C depending on the heating power. By adjusting the temperature of the cooling water, we maintain the temperature of the bulk fluid at 30°C ($\pm 1^\circ\text{C}$) for all the measurements (see Fig 4.13 for the temperature profile of the fluid). The corresponding Prandtl number of

the fluid is approximately 5.4. Figure 3.6 shows the temperature stability of the top and bottom plates. It is seen that the system is stable and the temperature fluctuation is within ± 0.5 °C (the standard deviation is less than 0.1°C), which is less than 3% of the temperature difference ΔT .

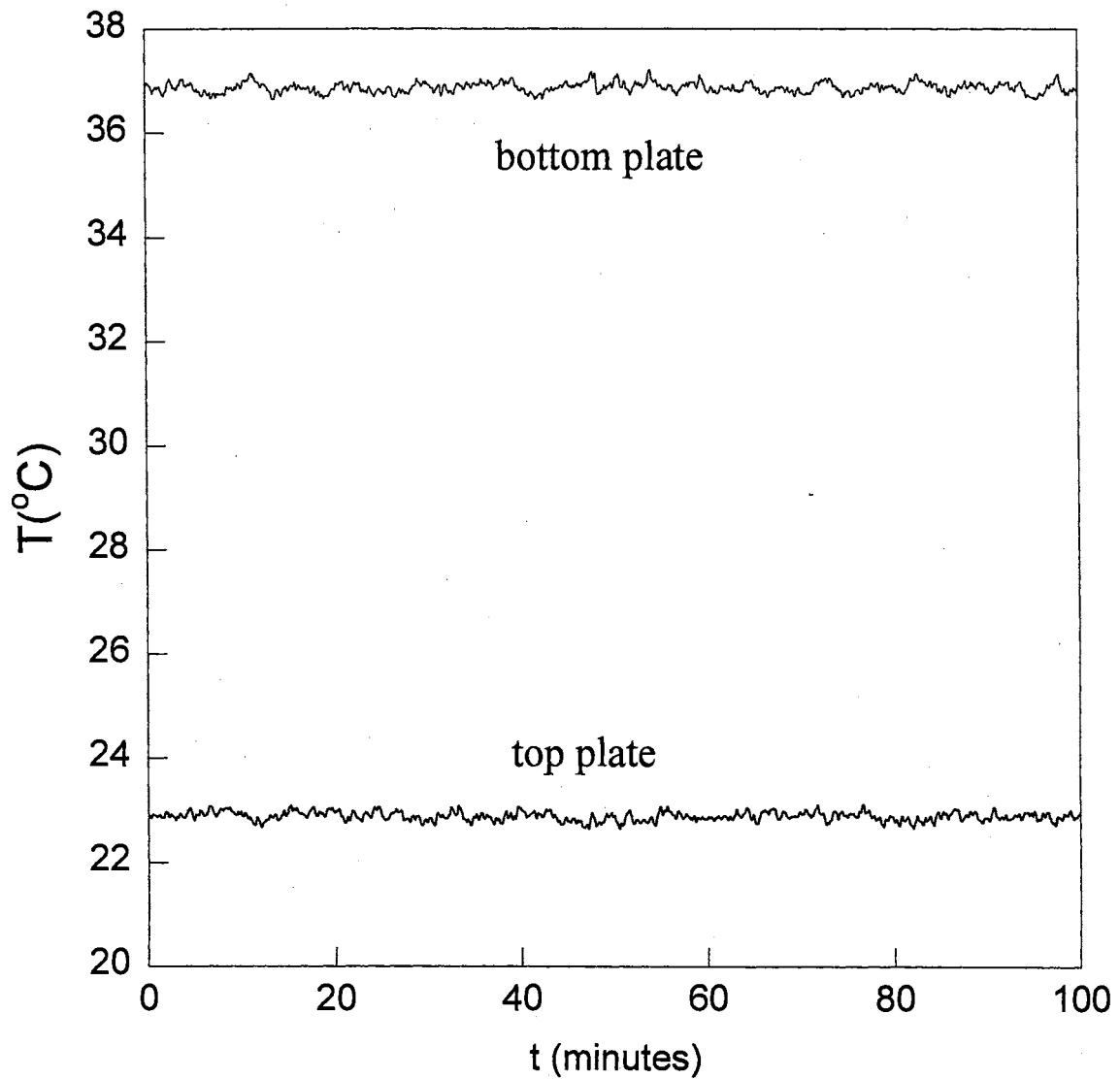


Figure 3.6 Temperature fluctuations of the top and bottom plates at $Ra = 2.8 \times 10^9$.

3.4 Data Acquisition

KEITHLEY Model 2001 and Model 199 digital multimeters are used to measure the resistance of the thermistors. A National Instruments AT-GPIB/TNT™ interface board along with the NI-488.2™ and LabVIEW® software packages are installed in a Pentium computer for data acquisition.

The Model 2001 multimeter is connected to the movable thermistor inside the convection cell. To reach a sampling rate of 20Hz, the resistance data are first stored in the memory buffer of the multimeter and then transferred via GPIB to the computer. A LabVIEW program is composed to acquire a specified number of data files (typically between 10 and 15 files) continuously into the computer. Each data file contains 29899 data points (the maximum number allowed for the multimeter), which correspond to a 24.9-minute real time measurement. The transfer of the 29899 readings from the multimeter to the computer takes approximately two minutes. Therefore, there is a 2-minute gap between two adjacent data files. Since the temperature correlation time is much shorter than 25 minutes, the 2-min gap does not affect our statistical analysis of temperature fluctuations. The Model 199 multimeter is used to measure the temperature of the top and bottom plates of the cell. With a multi-channel mutiplexor on the back panel of the multimeter, we can simultaneously measure the resistance of the thermistors on the top and bottom plates.

3.5 Flow Visualization

To study the boundary layer dynamics in turbulent convection, we use a photographic technique to visualize the temperature and velocity fields near the boundary. With this technique, small thermochromic liquid crystal (TLC) particles are suspended in the fluid at a low concentration. These particles are composed of cholesteric liquid crystal, which are encapsulated in gelatin spheres. In the cholesteric mesophase, the liquid crystal molecules arrange themselves to form parallel planes. Within each plane the rod-like liquid crystal molecules are aligned in one direction, but the relative orientation of the molecules between two adjacent planes is rotated by a small angle [36]. As a result, the molecular structure undergoes a helical modulation in the direction normal to the parallel planes. Since the spatial period of the cholesteric helix or the pitch length L is comparable to optical wavelengths, strong Bragg scattering can be observed in the suspension sample when the orientation of the TLC spheres satisfies the Bragg condition. Because the pitch length L decreases with increasing temperature, the Bragg scattered light from the particles changes color from red to blue in a narrow temperature range.

The TLC spheres used in the experiment are purchased from Hallcrest (Hallcrest, R29C4W), and have been used previously in visualizing the temperature field in turbulent convection [32]. These particles have a mean diameter of $15\mu\text{m}$ and change color from red to blue in the back scattering direction over a temperature range of 4°C from 29°C to 33°C . The temperature of the bulk fluid is adjusted to be approximately 28.8°C , such that strongly scattered Bragg light can be seen from the side (at the scattering angle of 90°).

Figure 3.7 shows the optical set-up to produce a thin sheet of white light for illuminating a vertical section of the convecting fluid. An overhead projector lamp (General Electric ACG41-W3, 120V, 600W) is used as the light source (S). Two condensing lenses (L1) are used to collect the light from S and then project it onto a slit (P) with an adjustable width. The vertical sheet of light passing through the slit is focused on to the central section of the cell by a collimating cylindrical lens (L2). The thickness of the light sheet inside the cell is approximately 2 mm (full width at the half-maximum). The azimuthal orientation of the vertical light sheet is adjusted such that it coincides with the rotation plane of the large-scale circulation. It has been shown [37] that the azimuth of the large-scale circulation rotates slowly inside the cylindrical cell when it is leveled perfectly. To lock the azimuthal rotation of the large-scale circulation, we tilt the cell with a small angle less than 2° . Ciliberto et al. [25] have shown that such a small tilt does not affect turbulent convection very much. For flow visualization in the rough cell, we orientated the cell such that its central groove coincides with the rotation plane of the large-scale circulation. The light sheet in this case is directed along a groove passing through the center of the rough surface.

A Canon camera ($f=135\text{mm}$, $f/D=4.5$) is used to take streak pictures of the TLC spheres with a long exposure time of 0.5s. The streak picture can show the temperature and velocity fields simultaneously. We also use a color CCD camera (Panasonic DX251) situated normal to the illuminating light sheet to obtain continuous images of the flowing TLC spheres and record them on a video tape with a S-VHS video cassette recorder (Panasonic, AG-1970). In the picture of the TLC spheres, cooler regions of the fluid appear brown and warmer regions appear green and blue. With the videotape, one can

continuously watch the emission dynamics of the thermal plumes. A frame grabber is used to digitize a sequence of frames of interest and store them in the computer.

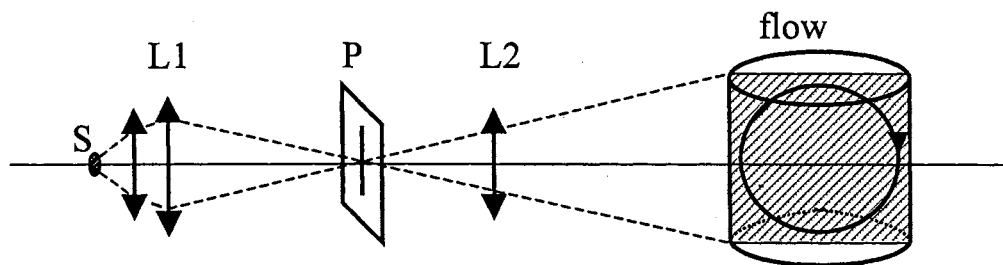


Figure 3.7 Schematic diagram of the optical set-up for flow visualization. S, GE quartzline lamp; L1, condensing lenses; P, adjustable slit; L2, cylindrical collimating lens.

CHAPTER IV

BOUNDARY LAYER MEASUREMENTS AND FLOW VISUALIZATION

4.1 Heat transport measurements and flow visualization

In the study of thermal convection, one is interested in the vertical heat transport through the cell. As discussed in Chapter 2, the Nusselt number Nu is defined as the actual heat flux through the cell normalized by the conductive heat flux. It describes the efficiency of turbulent heat transport. In our experiment, the actual heat flux is approximately equal to the heating power, because the heat loss is very small and can be ignored. Therefore, Nu for both the smooth and the rough cells is calculated as

$$Nu = \frac{PH}{\pi R^2 \chi \Delta T}, \quad (4.1)$$

where P is the total heating power, ΔT is the resulting temperature difference across the cell, χ is the thermal conductivity of water, H is the height of the cell, and πR^2 is the cross-sectional area of the cell. The control parameter in the convection experiment is the Rayleigh number Ra as defined in Equation (2.7). Because the heat transport measurements are conducted by varying heating power P , we plot the dimensionless heat flow $NuRa$ as a function of Ra . In this way, one can minimize the errors introduced by the measurement of ΔT .

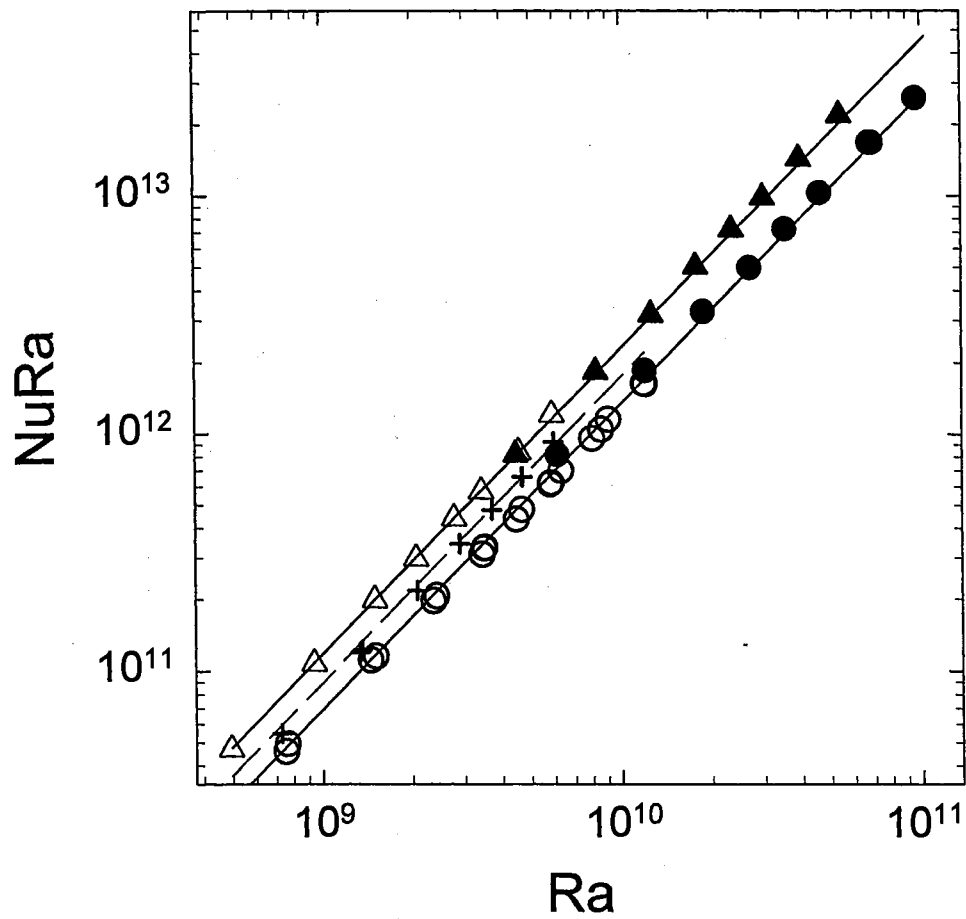


Figure 4.1 Measured $NuRa$ as a function of Ra in the smooth cells (circles) and in the rough cells with $h=9.0$ mm (triangles). The solid symbols represent the data obtained from the cells with $A=0.5$, and the open symbols are from the cells with $A=1.0$. The solid lines are the power law fits. The pluses are obtained in another rough cell with $h=3.2$ mm and $A=1.0$. The dashed line is a power law fit to the pluses.

Figure 4.1 shows the measured $NuRa$ as a function of Ra in the smooth cells (circles) and in the rough cells with roughness height $h = 9.0mm$ (triangles). The solid symbols represent the data obtained from the cells with the aspect ratio $A = 0.5$, and the open symbols are from the cells with $A=1.0$. The measured $NuRa$ in the smooth cells is well described by the power law $NuRa = 0.17Ra^{1+\beta}$ (the lower solid line), which indicates $Nu = 0.17Ra^\beta$. The exponent $\beta = 0.29$ agrees well with the previous measurements in water [7, 37, 38, 39] and in low temperature helium gas [5, 40]. As shown in Fig. 4.1, the heat transport in the rough cells with $h = 9.0mm$ is increased considerably in the whole range of Ra accessible to the present experiment. For a fixed heating power (i.e., at a fixed $NuRa$), the resulting temperature difference ΔT across the rough cell (and hence Ra) is found to be smaller than that across the smooth cell. This suggests that the rough cells have much less heat resistance and are more efficient for heat transfer. The measured heat flow $NuRa$ in the rough cells can also be well described by a power law with the same exponent β , but the amplitude is changed from 0.17 to 0.30 (the upper solid line). This amounts to a 76% increase in the heat transport. As described in Chapter 3, the rough elements form a square lattice of pyramids in the rough cell. Compare to the smooth cell, the total contact area between water and the top and bottom plates in the rough cell is increased by a factor of $\sqrt{2}$ (i.e., 41%). Therefore, the 76% increase of the heat flux can not be simply explained by the increase of the contact area.

In a recent experiment [34], Shen and Tong have shown that the effect of the surface roughness on the heat transport depends on the length ratio δ/h , where δ is the thickness of the thermal boundary layer. In the small Ra region, where $\delta > h$, the rough elements on the surface are buried beneath the thermal boundary layer, and hence the

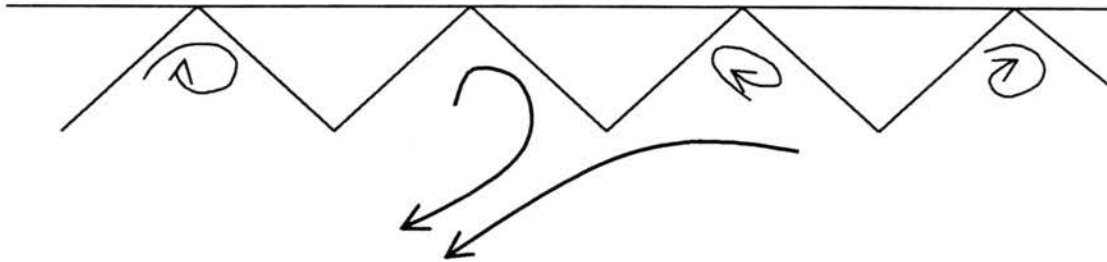
effect of the surface roughness is small. In the opposite limit of large Ra , where $\delta < h$, the surface roughness strongly affects temperature fluctuations near the surface and thereby alters the heat transport. Therefore, one can define a transitional Rayleigh number Ra_0 via the equation $\delta(Ra) \approx h$. The boundary layer thickness as a function of Ra can be calculated from the measured $Nu(Ra)$ by using the well-tested relation [27] $\delta(Ra) \approx H/[2Nu(Ra)]$. A transition near Ra_0 was indeed observed in the previous experiment [34]. For the rough cells with $h=9.0\text{ mm}$, we find $Ra_0 \approx 1.8 \times 10^6$, which is far below the working range of Ra shown in Fig. 4.1. The pluses in Fig. 4.1 show the measured $NuRa$ in the rough cell with $h=3.2\text{ mm}$ and $A=1.0$. For this rough cell we have $Ra_0 \approx 6.4 \times 10^7$, which is slightly below the Ra range accessible to the present experiment. It is seen from Fig. 4.1 that the pluses deviate gradually from the circles at low Ra and then become parallel to the circles and triangles at higher values of Ra . Over a limited range of Ra , the pluses can also be described by a power law with the same exponent $\beta = 0.29$, but the amplitude is increased from 0.17 to 0.22 (the dashed line). This further supports our conclusion that the enhanced heat transport in the rough cells cannot be explained simply by an increase in the contact area of the rough surface. As shown in Fig. 4.1, the measured $NuRa$ (or Nu) in the two rough cells with different h is changed considerably even though the contact area of their rough surfaces remains the same.

To find the real mechanism for the enhanced heat transport, we use the photographic technique described in Sec. 3.5 to visualize the temperature and velocity fields near the upper rough surface. Figure 4.2 (b) shows how a thermal plume (pointed by an arrow) is erupted from the (upper) cold rough surface. It is seen that the large-scale

motion in the near-wall region is well characterized by a simple shear flow (from right to left). However, the mean flow is modulated by the rough surface, a situation very much like a steady flow passing over bluff obstacles on a wall [41]. The mean flow is forced to become divergent from the surface when it meets with the upstream side of the pyramid. On the downstream side of the pyramid, an adverse pressure gradient region is formed inside the groove. This pressure gradient produces an eddy whose vorticity is opposite to that of the large-scale circulation. The interaction between the upstream divergent flow and the downstream back flow causes the thermal boundary layer to detach near the tip of the pyramid [see the sketch shown in Fig. 4.2 (a)]. The detached thermal boundary layer becomes a thermal plume, which is sheared to the downstream by the mean flow.

Figure 4.3 shows a streak picture of the TLC spheres taken near the upper surface of the smooth cell at $Ra = 2.6 \times 10^9$. We find that the emission dynamics of the thermal plumes in the smooth cell is totally different from that in the rough cell. In the smooth cell, the thermal plume is erupted by its own buoyancy force, which accelerates the fluid in the central stem of the plume. The sudden acceleration of the fluid produces a vortex ring around the stem (similar to the generation of a smoke ring), which gives the characteristic mushroom shape of the thermal plume. A 2-dimensional projection of the vortex ring gives rise to a pair of vortices with opposite signs. This is clearly shown in Fig. 4.3. In the rough cell, however, we find that the interaction between the eddy trapped inside the groove and the large-scale circulation causes the detachment of the thermal boundary layer near the tip of the rough elements. Because the detachment of the boundary layer is driven by the large-scale flow instead of the buoyancy force, the vortex

(a)



(b)

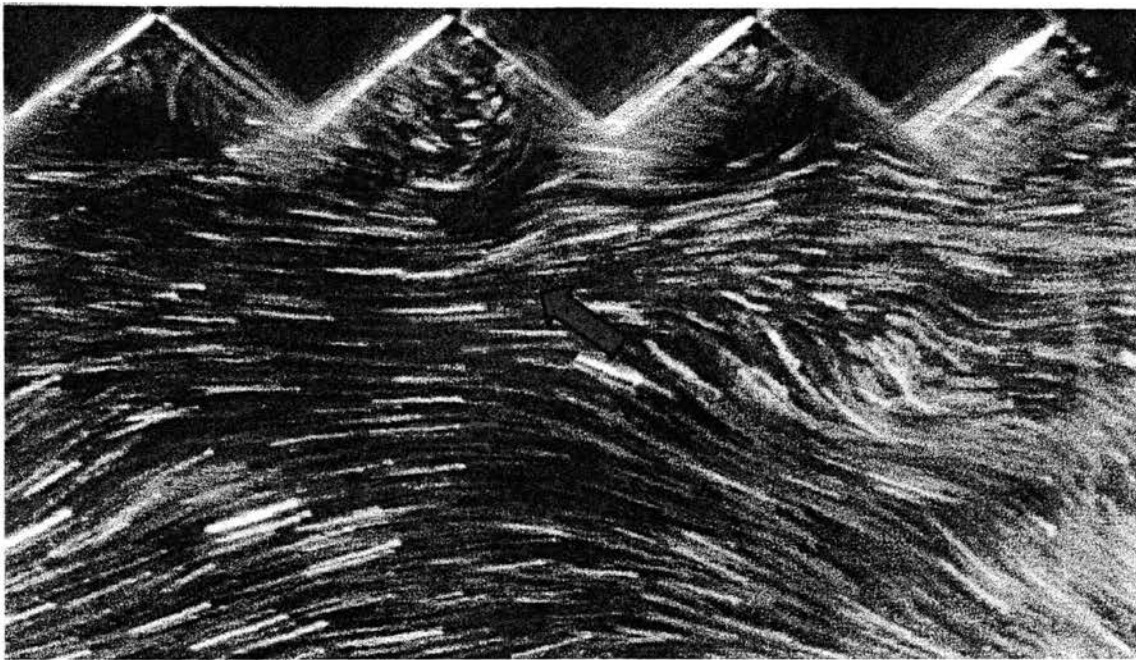


Figure 4.2 (a) Sketch of the flow field near the upper rough surface. (b) A typical streak image of the TLC spheres taken near the cold rough surface at $Ra = 2.6 \times 10^9$. The cold eruptions are brown; green and blue regions are warmer. The displayed region is approximately 7cm by 4cm. The arrow indicates a thermal plume, which just erupted from the tip of the pyramid.

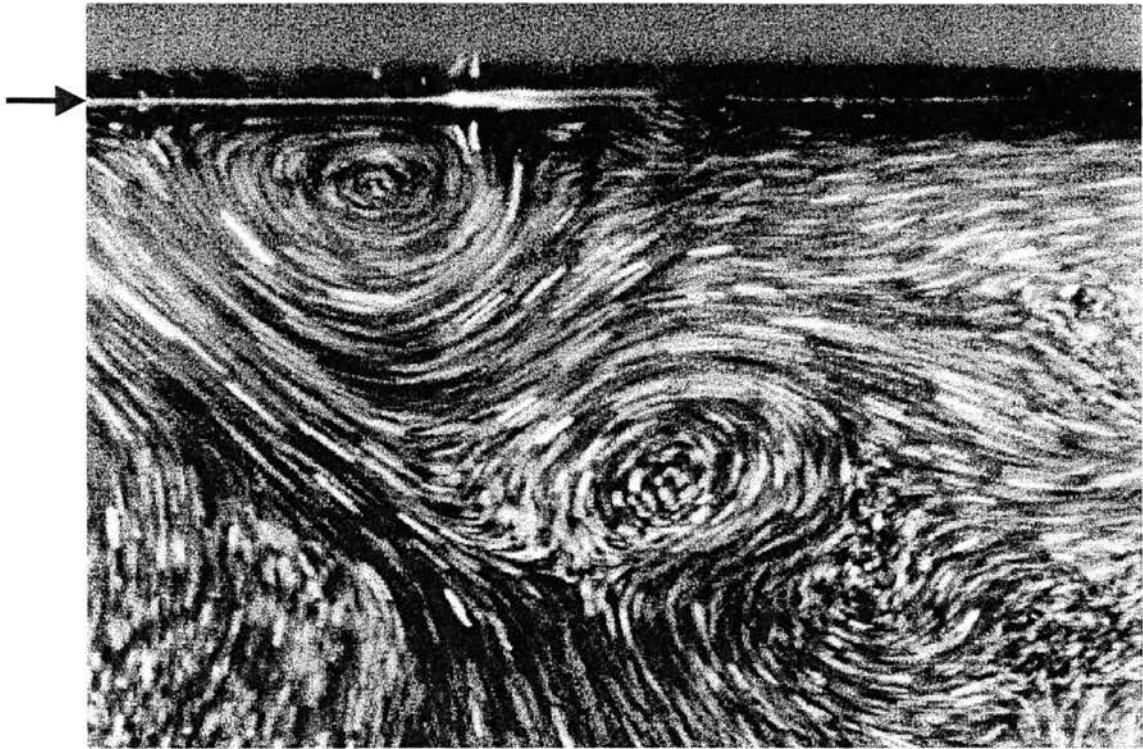


Figure 4.3. A streak image of the TLC spheres taken near the cold smooth surface at $Ra = 2.6 \times 10^9$. The cold eruptions are brown; green and blue regions are warmer. The displayed region is approximately 6.5cm by 4cm. The arrow on the left side of the graph indicates the position of the upper smooth surface.

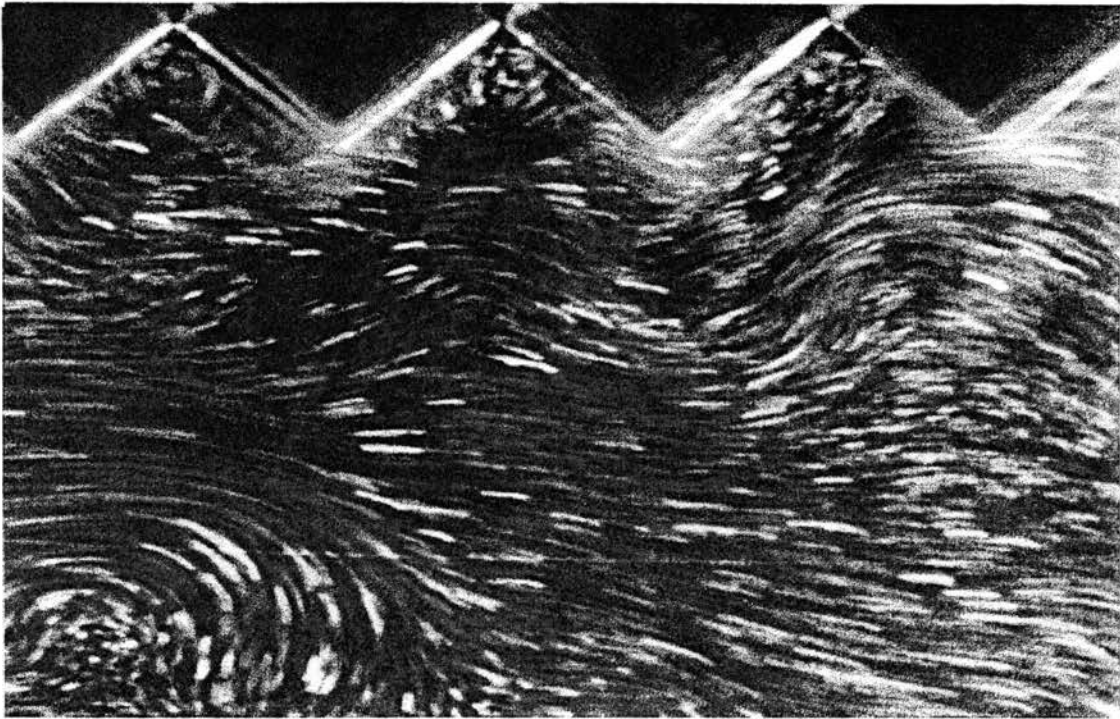


Figure 4.4 A streak image of the TLC spheres taken near the cold rough surface at $Ra = 2.6 \times 10^9$. The cold eruptions are brown; green and blue regions are warmer. The displayed region is approximately 6.3 cm by 3.8 cm.

ring associated with the buoyancy acceleration disappears and thus the thermal plumes in the rough cell lose their mushroom cap. Occasionally, we do see a few mushroom-shaped thermal plumes in the rough cell as shown in Fig. 4.4, but the majority of the thermal plumes looks like that shown in Fig. 4.2 (b) (pointed by an arrow).

Figures 4.5 and 4.6 show the eruption process of a thermal plume (pointed by a red arrow) in the smooth cell (Fig. 4.5) and in the rough cell (Fig. 4.6). The dynamic process is first recorded on a videotape and then the video images are digitized into a computer. The exposure time for each frame is 1/30 s and the time interval between two adjacent frames in Fig. 4.5 is 2 s and that in Fig. 4.6 is 1 s. The cold eruptions are brown; green and blue regions are warmer. Because the convecting fluid in the two cells has a slightly different mean temperature, the two time series of images show different background colors. The measurements are conducted at $Ra = 2.6 \times 10^9$ and the displayed region is approximately 6.5 cm by 4 cm. The arrows on the left side of the graphs in Fig. 4.5 indicate the position of the upper smooth surface (the bright line). The image above the bright line is caused by the reflection of the smooth surface. A thin fluid layer of brown color near the smooth surface (the bright line) is the thermal boundary layer, which fluctuates with time.

The top graph in Fig. 4.5 shows a thermal plume (pointed by an arrow), which is just erupted from the (upper) cold surface. The initial shape of the "plume cap" varies from time to time, and here it looks like a spherical blob. Because of the large-scale circulation, the thermal plume is sheared to the downstream direction (to the right). It is seen from the middle graph that after 2 s the thermal plume is shifted to the middle of the picture (travelling distance is ~ 2.3 cm) and obtains the characteristic mushroom shape.

As the thermal plume is further sheared to the downstream direction, the left part of the plume, whose vorticity has the same sign as that of the large-scale circulation, gains more energy whereas the right part of the plume, whose vorticity is opposite to that of the large-scale circulation, gradually loses its kinetic energy. Eventually, the right part of the plume disappears and the left part of the plume becomes part of the large-scale circulation. The bottom graph in Fig. 4.5 shows the thermal plume at the later stage.

Figure 4.6 shows the eruption process of a thermal plume in the rough cell. The top graph shows a brown thermal plume (pointed by a red arrow), which is just erupted from the tip of the left most pyramid. The shape of the thermal plume is different from that in the smooth cell and it does not have a mushroom cap. Similar to the situation in the smooth cell, the thermal plume is sheared to the downstream direction (to the right) by the large-scale circulation. It is seen from the middle graph (1 s later) that while the top part of the plume is sheared to the right, the “root” of the plume is pinned down to the tip of the pyramid. This situation is different from that in the smooth cell, in which the “root” of the thermal plume slides on the smooth surface, when the whole plume is sheared to the right (see Fig. 4.5). The bottom graph in Fig. 4.6 shows the later stage of the thermal plume, which is further sheared to the right. The color of the plume is changed during this period of time (2s) from brown to light green, indicating that heat has diffused into the cold plume and its temperature is increased.

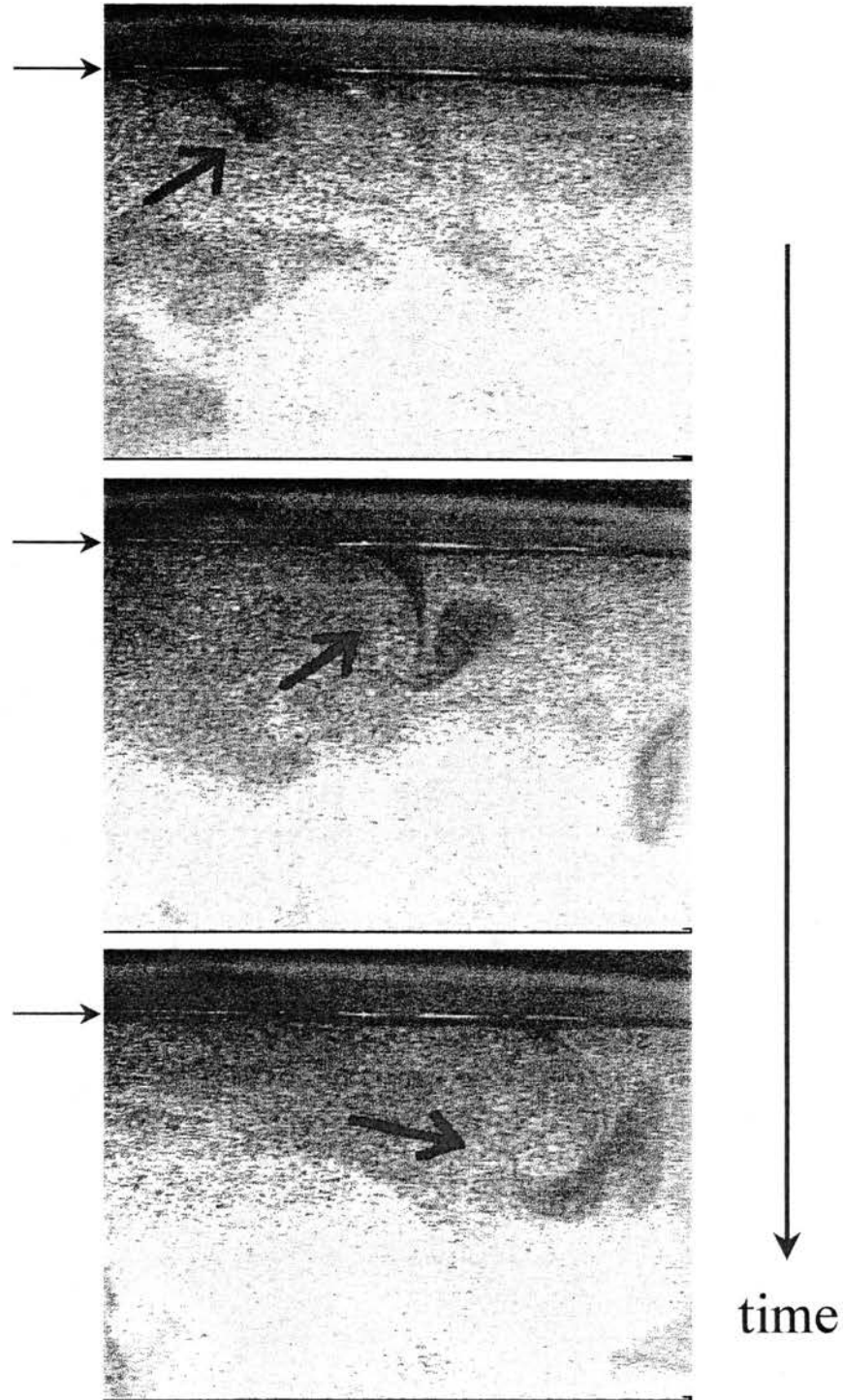


Figure 4.5 A time sequence of the TLC particle images illustrating the eruption process of a thermal plume (pointed by a red arrow) in the smooth cell at $Ra = 2.6 \times 10^9$. The time interval between two adjacent frames is 2 s. The displayed region is approximately 6.5cm by 4cm. The arrows on the left side of the graphs indicate the position of the upper smooth surface.

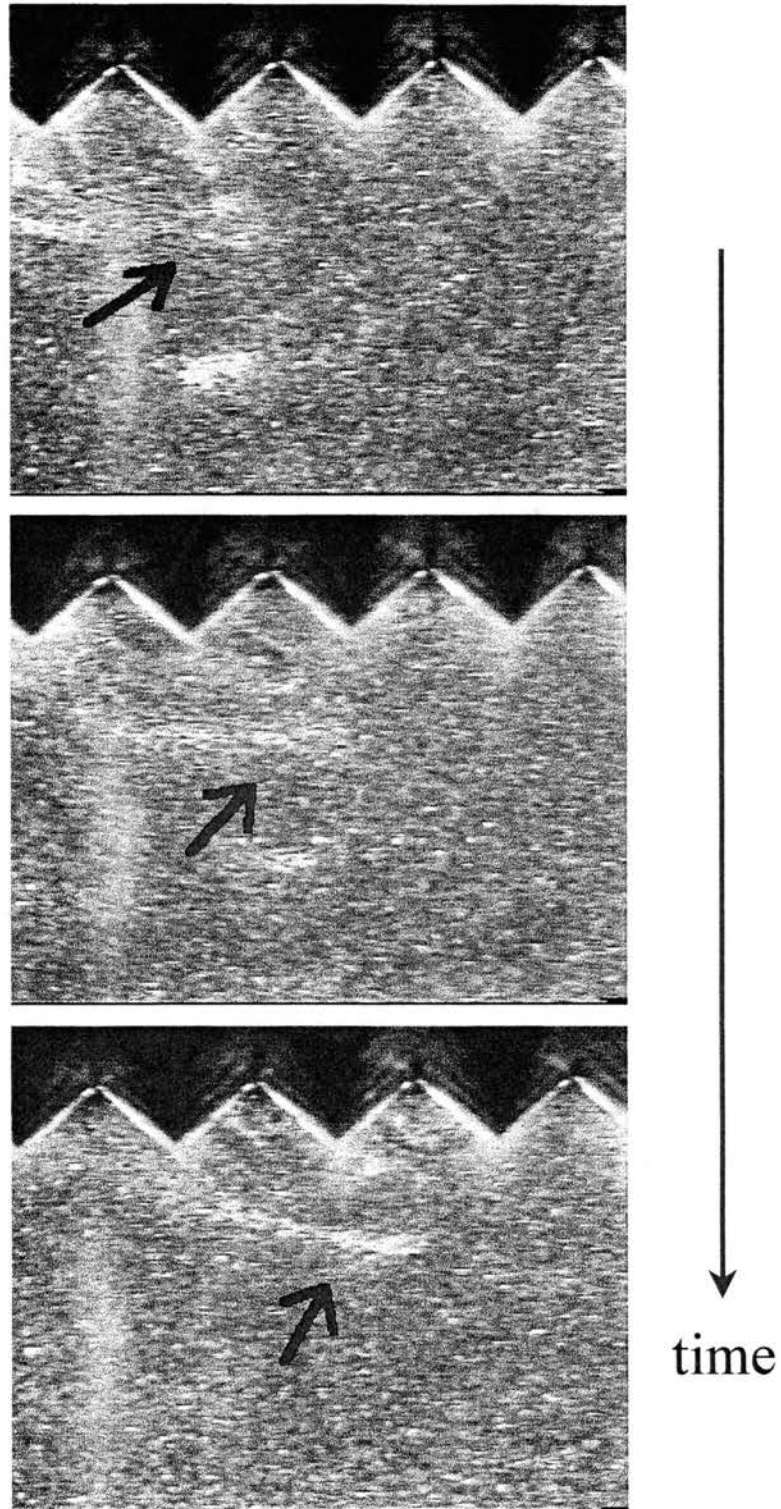


Figure 4.6 A time sequence of the TLC particle images illustrating the eruption process of a thermal plume (pointed by a red arrow) in the rough cell at $Ra = 2.6 \times 10^9$. The time interval between two adjacent frames is 1 s. The displayed region is approximately 6.5cm by 4cm.

4.2 Local temperature fluctuations and their histograms

The visualization measurements discussed above reveal the global structure of the temperature and velocity fields near the upper rough surface. We now discuss the local temperature measurements in this region, which provide statistical information about the temperature fluctuations. All the local temperature measurements, to be discussed in this and the next section, are performed in the cells with $A=1$. Figure 4.7 shows typical time series measurements of the local temperature T in the smooth (red curve) and rough (blue curve) cells. The measurements are made at $Ra = 2.6 \times 10^9$ and the corresponding thermal boundary layer thickness is $\delta \approx 1.5 \text{ mm}$. The movable temperature probe in the rough cell is placed at the position V and the distance z is measured from the bottom of the groove. The values of z are (a) $z=24 \text{ mm}$ (outside the rough surface), (b) $z=7 \text{ mm}$ (inside the groove but outside the thermal boundary layer), and (c) $z=0.6 \text{ mm}$ (inside the thermal boundary layer). It is seen from Fig. 4.7 that the cold fluctuations are superposed on an average base line. The downward going spikes are associated with cold plumes detached from the upper boundary layer and they are carried through the temperature probe by the large-scale circulation. Figure 4.7 (b) clearly shows that the emission of the (cold) thermal plumes is greatly enhanced in the rough cell. From the flow visualization we have learned that near the upper rough surface many thermal plumes are carried away horizontally by the large-scale circulation. Therefore, moving the temperature probe further away from the boundary will reduce the probability of detecting the thermal plumes. Nevertheless, Fig. 4.7 (a) shows that there are still some energetic thermal plumes, which can penetrate vertically into the bulk region of the convective flow.

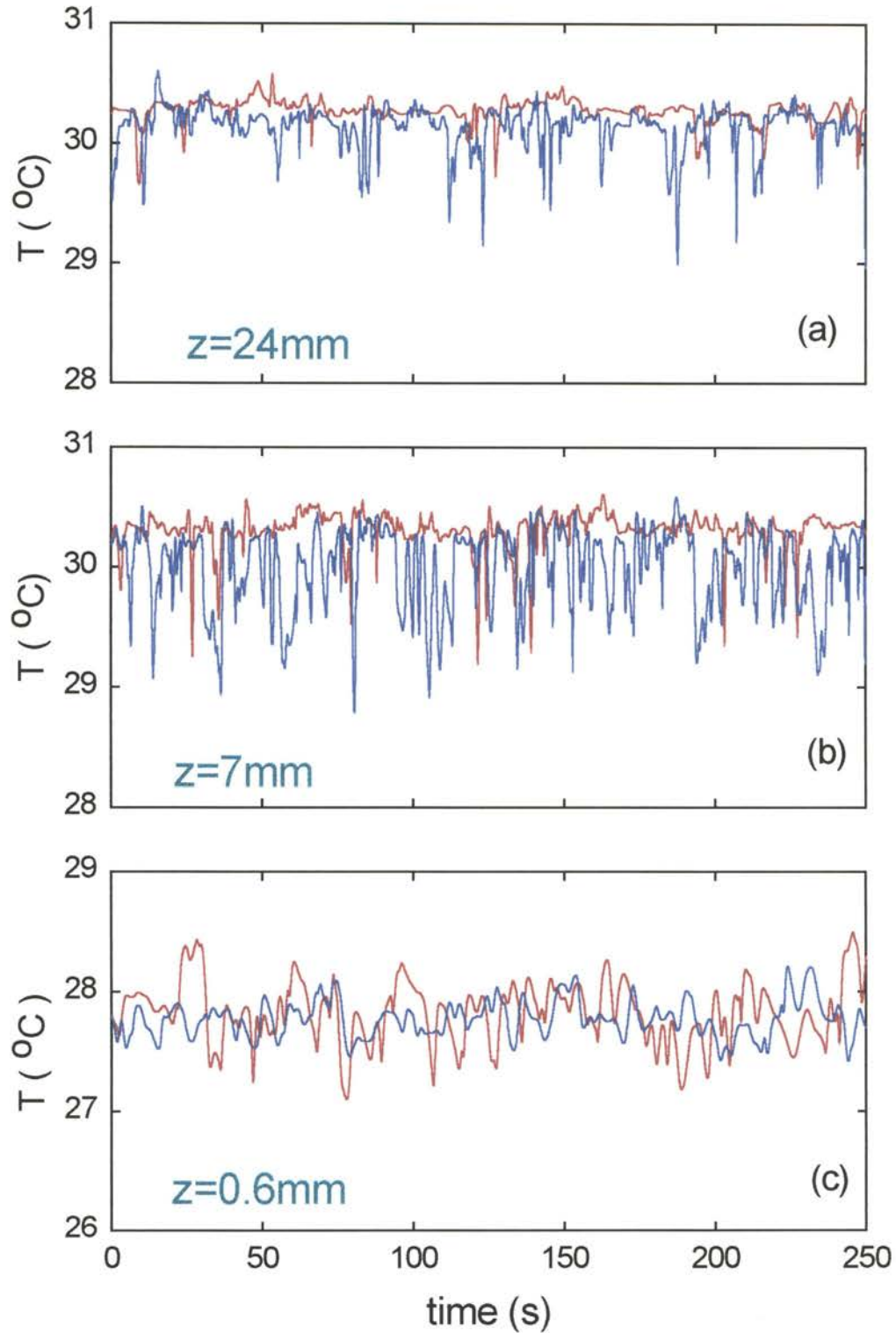


Figure 4.7 Typical time series measurements of temperature fluctuations near the upper (cold) plate in the smooth (red curve) and rough (blue curve) cells. The measurements are made at $Ra = 1.5 \times 10^9$. The movable temperature probe in the rough cell is placed at the position V and the distance z is measured from the bottom of the groove.

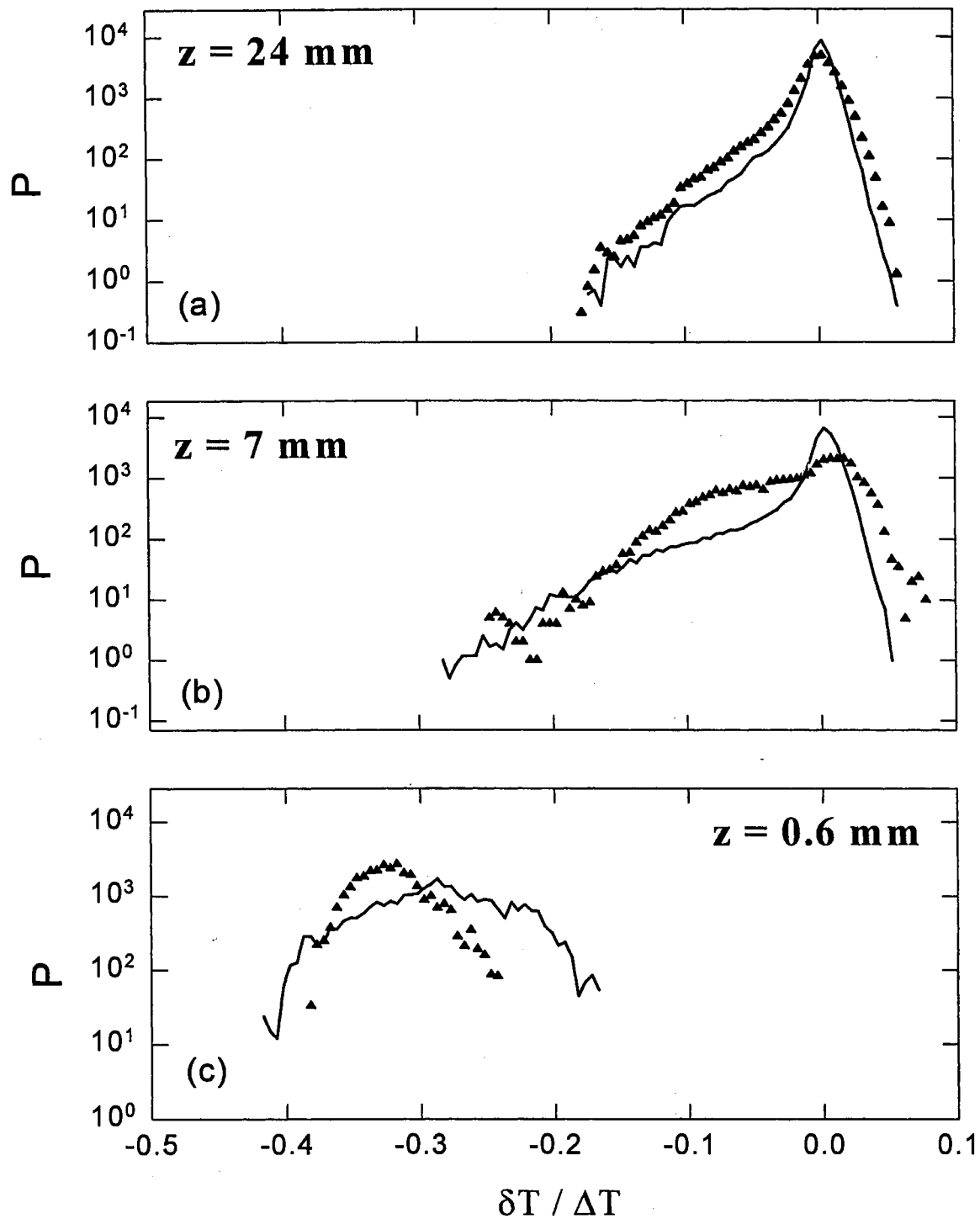


Figure 4.8 Comparison of the temperature histograms between the smooth cell (solid curves) and the rough cell (triangles). The histograms are computed using the time series data shown in Fig. 4.7.

To learn the distribution of temperature fluctuations, we compute their histogram using the time series data. Figure 4.8 shows the temperature histograms corresponding to the time series measurements shown in Fig. 4.7. The solid curves are obtained from the smooth cell and the triangles are obtained from the rough cell. The duration of the time series measurement for each value of z was set to be 8.3 minutes (10,000 data points) and the sampling rate was 20 Hz. It is seen from Fig. 4.8 (a) that when z is far away from the boundary ($z=24$ mm), the temperature histograms for the smooth and rough cells have a similar shape. Both of them are skewed towards the cold side, because more cold plumes are captured in the time series measurements. As shown in Fig. 4.7 (a), the emission of the cold plumes is greatly enhanced in the rough cell and, therefore, the corresponding histogram has a wider distribution when compared with that in the smooth cell. In the groove region ($z=7$ mm), the measured histogram shows a bigger shoulder on the cold side, which suggests that the extra thermal plumes produced by the rough surface are mostly of medium size. From the flow visualization we have learned that the interaction between the horizontal shear flow and the rough surface creates small eddies in the groove region. These eddies produce a strong mixing effect, which increases temperature fluctuations on both the warm and cold sides. This is clearly shown in Fig. 4.8(b). In contrast to the situation at $z=7$ mm, temperature fluctuations inside the boundary layer ($z=0.6$ mm) are found to be reduced in the rough cell. Figure 4.7 (c) shows that temperature fluctuations inside the thermal boundary layer are more symmetric and do not have sharp spikes as those shown in Figs. 4.7 (a) and 4.7 (b). It is seen from Fig. 4.8(c) that temperature fluctuations deep inside the groove region are reduced considerably when compared with those in the smooth cell. As will be shown in the next

section, the thermal boundary layer thickness δ is increased in the groove region. These measurements suggest that the thermal boundary layer in the groove region is further stabilized by the enhanced detachment of the thermal plumes near the tip of the pyramids.

Because the local heat transport is inversely proportional to δ (see Eq. 2.13), one might ask why the overall heat transport is increased whereas the local temperature gradient in the groove region is reduced? To answer this question, we measure the temperature fluctuations near the tip of a central pyramid. Figure 4.9 compares the temperature fluctuations at the position V (blue curve) and position T (red curve). The measurements are made at $Ra = 1.5 \times 10^9$. The corresponding histograms are shown in Fig. 4.10. The top graph of Fig. 4.9 shows the time series measurements when z is at 24 mm away from the bottom of the groove (blue curve) and at 14 mm away from the tip of the pyramid (red curve). Because the height of the pyramid is 9 mm, the two measurements are made at approximately the same horizontal level far away from the rough surface. The measured histograms clearly show that temperature fluctuations at this distance are independent of the horizontal positions. The situation is changed completely, when the distance z becomes closer to the rough surface. In the middle graph of Fig. 4.9, the blue curve is measured at 7mm away from the bottom of the groove (inside the groove) and the red curve is measured at 7mm away from the tip of the pyramid (outside of the groove region). It is seen from the middle graphs of Figs. 4.9 and 4.10 that there are more downward going spikes at the position V. From the flow visualization discussed in Sec. 4.1, we have learned that many thermal plumes emitted from the tip of the rough elements are sheared to the downstream by the horizontal mean flow and some of them are mixed into the groove region by the eddies trapped inside the

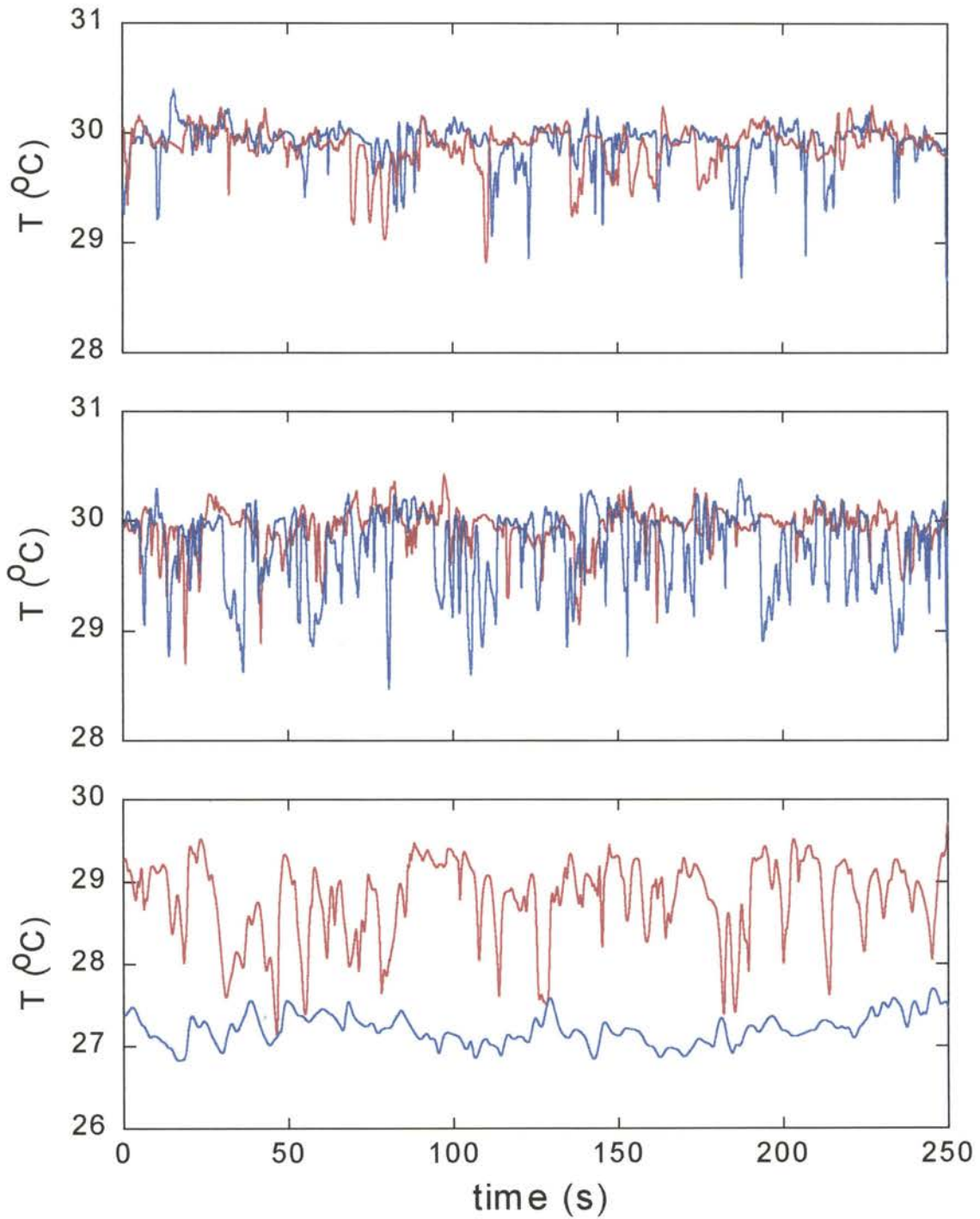


Figure 4.9 Time series measurements of temperature fluctuations at the position V (blue curve) and position T (red curve). The measurements are made at $Ra = 1.5 \times 10^9$. The values of z for the red curves are: $z=14$ mm (top), 7 mm (middle), and 0.6 mm (bottom). The values of z for the blue curves are: $z=24$ mm (top), 7 mm (middle), and 0.6 mm (bottom). The distance z at the two lateral positions T and V are measured, respectively, from the tip of the pyramid and from the bottom of the groove.

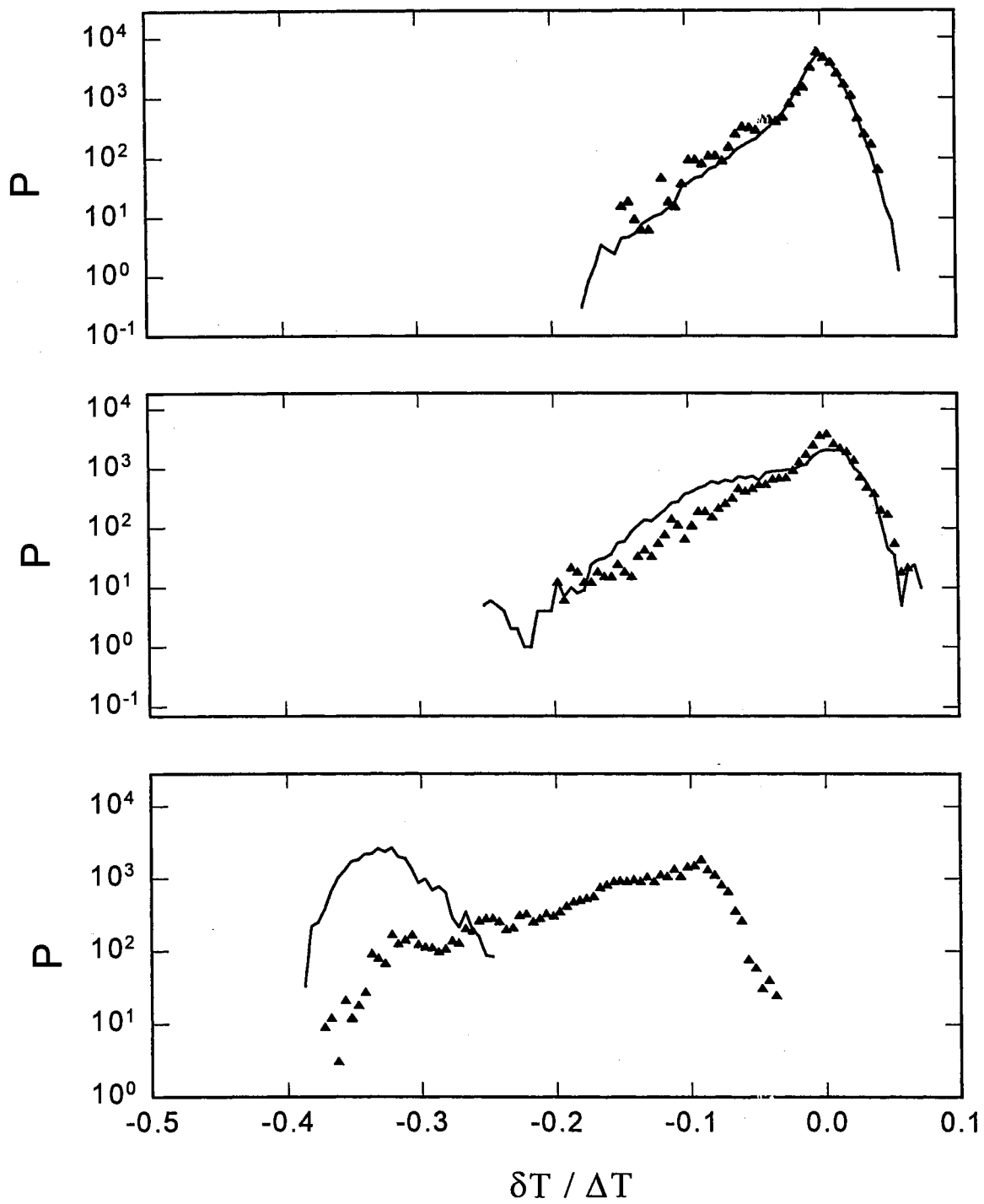


Figure 4.10 Comparison of the temperature histograms at the position V (solid curve) and position T (triangles). The histograms are computed using the time series data shown in Fig. 4.9.

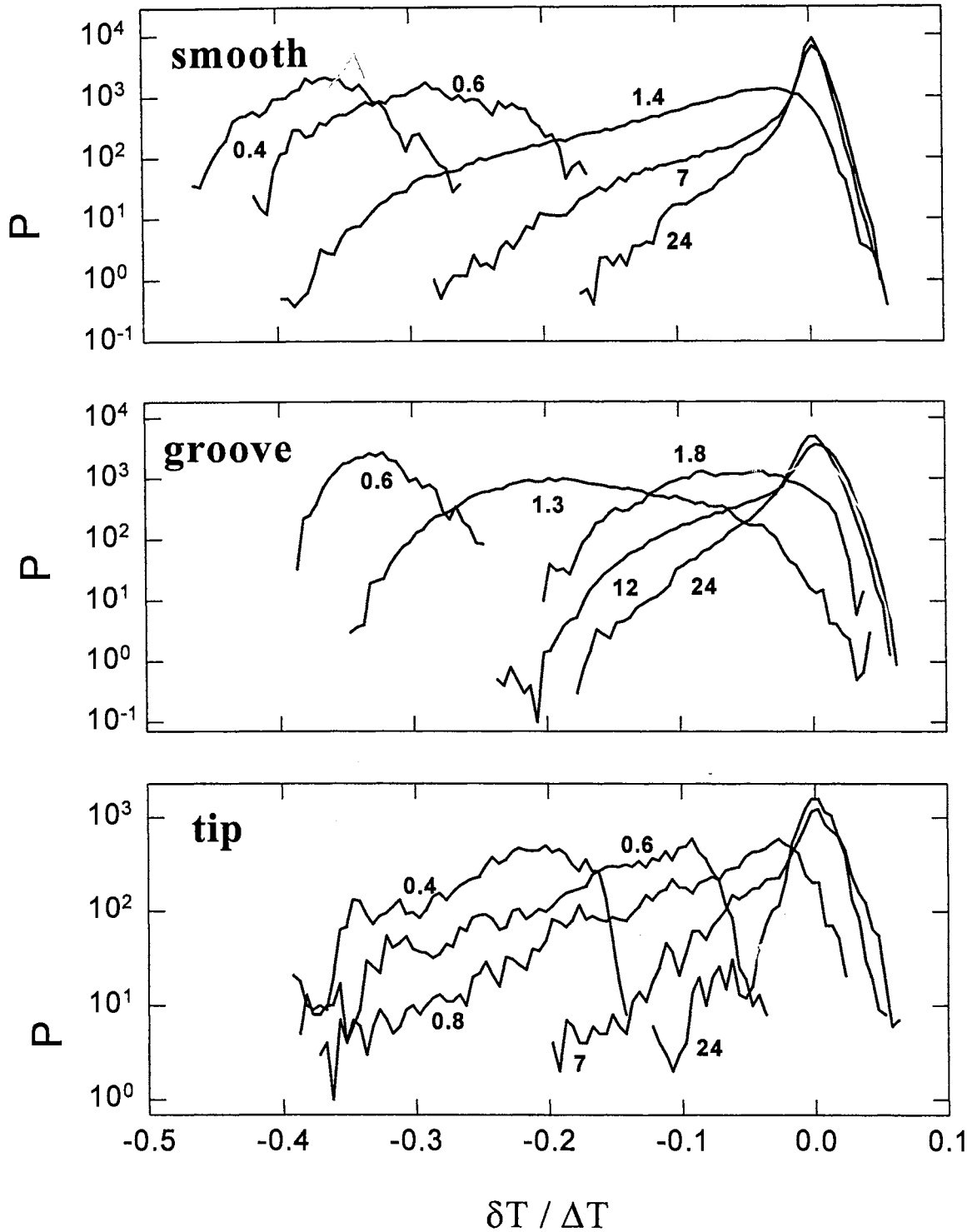


Figure 4.11 Measured temperature histograms at different values of z away from the top plate. The number near each curve indicates the value of z in mm. In the rough cell, the value of z at the position V (middle graph) is measured from the bottom of the groove and at the position T (bottom graph) it is measured from the tip of the pyramid.

grooves. The local temperature measurements shown in Figs 4.9 and 4.10 are therefore in good agreement with the flow visualization.

The bottom graphs of Figs. 4.9 and 4.10 show the temperature fluctuations and their histograms when z is inside the thermal boundary layer. An important feature shown in Fig. 4.9 is that the average surface temperature at the tip is higher than that at the bottom of the groove. Unlike the smooth surface, the rough surface is no longer an isothermal surface. The pyramids are surrounded by warm water and emit more cold plumes near their tips. This local dynamic process destroys the temperature homogeneity and produces a higher surface temperature at the tip. It is also seen from Fig. 4.9 that temperature fluctuations near the tip are much stronger than those in the groove region. The temperature histogram near the tip is found to be skewed towards the cold side (i.e., the skewness $S \equiv \langle (T - \bar{T})^3 \rangle / \langle (T - \bar{T})^2 \rangle^{3/2} < 0$). This is because the large-scale circulation carries many cold plumes horizontally near the tip. At the bottom of the groove, however, the thermal boundary layer is influenced strongly by the eddy mixing effect, which produces more warm fluctuations inside the boundary layer. As a result, the temperature histogram shows a small positive skewness. These changes in the histogram are shown in the bottom graph of Fig. 4.10. Note that the temperature histogram in the smooth cell is symmetric and its skewness S is approximately equal to zero.

To further illustrate the changes of the temperature statistics at different z , we plot, in Fig. 4.11, the temperature histograms measured at different values of z in the smooth cell (top graph) and in the rough cell at the position V (middle graph) and position T (bottom graph). The number near each curve indicates the value of z in mm. The temperature histogram undergoes many changes in shape when z is varied from zero

to the center of the cell. In the smooth cell, the shape of the histograms changes from a nearly Gaussian form within the boundary layer ($z=0.4$ mm) to an exponential form (to be shown in sec. 5.1) at the cell center ($z=100$ mm), with the broadest distribution at the edge of the thermal boundary layer ($z=1.4$ mm). In the rough cell, the temperature histograms at the positions V and T undergo similar changes as those in the smooth cell, but they also show some interesting new features. As discussed in the above, the temperature histograms inside the thermal boundary layer have different values of the skewness S . In the smooth cell, the distribution is symmetric and $S \approx 0$. In the rough cell, however, the distribution becomes asymmetric and S changes its sign from a positive value at the position V to a negative one at the position T. Because the mean temperature inside the (cold) thermal boundary layer increases linearly with z , the peak position of the measured histograms changes with z until z becomes larger than the boundary layer thickness δ . From Fig. 4.11 we find that the edge of the boundary layer is located at $z \approx 1.4$ mm (top graph), 1.8 mm (middle graph), and 0.8 mm (bottom graph), respectively. Fig. 4.11 thus suggests that the thermal boundary layer thickness δ in the groove region is increased, whereas near the tip of the pyramid δ is decreased when compared with that in the smooth cell.

4.3 Temperature profiles near the upper surface

To quantitatively characterize the temperature statistics at different values of z , we discuss, in this section, two important parameters of the temperature histogram. One is the mean temperature profile $T(z)$ and the other is the root mean square (RMS) temperature profile $T_{RMS}(z)$. Figure 4.12 shows the measured $T(z)$ near the top plate in

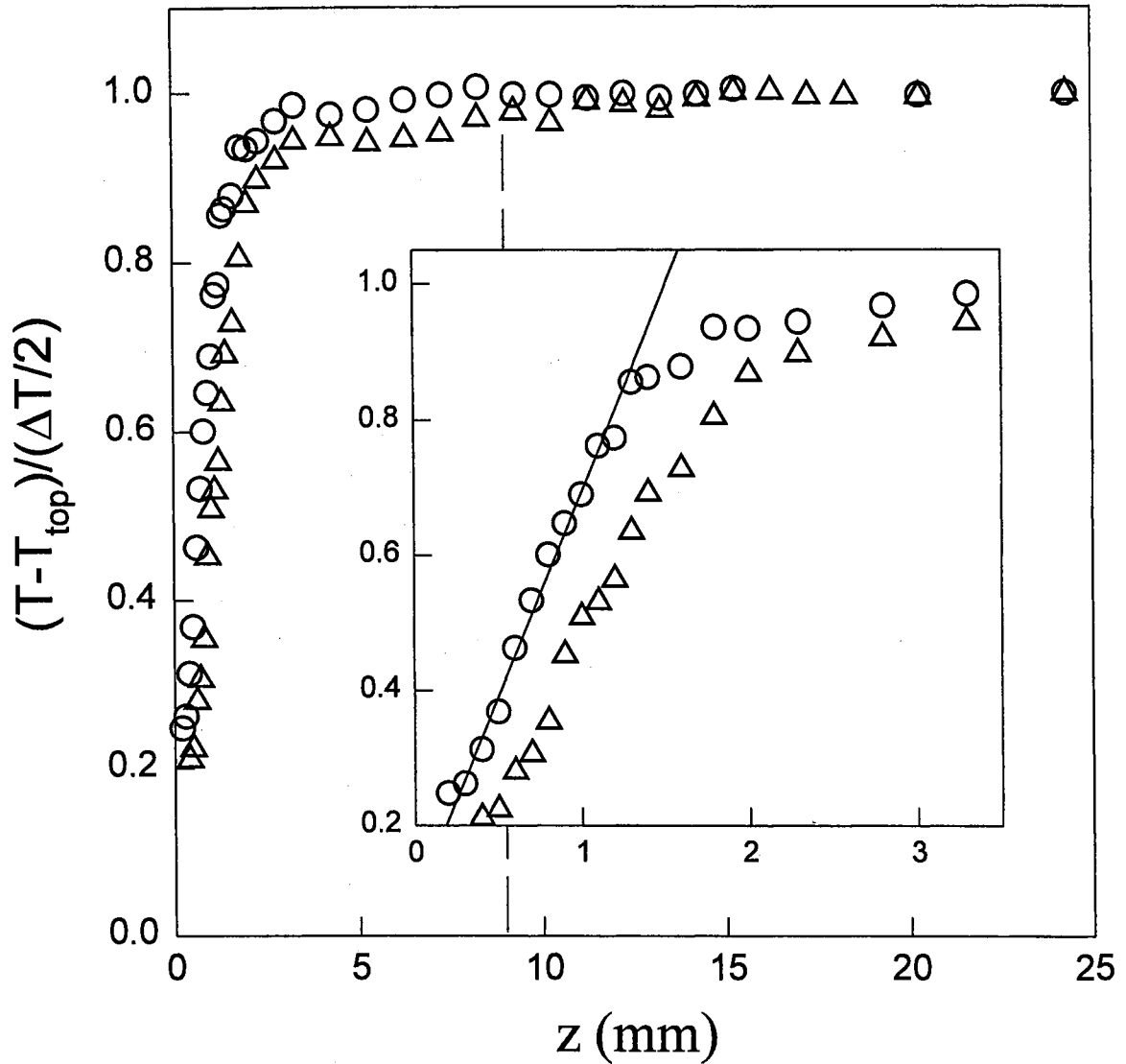


Figure 4.12 Measured mean temperature profile $T(z)$ in the smooth cell (circles) and in the rough cell at the position V (triangles). The measurements are made at $Ra = 1.5 \times 10^9$. The mean temperature, $T - T_{top}$, relative to the top plate temperature T_{top} is normalized by one half of the temperature difference ΔT across the cell. The vertical dashed line indicates the roughness height h . The insert shows an enlarged portion of the plot near the boundary and the solid line is a linear fit.

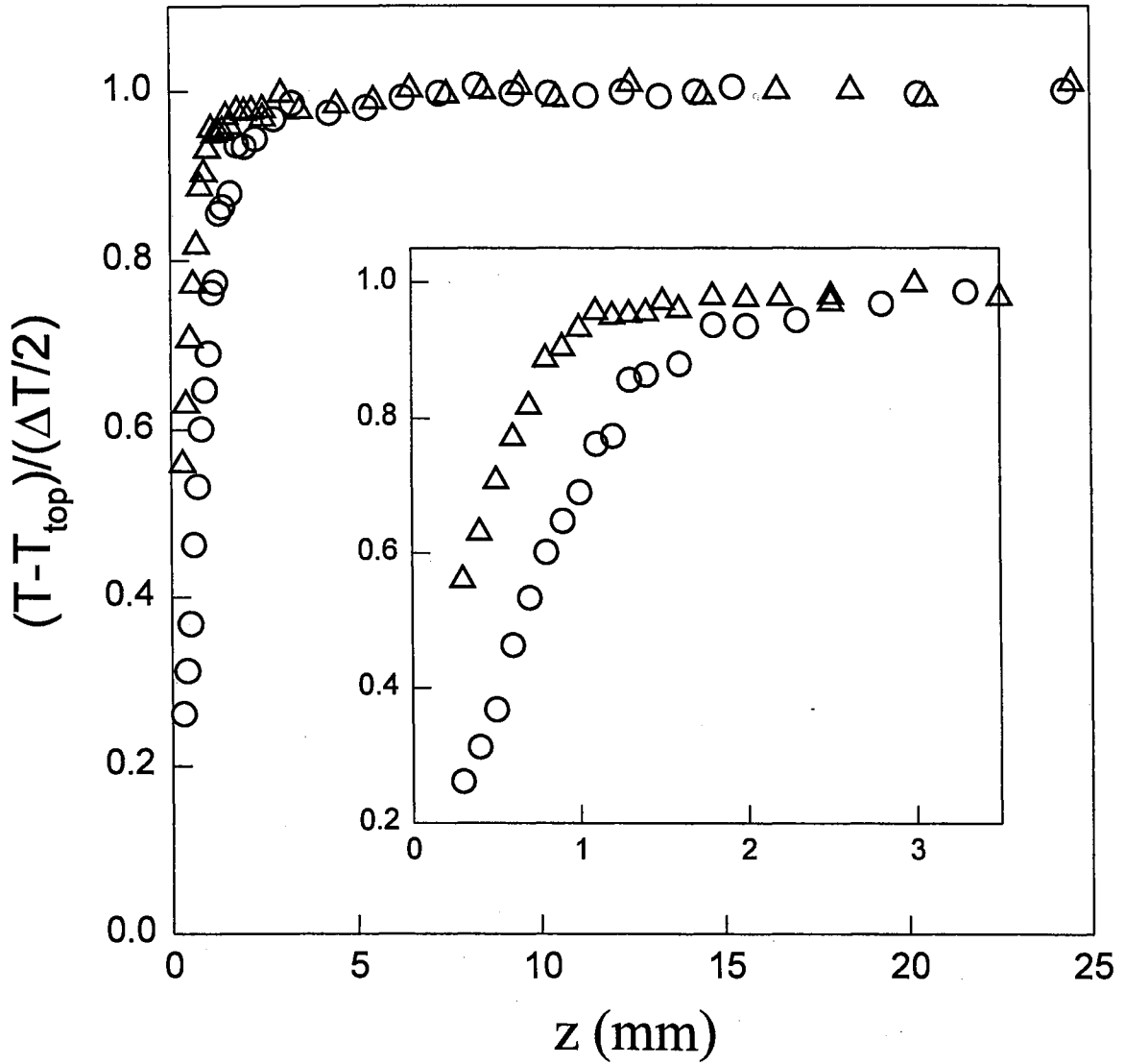


Figure 4.13 Measured mean temperature profile $T(z)$ in the smooth cell (circles) and in the rough cell at the position T (triangles). The measurements are made at $Ra = 1.5 \times 10^9$. The mean temperature, $T - T_{top}$, relative to the top plate temperature T_{top} is normalized by one half of the temperature difference ΔT across the cell. The insert shows an enlarged portion of the plot near the boundary.

the smooth cell (circles) and in the rough cell at the position V (triangles). The mean temperature at each value of z is obtained from the time series data and is normalized such that the top plate temperature is 0 and the bulk fluid temperature is 1. The measurements are made at $Ra = 1.5 \times 10^9$. In the smooth cell, the measured $T(z)$ increases linearly with z for small values of z (the solid line). After it reaches a maximum value T_m , the measured $T(z)$ remains constant throughout the bulk region. The measurement indicates that turbulent mixing creates, on average, an isothermal fluid in the bulk region and the temperature gradient across the cell is concentrated in thin thermal boundary layers. The boundary layer thickness δ can be defined as a distance, at which the extrapolation of the linear part of $T(z)$ equals to T_m . From Fig. 4.12 we find $\delta = 1.5$ mm in the smooth cell.

The temperature profiles measured in the rough cell at the positions V and T have a similar shape as that in the smooth cell, but they also show some interesting new features. It is seen from Fig. 4.12 that the mean temperature in the groove region ($z < h$) is reduced approximately by 0.5°C when compared with the smooth cell. This is caused by the mixing effect of the eddies trapped inside the cold groove. Another interesting feature shown in Fig. 4.12 is that the thermal boundary layer at the bottom of the groove becomes thicker than that in the smooth cell. The measured value of δ ($= 2.0$ mm) at the position V is found to be increased by 33% at $Ra = 1.5 \times 10^9$. Because the local heat transport is proportional to δ^{-1} (see Eq. 2.13) [11], Fig. 4.12 thus suggests that the local heat transport in the groove region is reduced. However, the local heat transport near the tip of the pyramids is found to be increased greatly. As shown in Fig. 4.13, the measured $T(z)$ near the tip has a shape similar to that in the smooth cell, but the value of δ is

reduced from 1.5 mm to 0.85 mm. Figures 4.12 and 4.13 also show that the surface temperature at the tip (extrapolated to $z=0$) is higher than that at the bottom of the groove. As discussed in the last section, the local emission dynamics of the thermal plumes destroys the temperature homogeneity on the rough surface. The local temperature measurements shown in Figs. 4.12 and 4.13 thus further support our conclusion that the interaction between the eddies trapped inside the groove and the large-scale circulation enhances the detachment of the thermal boundary layer near the tip of the pyramids. These extra thermal plumes increase the heat transport in the rough cell. The measurements of $T(z)$ in the rough cell also indicate that the thermal boundary layer follows the contour of the rough surface. Figure 4.14 depicts a sketch of the thermal boundary layer near the rough surface.

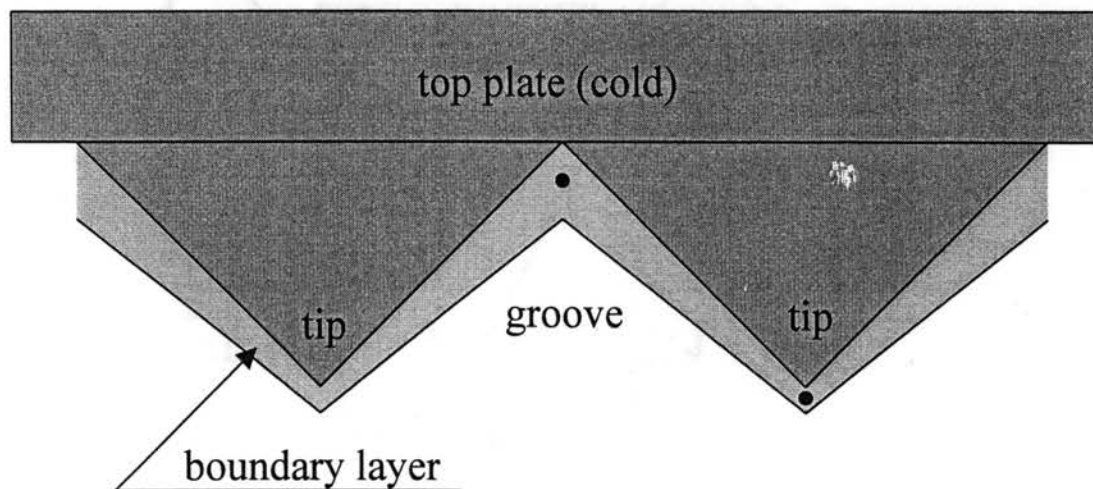


Figure 4.14 Sketch of the thermal boundary layer (light shadowed area) near the rough surface. The small dots indicate the two positions of the temperature measurement.

We now examine how the temperature profile $T(z)$ changes with the Rayleigh number. It is found that the measured $T(z)$ in the smooth cell for different values of Ra can all be brought into coincidence, once the distance z is scaled by the thermal boundary layer thickness δ . The plot of $T(z)$ vs. z/δ remains invariant and only δ changes with Ra . Figure 4.15 (a) shows the measured $T(z)$ as a function of z/δ for three different values of Ra in the smooth cell. The scaling behavior of $T(z)$ suggests that the structure of the turbulent temperature field near the boundary is invariant with Ra . Similar scaling behavior has been observed previously in a smooth cell filled with high pressure gases [10]. Figure 4.15(b) shows the measured $T(z)$ as a function of z for three different values of Ra in the rough cell at the position T. The shape of the measured $T(z)$ is similar to that in the smooth cell, but the value of δ now becomes insensitive to Ra . A possible reason for the Ra -independent behavior of δ is that the thermal boundary layer may not be well developed at the tip, because it is a singular point on the rough surface. Figure 4.16 shows the measured $T(z)$ as a function of z/δ for three different values of Ra in the rough cell at the position V. The measured $T(z)$ near the boundary is found to scale with z/δ , but the shoulder part of $T(z)$ does not scale with z/δ . It has been shown in Fig. 4.12 that the small eddies trapped inside the groove reduce the mean temperature in the groove region ($z < h$) by 0.5°C . Therefore, the shoulder part of $T(z)$ should scale with the roughness height h , which is independent of Ra . The h -scaling is indeed observed in the groove region and is shown in the insert of Fig. 4.16.

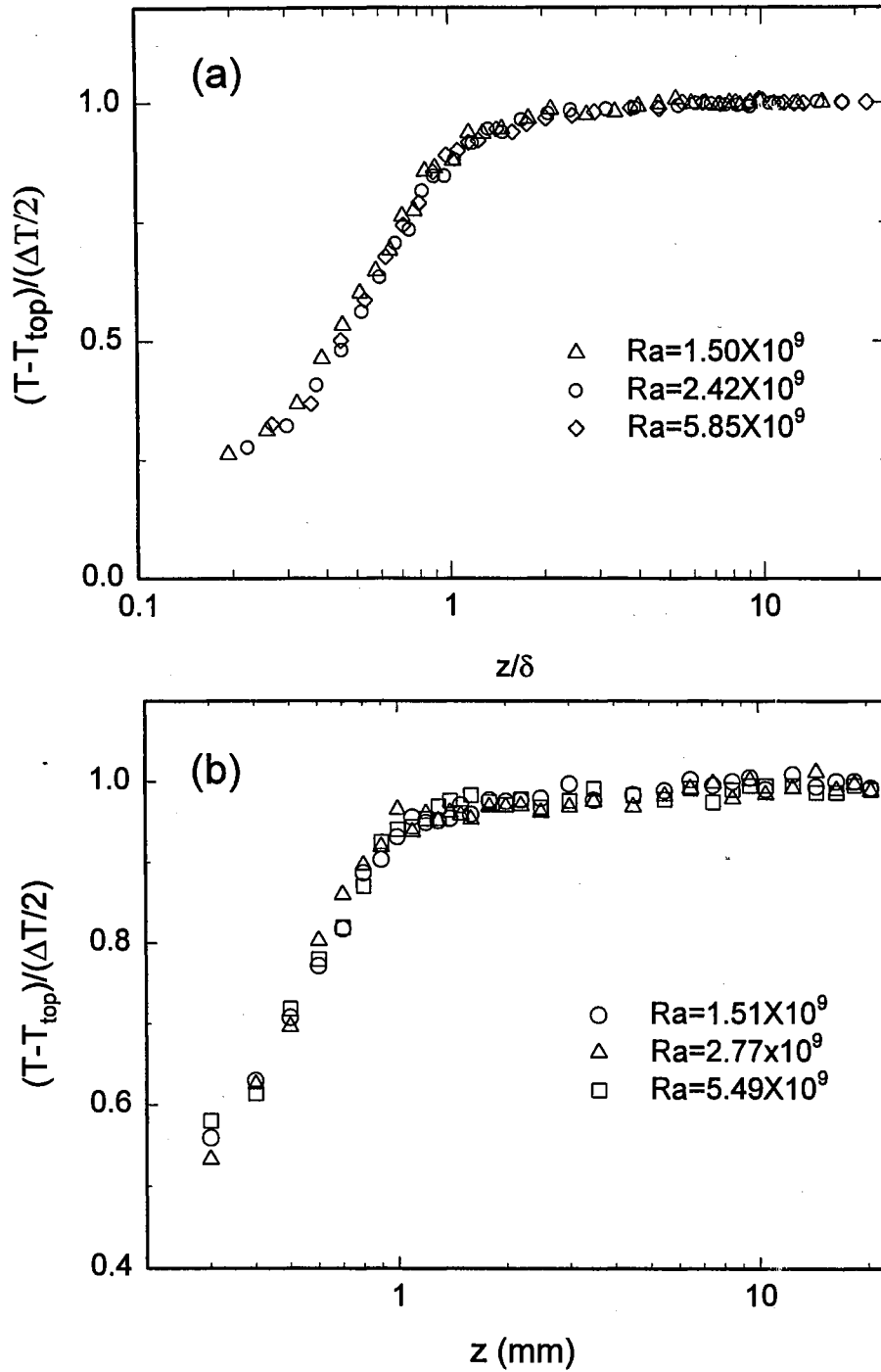


Figure 4.15 (a) Measured temperature profile $T(z)$ as a function of z/δ for three different values of Ra in the smooth cell. (b) Measured temperature profile $T(z)$ as a function of z for three different values of Ra in the rough cell at the position T.

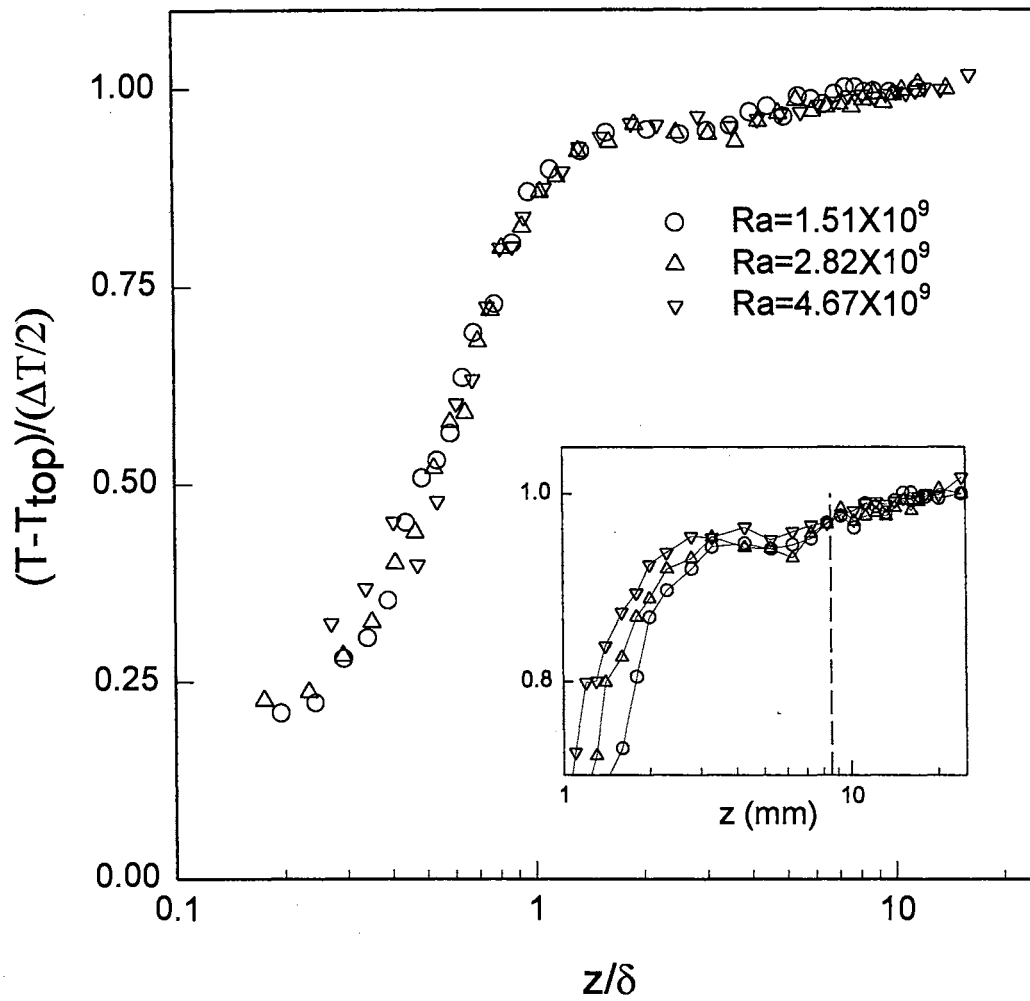


Figure 4.16 Measured temperature profile $T(z)$ as a function of z/δ for three different values of Ra in the rough cell at the position V. The insert shows the same plot as a function of z .

As discussed above, the boundary layer thickness δ changes with Ra . In Figure 4.17, we plot the measured δ / H as a function of the Rayleigh number in the smooth cell (solid circles) and in the rough cell at the position T (open triangles) and position V (solid triangles). While the number of data points is not enough to establish a power law, the data are certainly consistent with the $\delta / H \sim Ra^{-2/7}$ scaling. The solid lines show THE fitted power-laws: $4.5 \times Ra^{-2/7}$ (top solid line), $3.25 \times Ra^{-2/7}$ (middle solid line), and $2.05 \times Ra^{-2/7}$ (bottom solid line). For the smooth cell, one can also obtain the boundary layer thickness from the measured $Nu(Ra)$ via the relation $\delta = \frac{H}{2Nu}$. Using the measured transport result of $Nu = 0.17Ra^{2/7}$ in Sec. 4.1, we have $\delta / H = 2.94 \times Ra^{-2/7}$, which is very close to the direct measurement of δ in the smooth cell shown in Fig. 4.17.

The surface roughness affects not only the mean temperature profile $T(z)$ but also the RMS profile $T_{RMS}(z)$. Figure 4.18 compares the measured $T_{RMS}(z)$ in the smooth cell (circles) with those in the rough cell at the position V [triangles in Fig. 4.18(a)] and position T [triangles in Fig. 4.18(b)]. To view the near-wall portion of $T_{RMS}(z)$ more clearly, we use a logarithmic scale for z . The RMS profile is obtained from the time series measurements using the equation $T_{RMS}(z) = \left\langle (T(z) - \bar{T})^2 \right\rangle^{1/2}$, where \bar{T} is the mean temperature of the local fluid. It is seen from Fig. 4.18 that the measured $T_{RMS}(z)$ has a well-defined peak located at the edge of the thermal boundary layer, suggesting that the boundary layer is a strongly fluctuating structure. Indeed, this has been observed in the flow visualization. The value of $T_{RMS}(z)/\Delta T$ is peaked at $\sim 7\%$ and decays gradually to a value of $\sim 1\%$ at the center of the cell. As shown in Fig. 4.18(a), the measured $T_{RMS}(z)$

near the tip has a similar shape as that in the smooth cell, but the peak position is shifted toward the boundary. This is because the thermal boundary layer near the tip is thinner than that in the smooth cell.

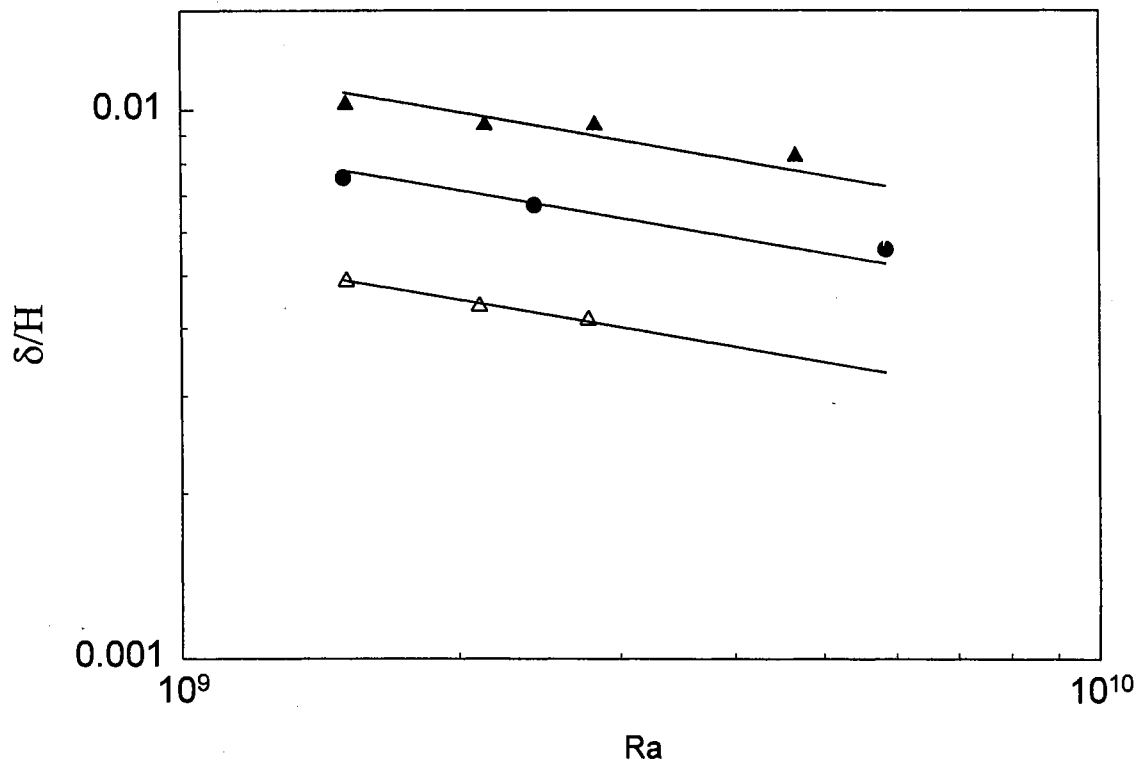


Figure 4.17 Measured δ/H as function of Ra in the smooth cell (solid circles) and in the rough cell at the position T (open triangles) and position V (solid triangles). The solid lines show the $Ra^{2/7}$ power law.

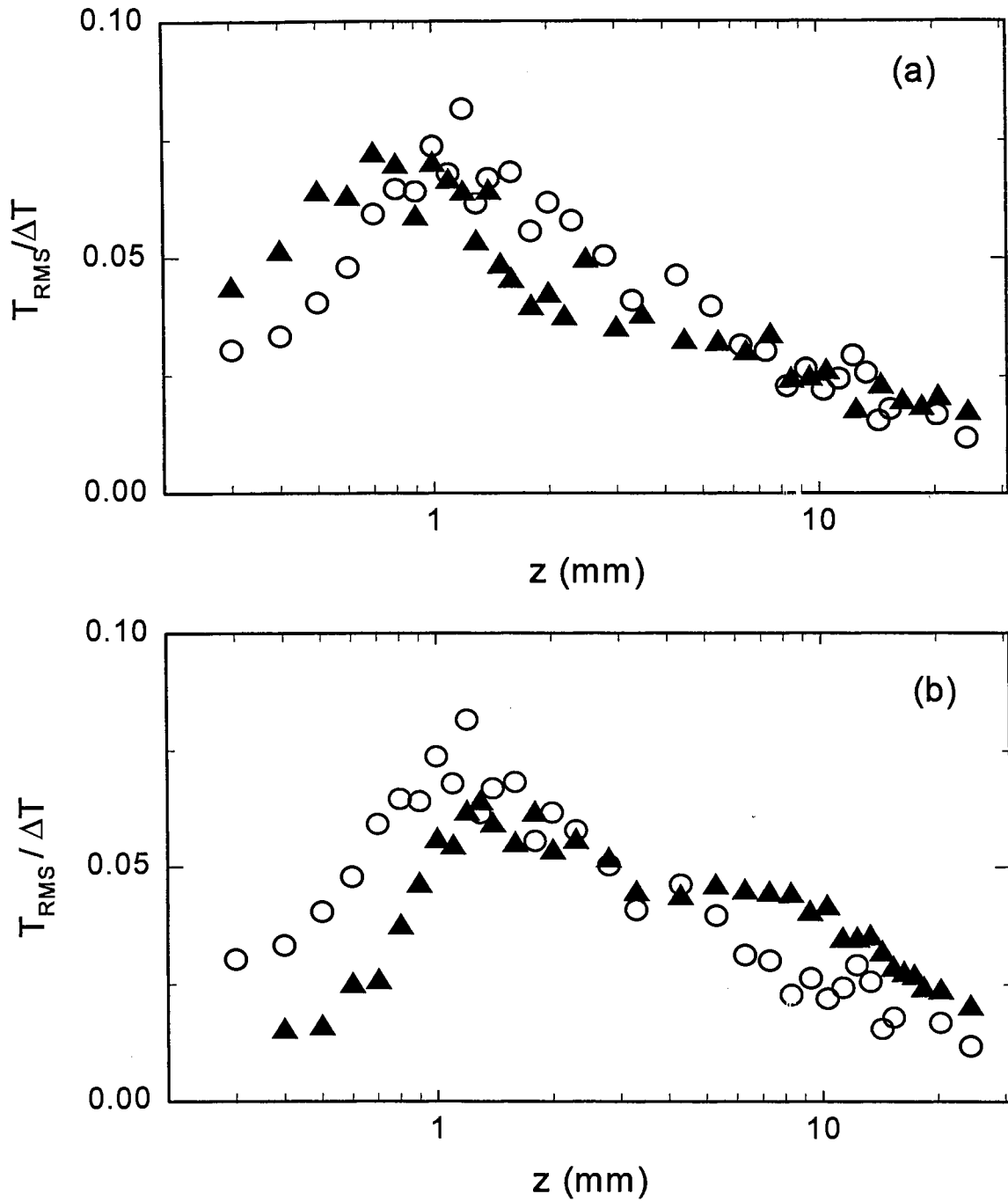


Figure 4.18 (a) Measured RMS temperature profile $T_{RMS}(z)$ in the smooth cell (circles) and in the rough cell at the position T (triangles) at $Ra = 1.5 \times 10^9$. In the plot $T_{RMS}(z)$ is normalized by the temperature difference ΔT . (b) Measured $T_{RMS}(z)$ in the smooth cell and in the rough cell at the position V (triangles) at $Ra = 1.5 \times 10^9$.

The triangles in Fig. 4.18(b) show the measured $T_{RMS}(z)$ in the groove region. The peak position of $T_{RMS}(z)$ is shifted away from the boundary, because the boundary layer in the groove region becomes thicker than that in the smooth cell. As discussed in the last section, the small eddies trapped inside the groove produce a strong mixing effect, which creates large temperature fluctuations. It is seen from Fig. 4.18(b) that the measured $T_{RMS}(z)$ inside the groove region ($z < h$) is increased by more than 100%. Another interesting feature shown in Fig. 4.18(b) is that the influence of the surface roughness extends way into the central region, in which the measured $T_{RMS}(z)$ is still considerably larger than that in the smooth cell. From the measurements at the center of the rough cell (see Chapter V), we find that the temperature histogram remains the same exponential form as that in the smooth cell and the measured $T_{RMS}(z)/\Delta T$ as a function of Ra obeys the same $Ra^{-1/7}$ scaling law. However, the power law amplitude in the rough cell is increased by $\sim 35\%$. It becomes clear now that the rough elements on the surface play an active role in the emission dynamics of the thermal plumes. Rather than simply sheltering the groove region from the large-scale circulation, the rough elements help to create a secondary flow (eddies) in the groove region. This secondary flow together with the large-scale circulation enhance the detachment of the thermal boundary layer near the tip of the pyramids. In the groove region, the secondary flow produces a strong eddy mixing effect, which suppresses the emission of the thermal plumes, and at the same time creates large temperature fluctuations outside the thermal boundary layer.

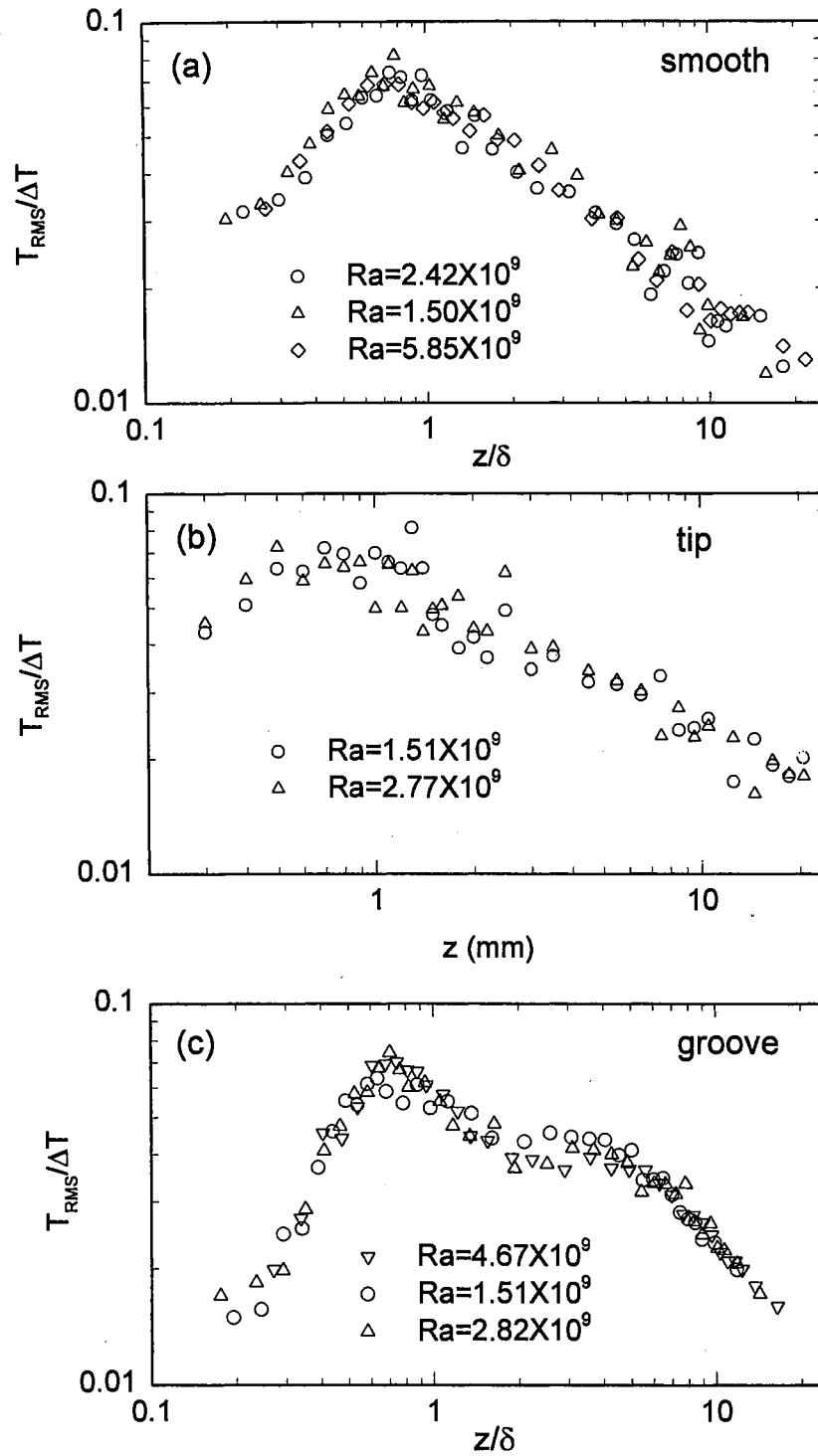


Figure 4.19 Measured $T_{RMS}(z)$ in the smooth cell (a) and in the rough cell at the position T (b) and position V (c) for different values of Ra . In the plot $T_{RMS}(z)$ is normalized by the temperature difference ΔT .

We now discuss the Ra -dependence of $T_{RMS}(z)$. Figure 4.19 shows the measured $T_{RMS}(z)$ in the smooth cell (a) and in the rough cell at the position T (b) and position V (c) for different values of Ra . Similar to the mean temperature profile $T(z)$, the RMS profile $T_{RMS}(z)$ in the smooth cell also scales with δ . As shown in Fig. 4.19(a), plots of $T(z)$ vs. z/δ for different Ra remain invariant and only δ changes with Ra . The value of $T_{RMS}(z)/\Delta T$ is peaked at $\sim 7\%$ and does not change very much with Ra . The measured $T_{RMS}(z)$ outside the boundary layer decreases with increasing z and can be fit to a function $T_{RMS}(z)/\Delta T \sim \ln z$. The fit has relatively large uncertainties because of the large scatters in the measured $T_{RMS}(z)$. Experimental uncertainties for $T_{RMS}(z)$ are largely statistical due to the relatively short duration for the time series measurements. The measurements of $T_{RMS}(z)$ in water agree well with the previous measurements in a smooth cell filled with high-pressure gases [11]. The scaling behavior of the measured $T_{RMS}(z)/\Delta T$ suggests that the temperature fluctuations in the smooth cell of aspect ratio one are controlled by a universal mechanism.

The RMS profiles measured in the rough cell have a similar scaling behavior as those in the smooth cell. Figure 4.19(b) shows the measured $T_{RMS}(z)$ in the rough cell at the position T. Since the boundary layer thickness near the tip does not change very much with Ra , we plot the measured $T_{RMS}(z)$ as a function of z instead of z/δ . Because temperature fluctuations near the tip are stronger and the thermal boundary layer is very thin, it becomes difficult to determine δ accurately and the RMS data have relatively larger statistical uncertainties near the tip. Nevertheless, one can still see from Fig. 4.19 (b) that the RMS profiles for different Ra have a similar shape. As discussed above, the

temperature fluctuations in the groove region are enhanced greatly because of the eddy mixing effect. It is seen from Fig. 4.19(c) that the measured $T_{RMS}(z)/\Delta T$ reaches a maximum value of 7% at the edge of the thermal boundary layer, remains a constant value of 4% throughout the groove region, and then decreases with further increasing z outside the rough surface. The shape of the measured $T_{RMS}(z)$ for different Ra remains unchanged and only δ changes with Ra . The fact that the measured $T_{RMS}(z)$ remains constant inside the groove region suggests that the small eddies are very effective in homogenizing the temperature fluctuations in the region. These findings further confirm that the small eddies trapped in the groove region play an important role in the boundary dynamics near the rough surface.

CHAPTER V

TEMPERATURE FLUCTUATIONS AT THE CELL CENTER

In this chapter we discuss the local temperature measurements in the central region of the convection cells.

5.1 Local temperature fluctuations and their statistics

We first discuss the local temperature measurements at the center of the smooth and rough cells with the aspect ratio $A=1$. Figure 5.1 shows typical time series measurements of $T(t)$ in the smooth cell [Fig. 5.1(a)] and in the rough cell [Fig. 5.1(b)]. The local temperature $T(t)$ is normalized such that the mean temperature of the top plate is 0 and that of the bulk fluid is 0.5. Both measurements are made in the hard turbulence regime [4] at $Ra=1.5\times 10^9$. The temperature fluctuations at the cell center are characterized by intermittent sharp spikes of variable heights and more fluctuations are found in the rough cell. To learn the distribution of temperature fluctuations, we compute their histogram from the time series data. Figure 5.2 (a) shows the temperature histogram $H(\delta T)$ in the smooth cell at $Ra=4.33\times 10^9$. The horizontal variable, $\delta T/\Delta T \equiv (T - \bar{T})/\Delta T$, represents the fluctuation of the local temperature T about its mean \bar{T} and is normalized by the temperature difference ΔT . In the plot 6×10^5 data points are used to compute $H(\delta T)$. This corresponds to a continuous real-time measurement of

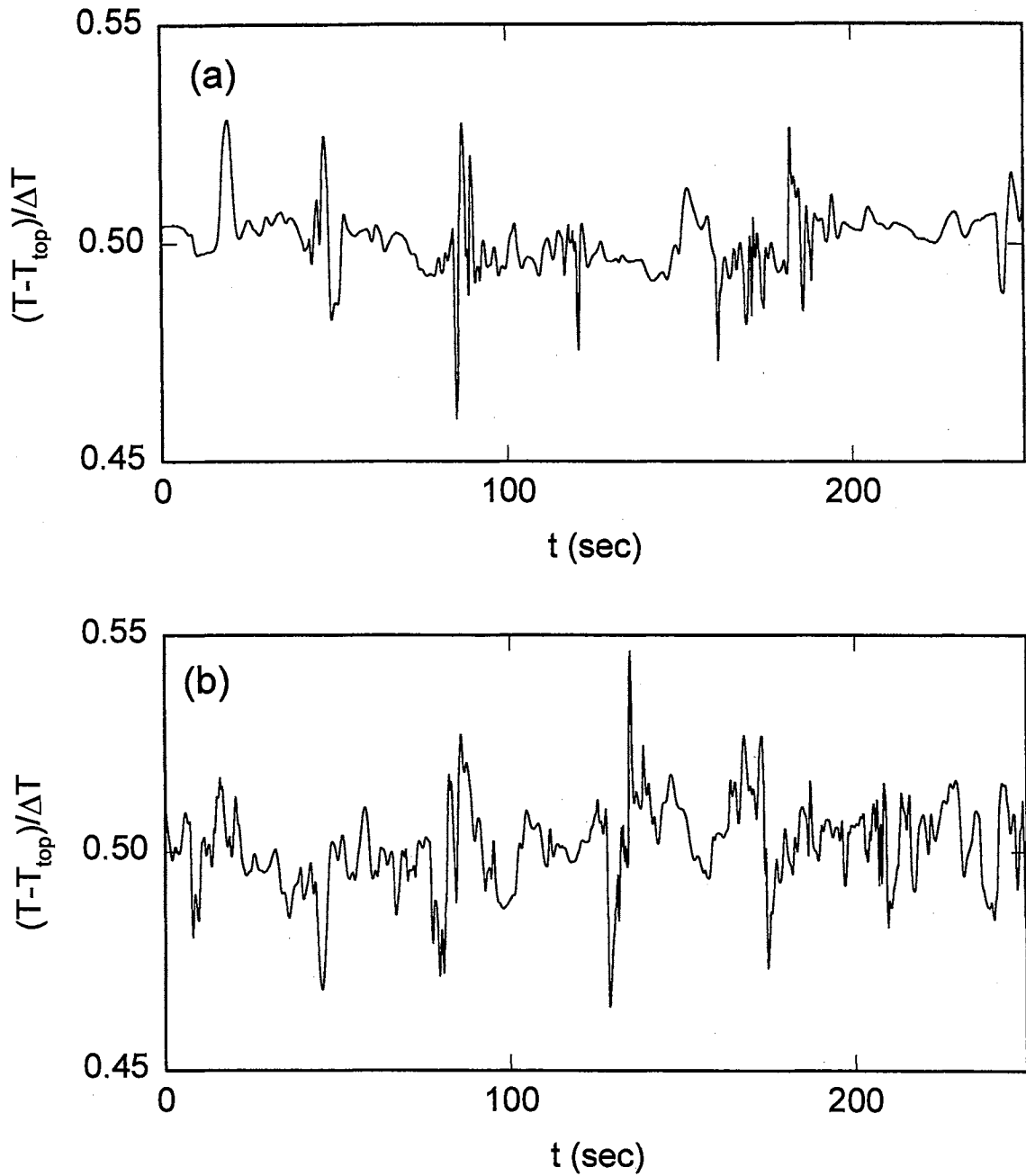


Figure 5.1 Typical time series measurements of temperature fluctuations at the center of (a) the $A=1$ smooth cell and (b) the $A=1$ rough cell. The local temperature $T - T_{top}$ relative to the top plate temperature T_{top} is normalized by the temperature difference ΔT across the cell. Both measurements are made at $Ra = 1.5 \times 10^9$.

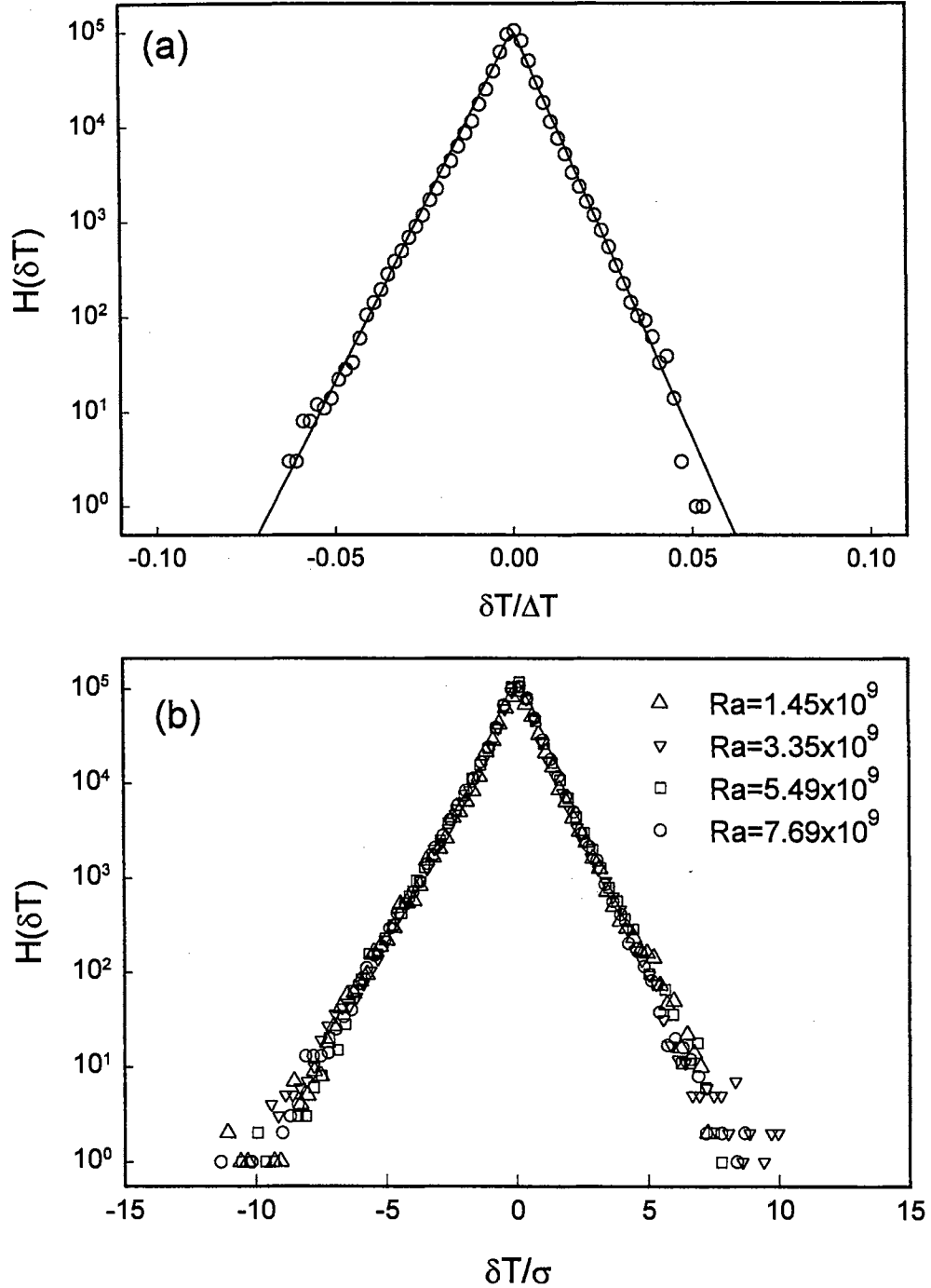


Figure 5.2 (a) Measured temperature histogram $H(\delta T)$ at the center of the $A=1$ smooth cell. The horizontal variable, $\delta T/\Delta T \equiv (T - \bar{T})/\Delta T$, represents the fluctuation of the local temperature T about its mean \bar{T} and is normalized by the temperature difference ΔT . The measurement is made at $Ra = 4.33 \times 10^9$ and the solid lines are the linear fits. (b) Measured $H(\delta T)$ as a function of $\delta T/\sigma$ for different values of Ra at the center of the $A=1$ smooth cell.

8.3 hours. It is seen from Fig. 5.2(a) that the measured $H(\delta T)$ at the cell center has a simple exponential form over an amplitude range of more than 4 decades. The straight lines in Fig. 5.2(a) show the linear fits to the data points. The absolute values of the slope for the two straight lines are slightly different (<10%), suggesting that the temperature distribution is somewhat asymmetric. This asymmetry could be caused by the fact that the temperature probe may not be placed exactly at the cell center.

We now examine how the histogram $H(\delta T)$ changes with the Rayleigh number. It is found that the measured $H(\delta T)$ for different values of Ra can all be brought into coincidence, once δT is scaled by its RMS value $\sigma = \langle (T - \bar{T})^2 \rangle^{1/2}$. The plot of $H(\delta T)$ vs. $\delta T/\sigma$ remains invariant and only σ changes with Ra . Figure 5.2(b) shows the measured $H(\delta T)$ as a function of $\delta T/\sigma$ for four different values of Ra . The scaling behavior of the measured $H(\delta T)$ suggests that the structure of the turbulent temperature field in the central region is invariant with Ra . The width of the temperature distribution, i.e., the RMS value σ , is found to decrease with increasing Ra , indicating that the temperature fluctuations are reduced as the flow becomes more turbulent. Similar scaling behavior has been observed previously in a smooth cell filled with low temperature helium gas [5]. We will discuss the Ra -dependence of the measured σ later in conjunction with the results from the rough cell.

Figure 5.3 compares the temperature histogram $H(\delta T)$ obtained in the rough cell at $Ra = 2.11 \times 10^9$ (triangles) with that in the smooth cell at $Ra = 2.34 \times 10^9$ (solid curve). It is seen that the measured $H(\delta T)$ in the rough cell is of the same exponential form as that in the smooth cell, but has a larger value of σ . This suggests that temperature

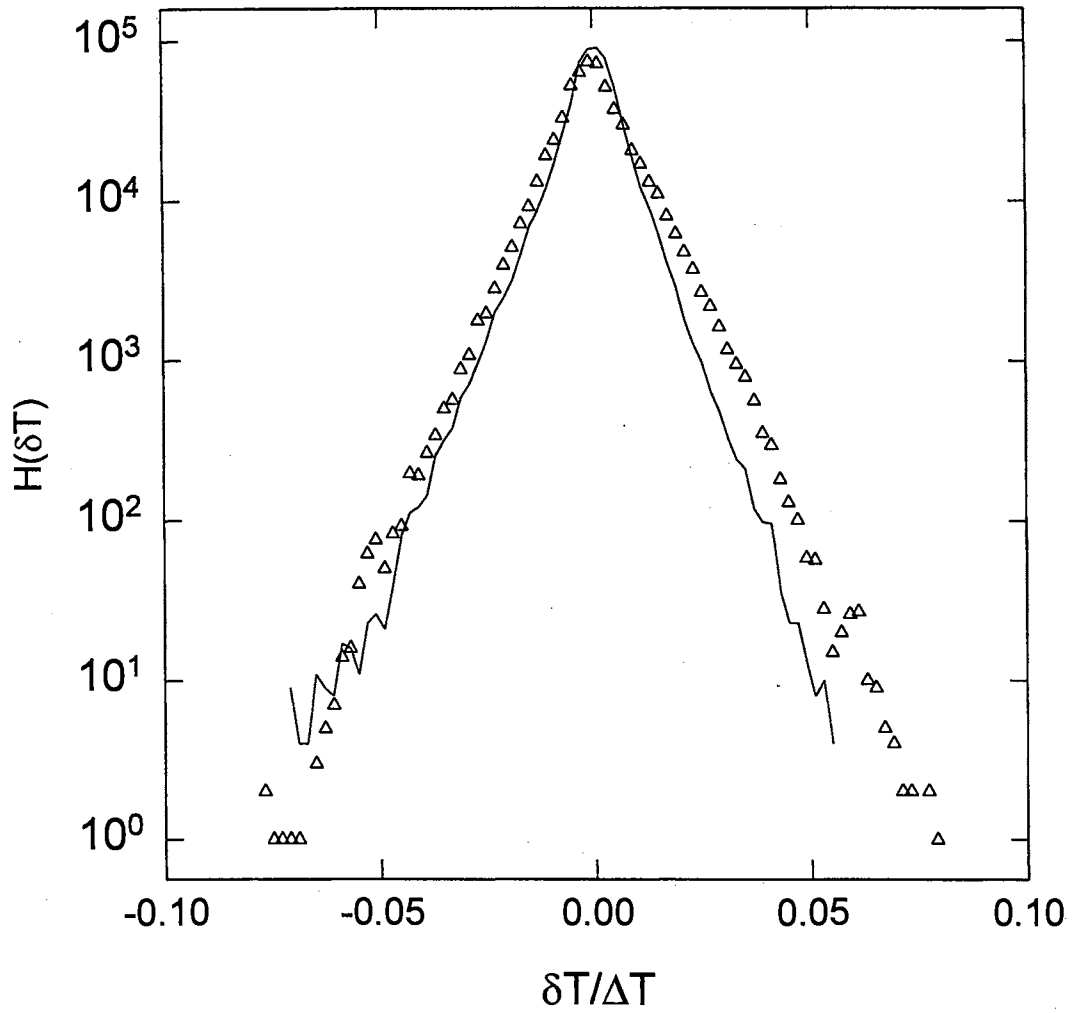


Figure 5.3 Comparison of the temperature histograms between the $A=1$ smooth cell (solid curve) and the $A=1$ rough cell (triangles). The measurements are made at $Ra = 2.34 \times 10^9$ for the smooth cell and at $Ra = 2.11 \times 10^9$ for the rough cell.

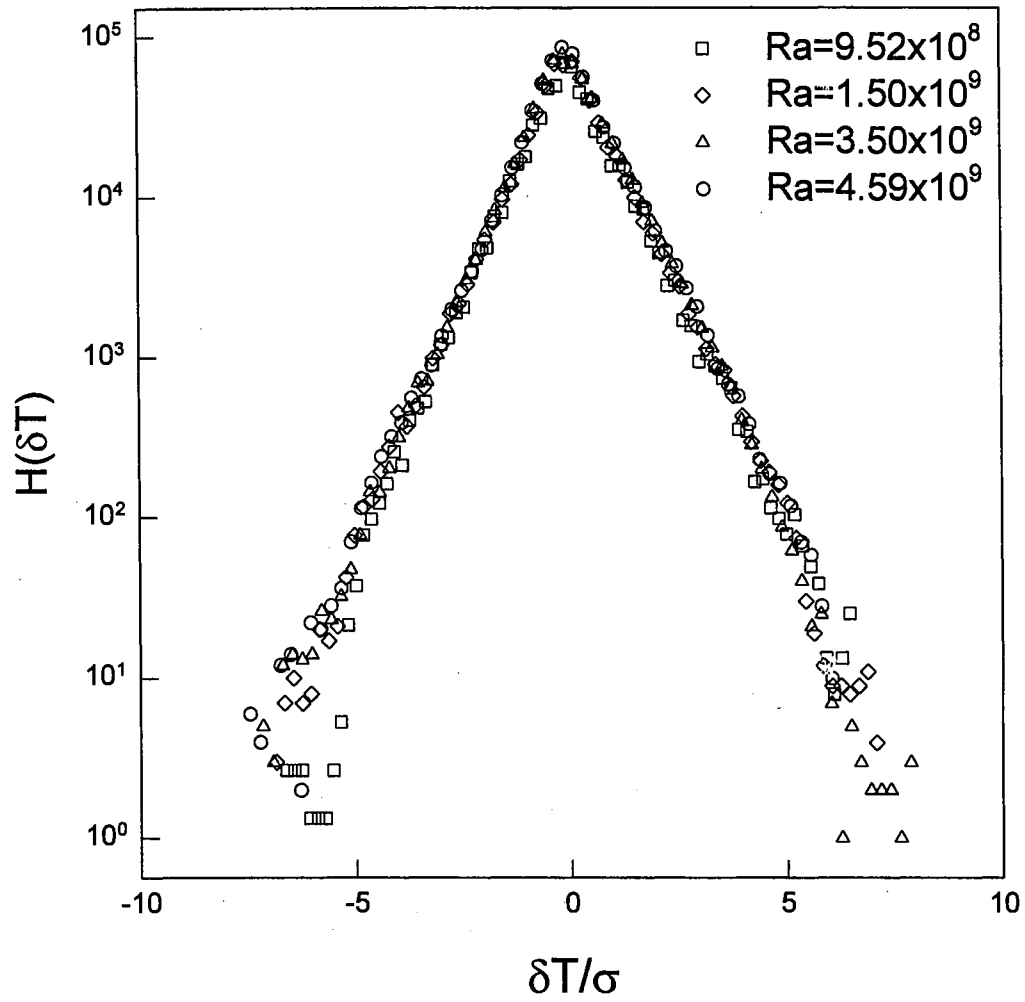


Figure 5.4 Measured temperature histogram $H(\delta T)$ as a function of $\delta T/\sigma$ for different values of Ra at the center of the $A=1$ rough cell.

fluctuations are increased considerably in the rough cell, which is consistent with the direct observation shown in Fig. 5.1. Figure 5.4 shows the measured $H(\delta T)$ as a function of $\delta T/\sigma$ for different values of Ra at the center of the $A=1$ rough cell. Similar to those obtained in the smooth cell, the measured $H(\delta T)$ in the rough cell also scales with $\delta T/\sigma$. It is seen from Fig. 5.4 that over an amplitude range of almost 5 decades, all the temperature histograms measured in the rough cell exhibit the same exponential shape and do not change with Ra . The scaling behavior of the measured $H(\delta T)$ suggests that the structure of the turbulent temperature field in the central region of the rough cell remains the same as that in the smooth cell and is invariant with Ra .

Figure 5.5 shows the instantaneous flow field in the $A=1$ rough cell [Fig. 5.5(a)] and in the $A=1$ smooth cell [Fig. 5.5(b)] both at $Ra = 2.6 \times 10^9$. The displayed region covers approximately top 2/3 of the convection cell and the exposure time for the streak images is 0.5 s. It is clearly seen from Fig. 5.5 that there is a large-scale circulation in both the rough and smooth cells and the “eye” of the circulation is approximately located at the cell center. Recent local velocity measurements [42, 12] in the smooth cell have shown that in the central region velocity fluctuations are, and are much larger than the mean velocity, which is approximately equal to zero. We believe that this conclusion also applies to the velocity field in the rough cell. Near the boundary, however, the large-scale circulation is found to persist over a long period of time and its velocity is unidirectional with a mean value much larger than the fluctuations [42, 15]. It is seen from Fig. 5.5(a) that there are several small eddies trapped in the groove region. These eddies together with the large-scale flow cause the eruption of the thermal plumes near the tip of the pyramids. The arrow in Fig. 5.5(a) indicates a cold plume, which just

erupted from the tip. Because the eruption of the thermal plumes over the rough surface is driven mainly by the large-scale flow rather than the buoyancy force, the vortex ring associated with the buoyancy acceleration disappears and thus most thermal plumes in the rough cell lose their mushroom cap.

We now discuss temperature fluctuations at the center of the tall convection cells with $A=0.5$. Figure 5.6 shows typical time series measurements of the local temperature $T(t)$ at the center of the smooth cell [Fig. 5.6(a)] and the rough cell [Fig. 5.6(b)]. The measurements are made at $Ra = 1.24 \times 10^{10}$ for the smooth cell and at $Ra = 8.21 \times 10^9$ for the rough cell, both are in the hard turbulence regime. Similar to those in the $A=1$ cells, the temperature fluctuations in the $A=0.5$ cells are characterized by sharp spikes of variable heights and are of intermittent nature. A new feature shown in Fig. 5.6 is that the cold and warm spikes are superposed on a base line, which changes with time slowly. This is in contrast with Fig. 5.1, in which the spikes are superposed on a fairly stable base line. The time scale for the slow baseline variation is ~ 60 s, which is comparable to the time necessary to move the fluid from the top to the bottom of the cell [42]. It has been suggested that this slow baseline variation is caused by the fact that the large-scale circulation becomes unstable in the $A=0.5$ cell [43, 44]. As will be shown below, because of the unstable large-scale circulation, the RMS value σ in the $A=0.5$ cells becomes larger than that in the $A=1$ cells.

The temperature histograms in the $A=0.5$ smooth cell show a similar scaling behavior as those in the $A=1$ smooth cell. As shown in Fig. 5.7(a), the measured $H(\delta T)$ for different values of Ra are symmetric and remain invariant with Ra , once δT is scaled by its RMS value σ . A new feature shown in Fig. 5.7(a) is that the shape of the measured

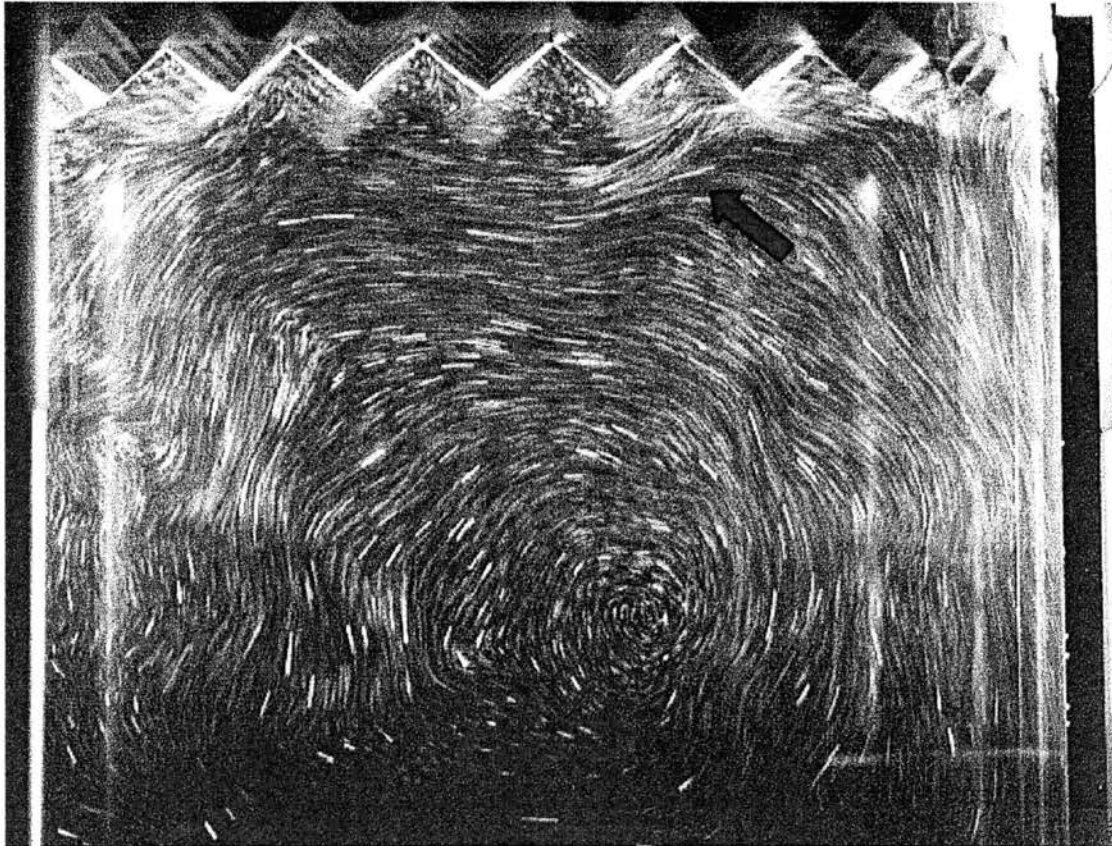


Figure 5.5(a) A Streak image of the seeded TLC spheres taken in the $A=1$ rough cell at $Ra = 2.6 \times 10^9$. Cold eruptions are brown; green and blue regions are warmer. The displayed region covers approximately top 2/3 of the convection cell and its dimension is 20 cm by 14 cm. The arrow indicates a thermal plume, which just erupted from the tip of a pyramid.

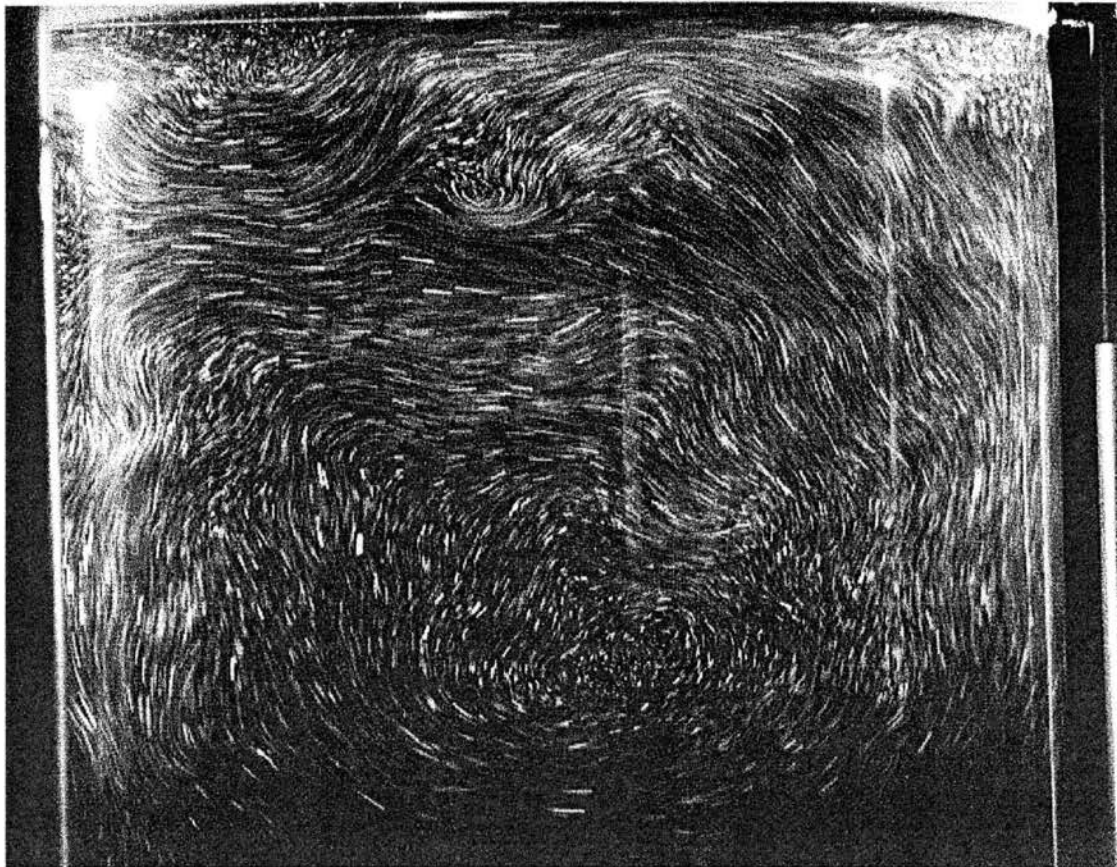


Figure 5.5(b) A Streak image of the seeded TLC spheres taken in the $A=1$ smooth cell at $Ra = 2.6 \times 10^9$. The displayed region covers approximately top 2/3 of the convection cell and its dimension is 20 cm by 14 cm.

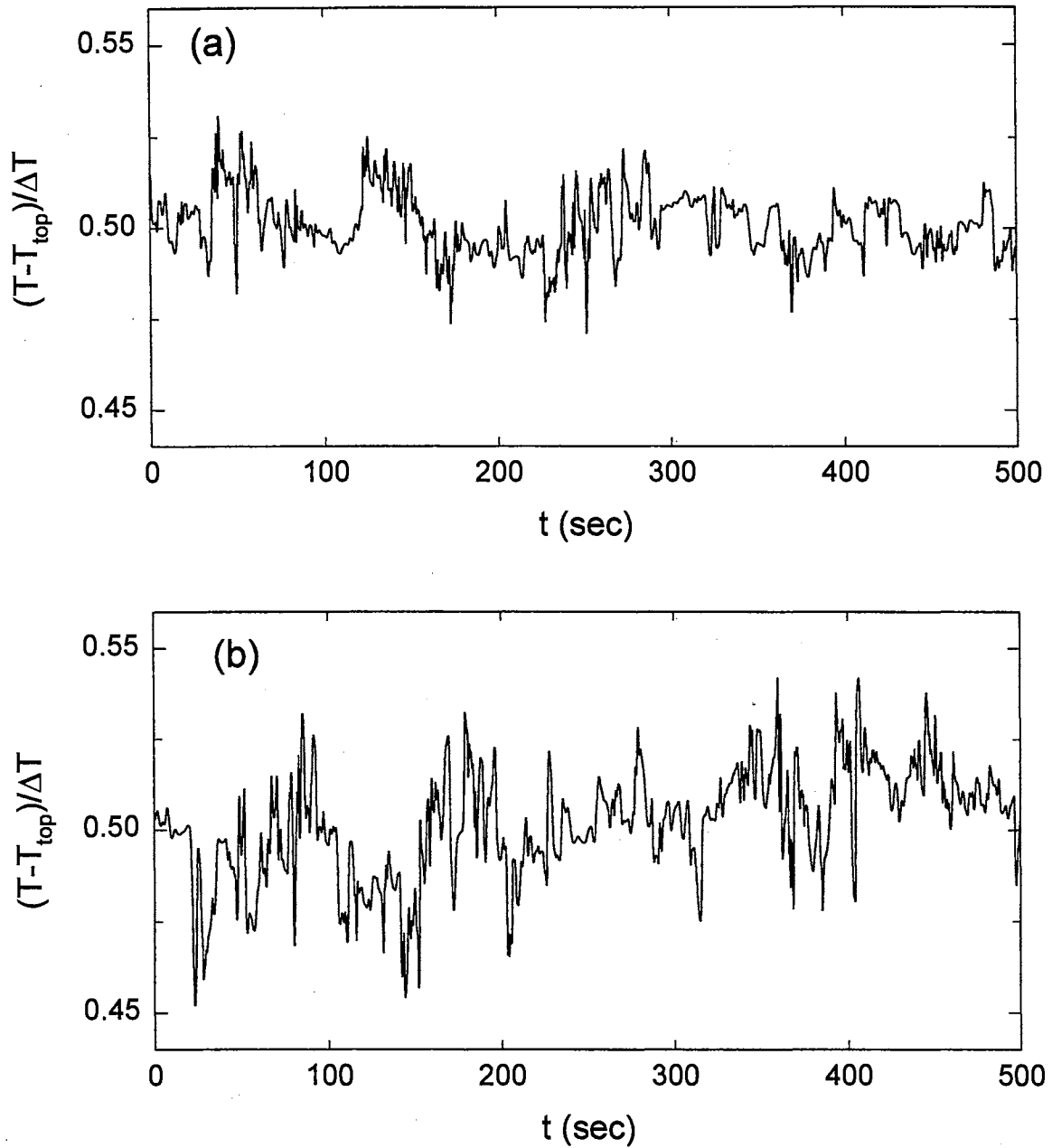


Figure 5.6 Typical time series measurements of the temperature fluctuations at the center of (a) the $A=0.5$ smooth cell and (b) the $A=0.5$ rough cell. The measurements are made at $Ra = 1.24 \times 10^{10}$ for the smooth cell and at $Ra = 8.21 \times 10^9$ for the rough cell.

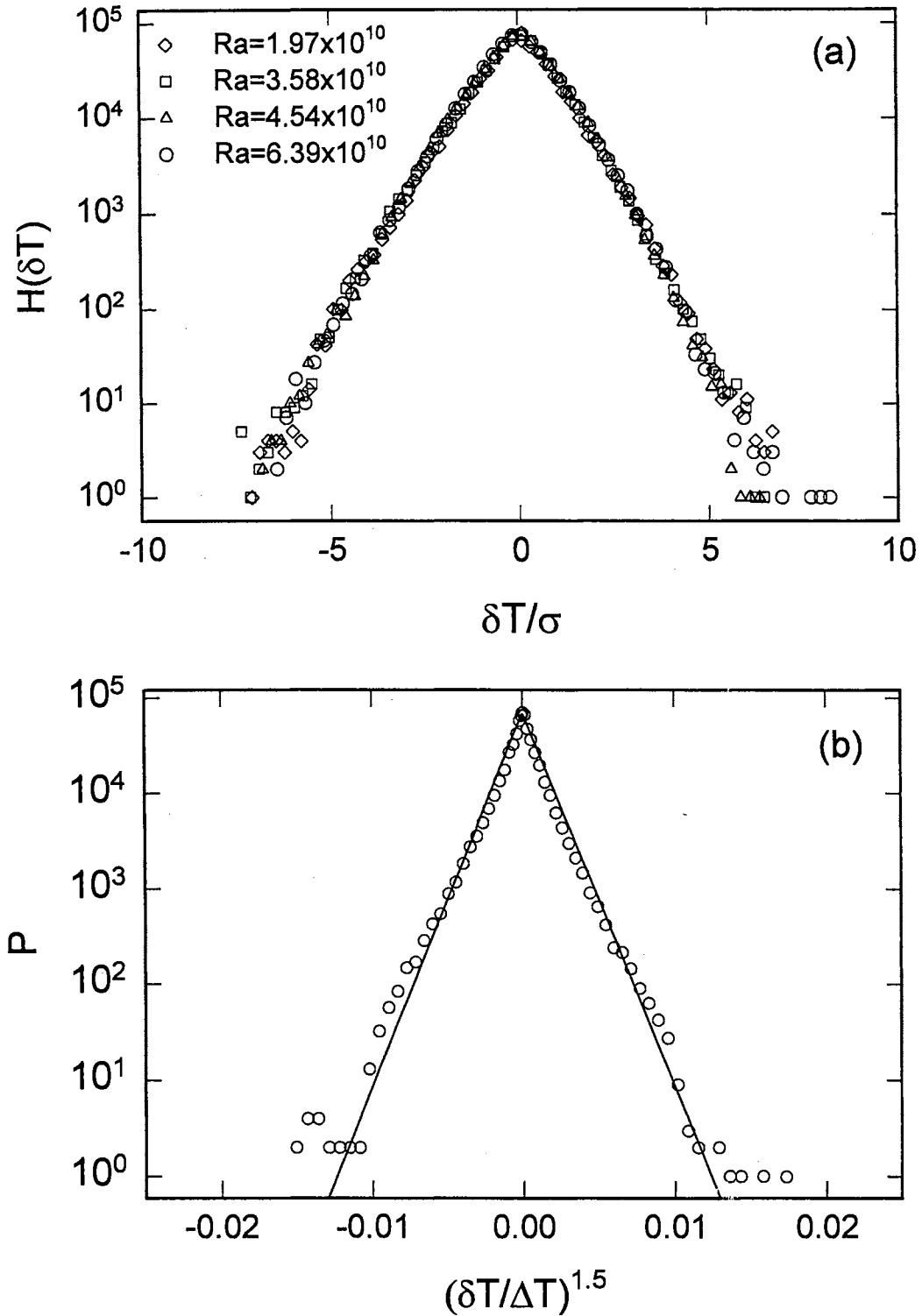


Figure 5.7 (a) Measured temperature histogram $H(\delta T)$ as a function of $\delta T/\sigma$ for different values of Ra at the center of the $A=0.5$ smooth cell. (b) Measured $H(\delta T)$ as a function of $(\delta T/\sigma)^{1.5}$ in the $A=0.5$ smooth cell at $Ra = 2.75 \times 10^{10}$. The solid lines are the linear fits.

$H(\delta T)$ in the $A=0.5$ cell is no longer of simple exponential form. The unstable large-scale circulation produces a round cusp for the temperature histogram, which can be fitted by a stretched exponential function. In Fig. 5.7(b) we plot the measured $H(\delta T)$ as a function of $(\delta T/\Delta T)^{1.5}$ in the $A=0.5$ smooth cell at $Ra = 2.75 \times 10^{10}$. The straight lines show the stretched exponential function $H(\delta T) = H_0 \exp[-\kappa(\delta T/\Delta T)^{1.5}]$ with $H_0 = 70000$ and $\kappa = 900$.

Figure 5.8 shows the measured $H(\delta T)$ as a function of $(\delta T/\Delta T)^{1.5}$ in the $A=0.5$ rough cell (triangles) and in the $A=0.5$ smooth cell (solid curve). The Rayleigh numbers for the two measurements are very close, one is $Ra = 2.98 \times 10^{10}$ (rough cell) and the other is $Ra = 2.75 \times 10^{10}$ (smooth cell). It is seen that the measured $H(\delta T)$ in the rough cell is of the same shape as that in the smooth cell, but has a larger value of σ . Figure 5.9 shows the measured $H(\delta T)$ as a function of $\delta T/\sigma$ for different values of Ra at the center of the $A=0.5$ rough cell. Similar to the situation in the $A=0.5$ smooth cell, the measured $H(\delta T)$ in the rough cell also scales with $\delta T/\sigma$. It is seen from Fig. 5.9 that over an amplitude range of almost 5 decades, all the temperature histograms have the same stretched exponential shape and do not change with Ra .

Finally, we examine how the RMS value σ changes with Ra . Figure 5.10(a) shows the normalized RMS value $\sigma/\Delta T$ as a function of Ra at the center of the smooth cells (circles) and the rough cells (triangles). The solid symbols represent the data obtained from the $A=0.5$ cells and the open symbols are from the $A=1$ cells. The measured $\sigma/\Delta T$ in the smooth cells is well described by the power law $\sigma/\Delta T = aRa^{-\gamma}$ (solid lines). In both $A=1$ and $A=0.5$ cells the exponent $\gamma=0.14$, which agrees well with

the previous measurements using low temperature helium gas [5, 44]. As discussed above, the unstable large-scale circulation in the $A=0.5$ cell produces larger temperature fluctuations and thus the power-law amplitude a in the $A=0.5$ cell is increased from 0.153 to 0.253. The measured $\sigma/\Delta T$ in the rough cells can also be described by a power law with the same exponent γ , but the amplitude a is changed from 0.153 to 0.192 for the $A=1$ cell and from 0.253 to 0.33 for the $A=0.5$ cell (dashed lines). The measured σ in the rough cells is thus increased by 25-30% when compared with the value in the smooth cells. Similar scaling behavior is also observed when the temperature probe is moved away from the cell center. Figure 5.10(b) shows the measured $\sigma/\Delta T$ as a function of Ra when the movable thermistor is placed at distance $z=2.4$ cm away from the upper cold surface. The solid and dashed lines are the power-law fits to the corresponding data sets. The fitted functions are: $\sigma/\Delta T = 0.28Ra^{-1/7}$ (left solid line), $\sigma/\Delta T = 0.38Ra^{-1/7}$ (right solid line), $\sigma/\Delta T = 0.39Ra^{-1/7}$ (left dashed line), and $\sigma/\Delta T = 0.54Ra^{-1/7}$ (right dashed line). Figure 5.10 thus demonstrates that the measured $\sigma/\Delta T$ as a function of Ra in different cells and at different spatial positions can all be described by a simple power law with a common exponent $\gamma=1/7$, but the power-law amplitude may change with the spatial position and type of the cells.

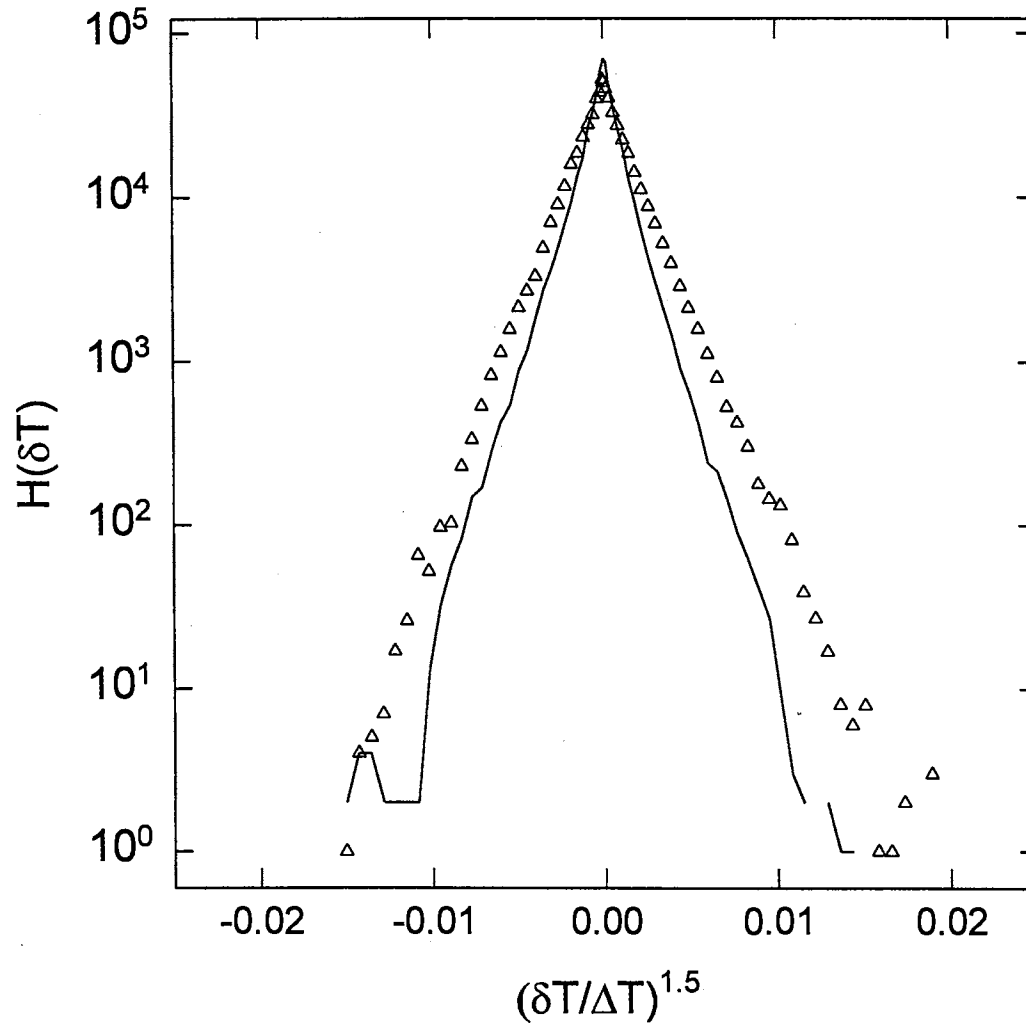


Figure 5.8 Comparison of the temperature histograms between the $A=0.5$ smooth cell (solid curve) and the $A=0.5$ rough cell (triangles). The measurements are made at $Ra = 2.75 \times 10^{10}$ for the smooth cell and at $Ra = 2.98 \times 10^{10}$ for the rough cell.

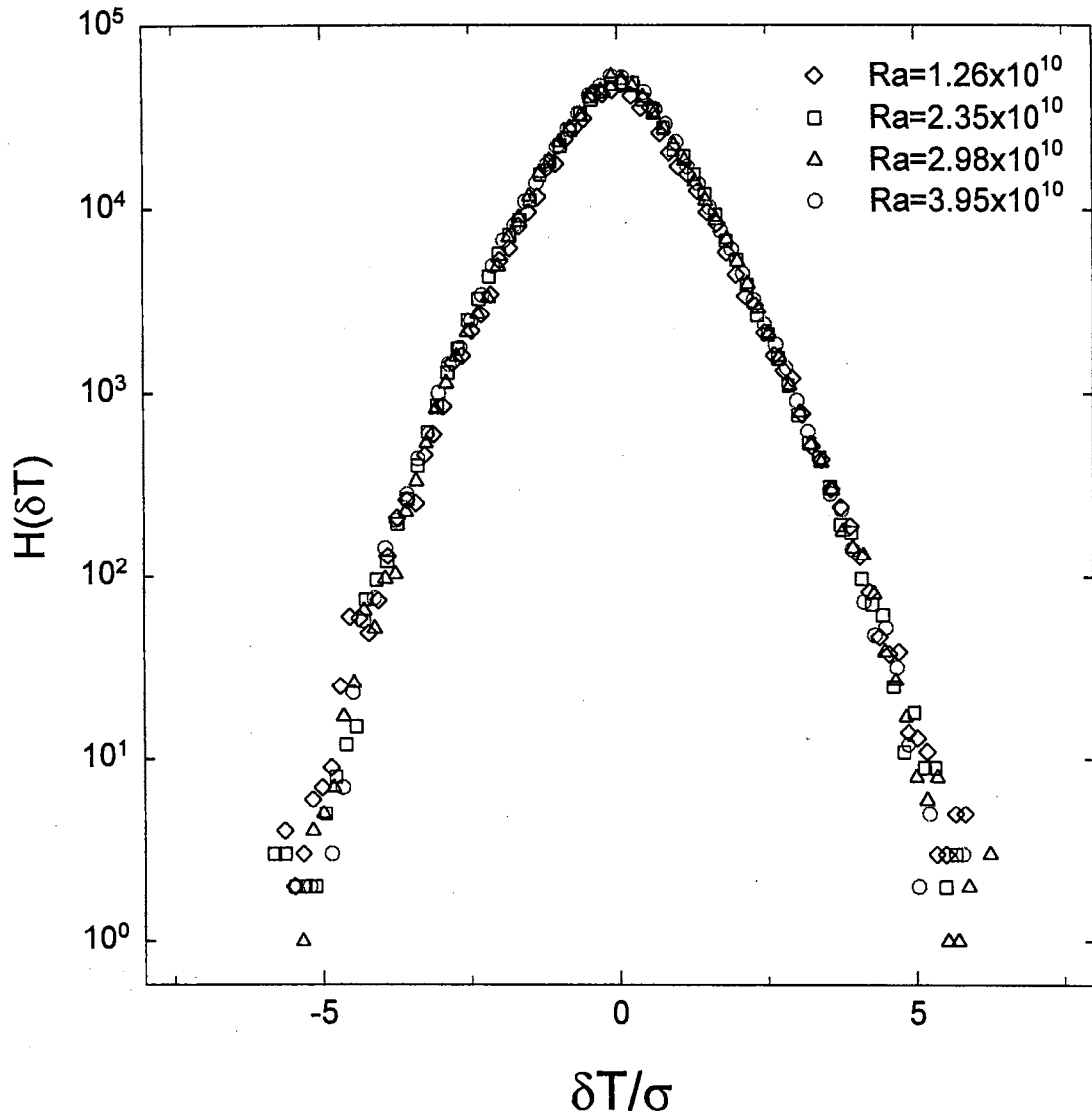


Figure 5.9 Measured temperature histogram $H(\delta T)$ as a function of $\delta T/\sigma$ for different values of Ra at the center of the $A=0.5$ rough cell.

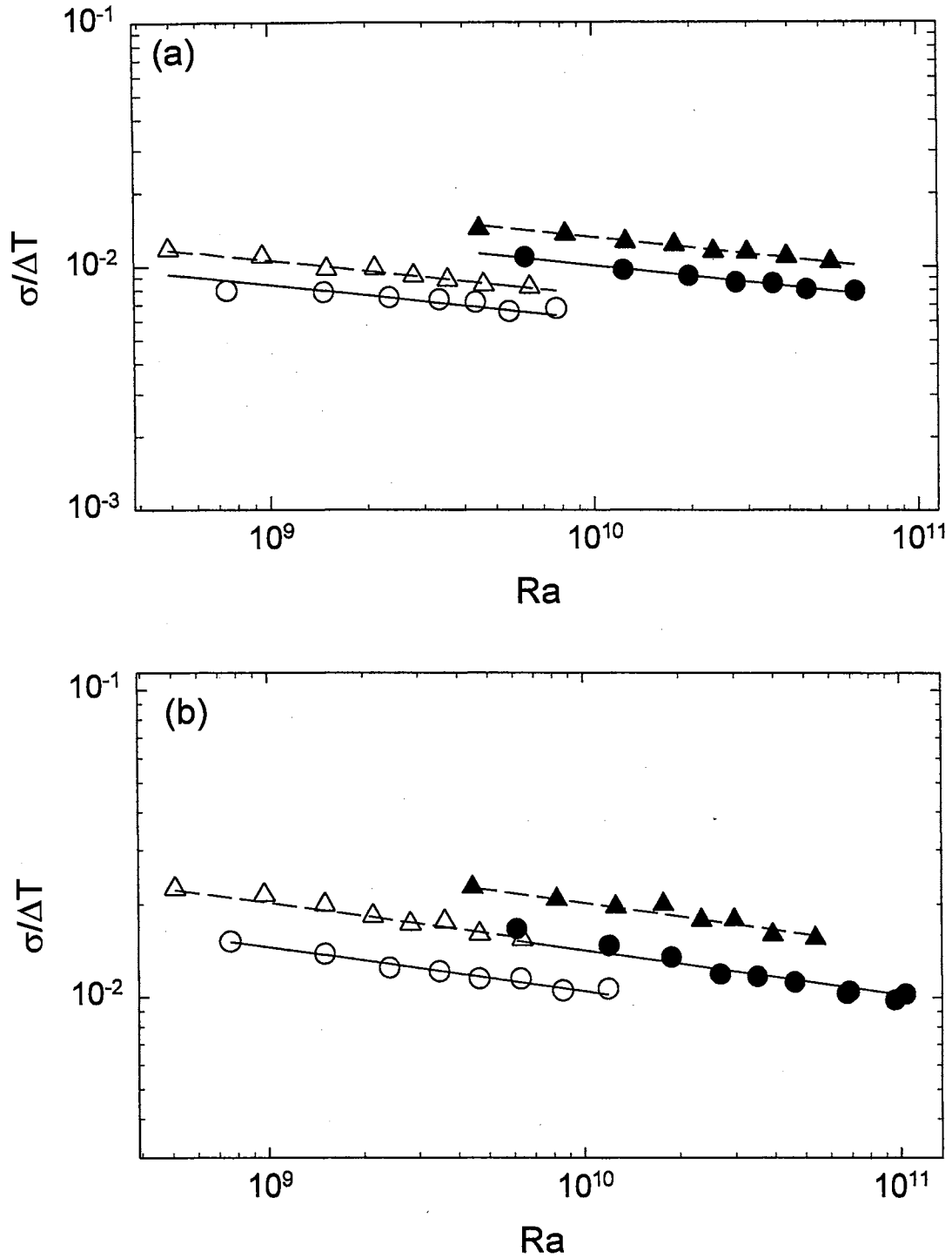


Figure 5.10 Normalized RMS value $\sigma/\Delta T$ as a function of Ra in the smooth cells (circles) and in the rough cells (triangles). The local temperature measurements are conducted (a) at the cell center and (b) at distance $z=2.4$ cm away from the upper cold surface. The solid symbols represent the data obtained from the $A=0.5$ cells and the open symbols are from the $A=1$ cells. The solid and dashed lines are the power-law fits to the circles and triangles, respectively.

5.2 Frequency power spectrum of temperature fluctuations

To understand the dynamics of temperature fluctuations at small length scales, we use a LabVIEW program [45] to compute the frequency power spectrum $P(f)$ of the measured $T(t)$:

$$P(f) = \left| \int_{-\infty}^{+\infty} T(t) e^{-i2\pi ft} dt \right|^2. \quad (5.1)$$

The calculation of $P(f)$ is carried out first for 1024 data points with the Hanning window, and then the result is averaged over all the data files. Typically, 580 averages are performed to obtain the final $P(f)$. The sampling rate for the temperature measurement is $f_s = 20\text{Hz}$, and therefore the frequency range of $P(f)$ is in between $f_s/2 = 10\text{Hz}$ and $f_s/1024 = 0.0019\text{Hz}$.

Figure 5.11(a) shows the measured power spectrum $P(f)$ as a function of f at the center of the $A=1$ smooth cell. The measurements are made in the hard turbulence regime with $Ra = 1.47 \times 10^9$ (bottom curve), 3.35×10^9 (middle curve), and 7.69×10^9 (top curve). Previous measurements with low temperature helium gas [6] have shown that the lower-frequency part of $P(f)$ exhibits a power-law range, which increases with Ra . The dashed line in Fig. 5.11(a) indicates the power-law $P(f) \sim f^{-\alpha}$ with the exponent $\alpha=1.2$. Because of the limited range of f , the value of α is found to scatter in a range between 1.2 and 1.3 in our working range of Ra . This value of α is close to the Bolgiano-Obukhov scaling of $7/5$, which is predicted for the turbulent energy cascade in thermal stratification [46, 47, 48, 6, 49]. However, it was pointed out recently that similar scaling exponents have also been found for a passive scalar behind a cylinder and in a turbulent boundary layer [3]. In the high frequency region, the measured $P(f)$ drops

sharply and can be described by a stretched exponential function $P(f) = P_0 \exp[-(f/f_c)^{0.6}]$, where f_c is a cut-off frequency and P_0 is an amplitude. In Fig. 5.11(b) we plot the measured $P(f)$ as a function of $f^{0.6}$. The high-frequency part of the measured $P(f)$ appears as a straight line in this plot, indicating that it is indeed of the stretched exponential form, which does not change with Ra . It will be shown in next section that the sharp decay of $P(f)$ at the high frequency is caused by the dissipation of turbulent energy and we will discuss the Ra -dependence of the cut-off frequency f_c later together with the rough cell results.

The power spectra in the $A=0.5$ smooth cell show a similar behavior as those in the $A=1$ cell. Figure 5.12(a) depicts the measured $P(f)$ as a function of f for three different values of Ra at the center of the $A=0.5$ smooth cell. The low-frequency power-law range of the measured $P(f)$ is found to be slightly wider than that shown in Fig. 5.11(a) and the value of the power-law exponent $\alpha = 1.3 \pm 0.1$ (the dashed line), which is in good agreement with the previous measurements [48, 6, 49]. In the high frequency region, the measured $P(f)$ is found to be of the same stretched exponential form $P(f) = P_0 \exp[-(f/f_c)^{0.6}]$. As shown in Fig. 5.12(b), plots of $P(f)$ as a function of $f^{0.6}$ appear as straight lines, indicating that they are indeed of the stretched exponential form and do not change with Ra .

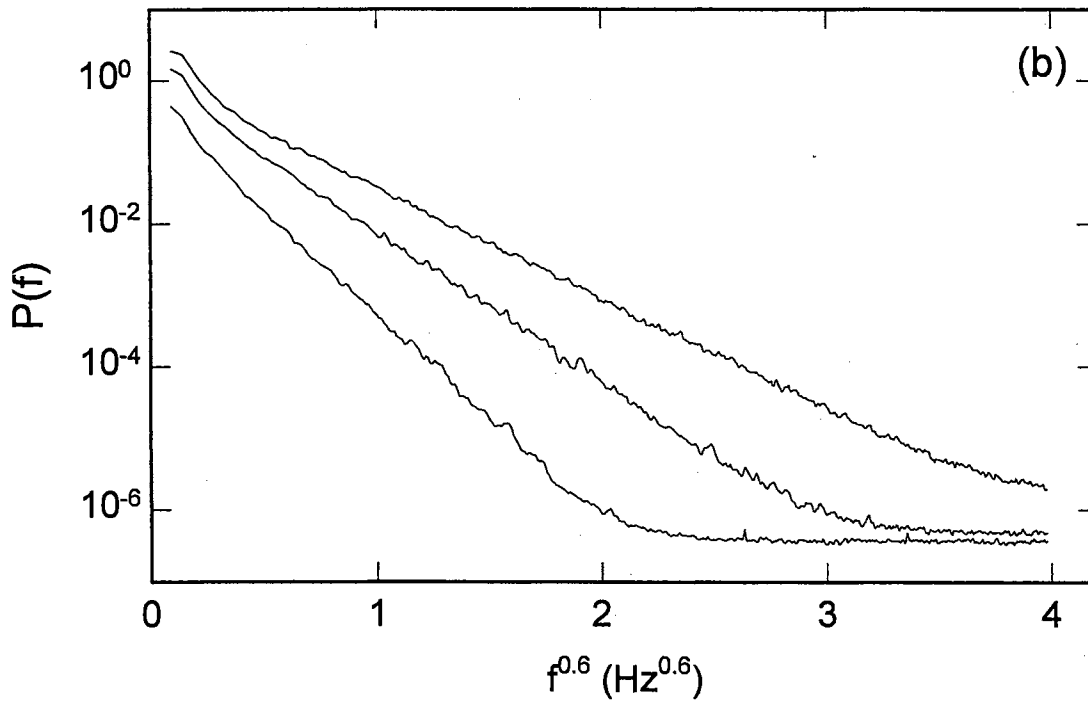
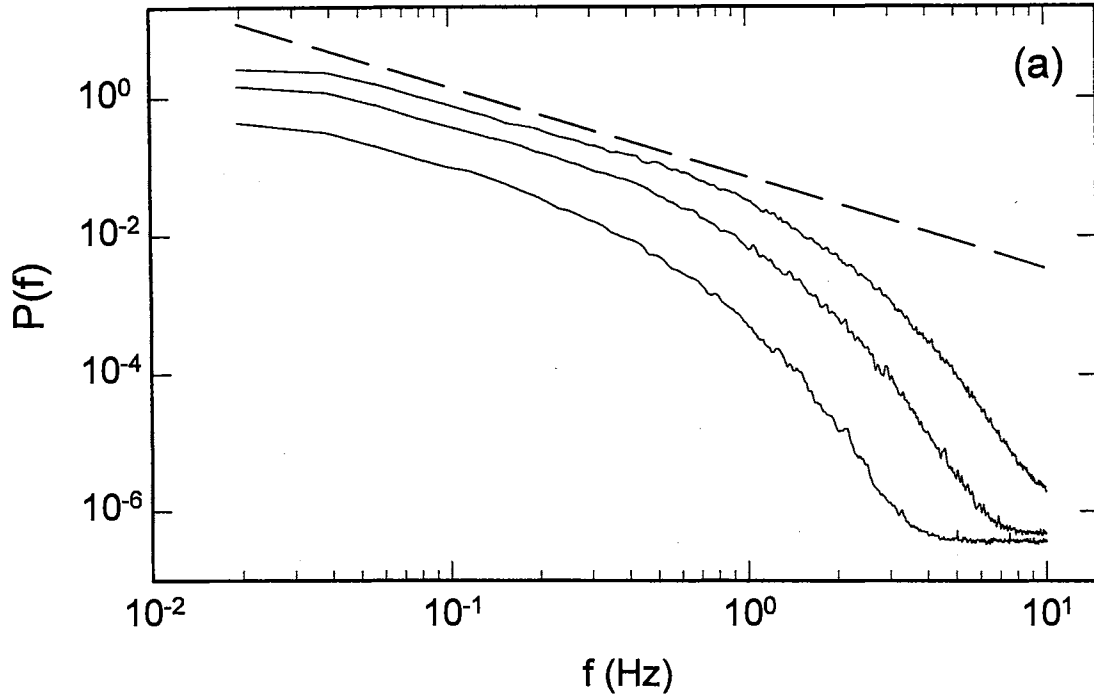


Figure 5.11 (a) Measured power spectrum $P(f)$ as a function of f for three different values of Ra at the center of the $A=1$ smooth cell. The values of Ra are: 1.47×10^9 (bottom curve), 3.35×10^9 (middle curve), and 7.69×10^9 (top curve). The dashed line indicates the power law $P(f) \sim f^{-1.2}$. (b) Plots of $P(f)$ as a function of $f^{0.6}$ for the same data.

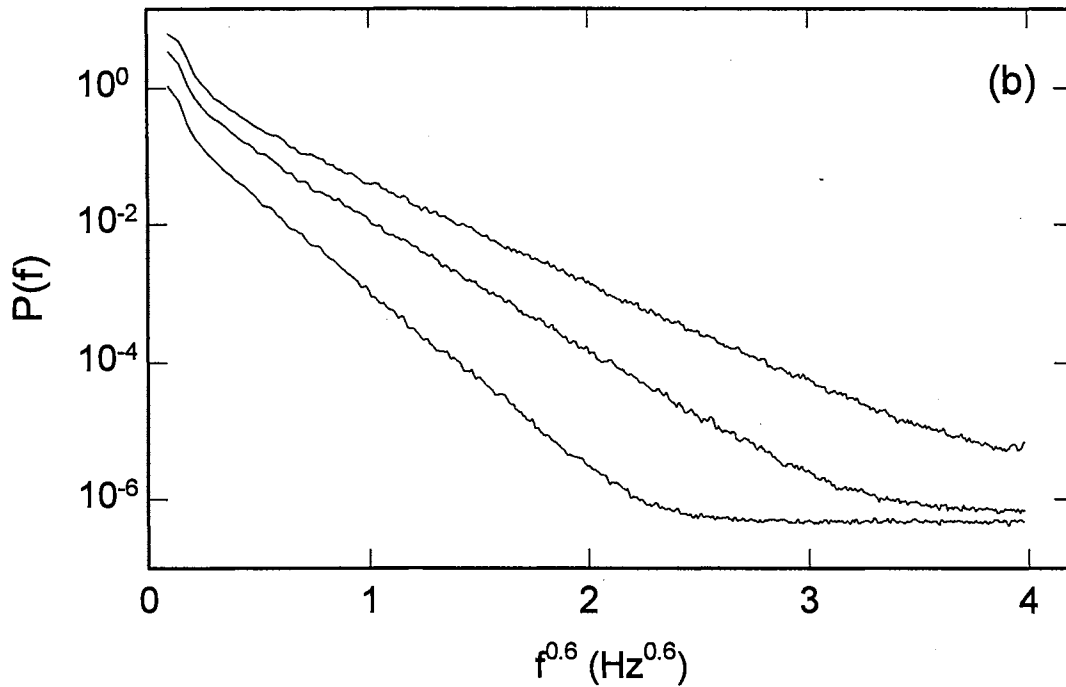
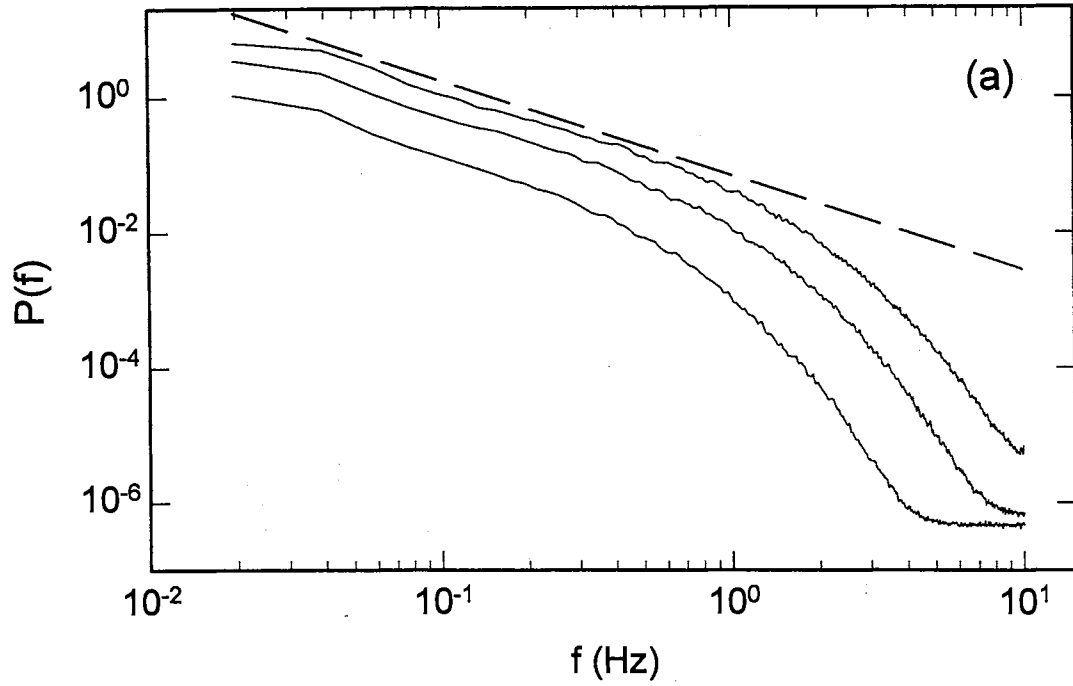


Figure 5.12 (a) Measured power spectrum $P(f)$ as a function of f for three different values of Ra at the center of the $A=0.5$ smooth cell. The values of Ra are: 1.24×10^{10} (bottom curve), 2.75×10^{10} (middle curve), and 6.39×10^{10} (top curve). The dashed line indicates the power law $P(f) \sim f^{-1.3}$. (b) Plots of $P(f)$ as a function of $f^{0.6}$ for the same data.

The power spectra in the rough cells have the same shape as those in the smooth cells. Figure 5.13 compares the measured $P(f)$ in the $A=1$ rough cell (upper curve) with that in the $A=1$ smooth cell (lower curve). The Rayleigh numbers for the two measurements are very close, one is $Ra = 2.34 \times 10^9$ (smooth cell) and the other is $Ra = 2.11 \times 10^9$ (rough cell). It is seen that the measured $P(f)$ in the rough cell is of the same shape as that in the smooth cell, but has a slightly larger amplitude. The larger amplitude in $P(f)$ is caused by the fact that temperature fluctuations are increased in the rough cell and the power spectrum $P(f)$ is related to the RMS value σ by

$$\int_0^{+\infty} P(f) df = \sigma^2 \quad (5.2)$$

Figure 5.14(a) shows the measured $P(f)$ as a function of f for three different values of Ra at the center of the $A=1$ rough cell. The dashed line indicates the power law $P(f) \sim f^{-1.3}$. It is seen that the measured $P(f)$ decays quickly in the high frequency region immediately after the power-law decay. Figure 5.14(b) demonstrates that the high frequency part of $P(f)$ in the rough cell has the same stretched exponential form as that in the smooth cell.

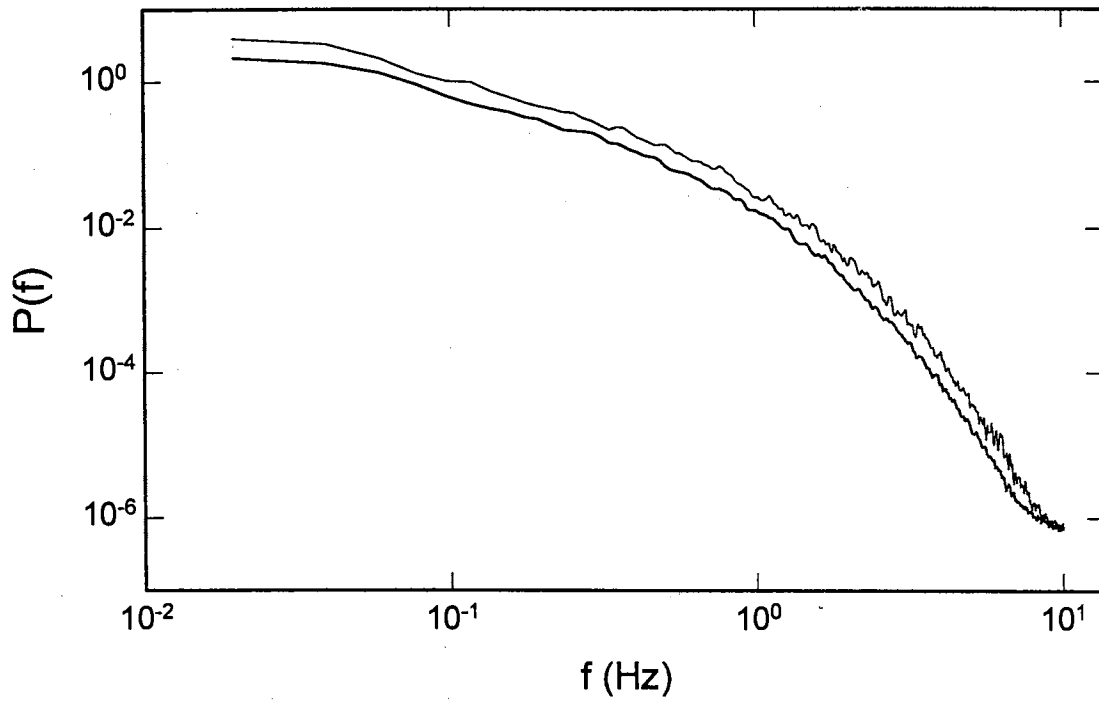


Figure 5.13 Comparison of the power spectra in the $A=1$ smooth cell (lower curve) and in the $A=1$ rough cell (upper curve). The measurements are made at $Ra = 2.34 \times 10^9$ for the smooth cell and at $Ra = 2.11 \times 10^9$ for the rough cell.

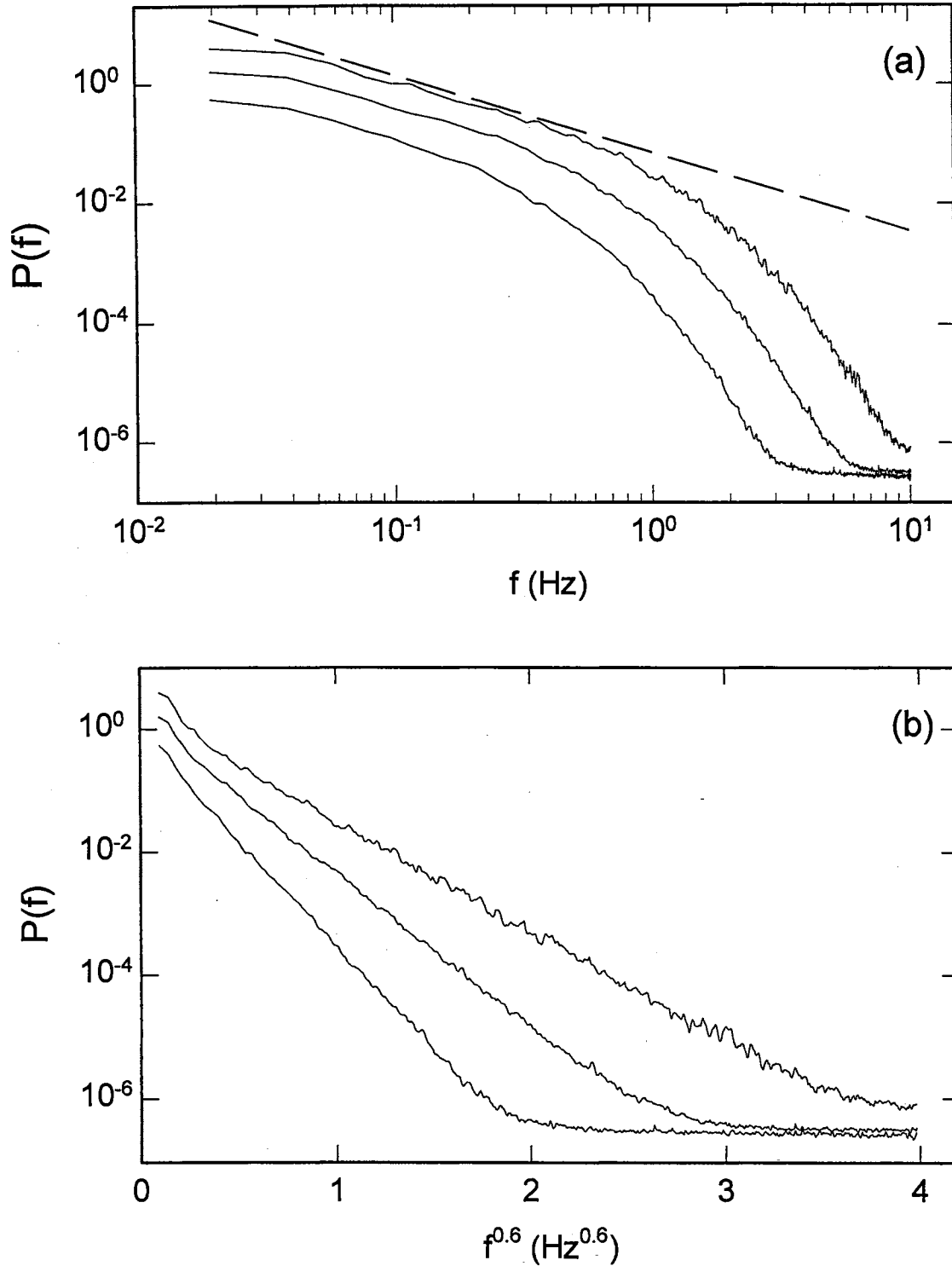


Figure 5.14 (a) Measured power spectrum $P(f)$ as a function of f for three different values of Ra at the center of the $A=1$ rough cell. The values of Ra are: 9.52×10^8 (bottom curve), 2.11×10^9 (middle curve), and 4.59×10^9 (top curve). The dashed line indicates the power law $P(f) \sim f^{-1.3}$. (b) Plots of $P(f)$ as a function of $f^{0.6}$ for the same data.

5.3 Energy dissipation in turbulent convection

We now discuss the Ra -dependence of the cut-off frequency f_c and its physical significance. In the experiment, we obtain f_c from the slope of the straight line in the plot of $P(f)$ vs. $f^{0.6}$. Figure 5.15(a) shows the cut-off frequency f_c as a function of Ra in the smooth cells (circles) and in the rough cells (triangles). The solid symbols represent the data obtained from the $A=0.5$ cells, and the open symbols are from the $A=1$ cells. It is found that the measured f_c in the rough cells remains the same as that in the corresponding smooth cells. The solid lines in Fig. 5.15(a) show the power-law fits to the data and the fitting results are: $f_c = 4.8 \times 10^{-8} Ra^{0.68}$ (left solid line) and $f_c = 1.3 \times 10^{-8} Ra^{0.68}$ (right solid line). This fitting indicates that the power-law exponent remains the same for both the $A=1$ and $A=0.5$ cells, but the amplitude in the $A=1$ cells is approximately 4 times larger than that in the $A=0.5$ cells.

The cut-off frequency f_c has been measured previously in other fluid systems, such as liquid mercury [50, 14], low temperature helium gas [43, 48, 49], and room temperature compressed gases (helium, nitrogen, or sulfur hexafluoride) [10, 11]. Because of the complicated shape of the measured $P(f)$ and the limited frequency range, f_c was obtained in these experiments by assuming different functional forms for the high-frequency cut-off of $P(f)$. In the present study of convection in water and early measurements in low temperature helium gas [43, 6], the high-frequency part of $P(f)$ is fitted to a stretched exponential function and the fitting is independent of the low-frequency power-law region of $P(f)$. The low temperature helium data have also been analyzed with a classical exponential cut-off for $P(f)$ together with a low-frequency

power-law dependence in f [6, 48, 49]. The obtained f_c from the exponential cut-off is found to have the same Ra -dependence as that from the stretched exponential cut-off, but the magnitude is increased by a factor of 3.3 [6]. In the experiment with compressed gases [10, 11], the cut-off frequency f_c is simply defined as the frequency where the power spectrum intersects the noise level of the experiment. It is seen from Figs. 5.11(a) and 5.15(a) that the cut-off frequency defined in this way is approximately 80 times larger than that obtained from the stretched exponential cut-off.

It has been found that the measured f_c in the smooth cells can be well described by a power law $f_c \sim Ra^{-\xi}$, but the exponent ξ varies in different fluid systems. In helium gas ($Pr \sim 0.7$), the value of ξ is found to be ~ 0.78 both at the center of the cell [43, 48, 49] and near the thermal boundary layers [10, 11]. In liquid mercury ($Pr=0.024$), however, one finds $\xi \sim 0.4$ [14], which is approximately a factor of 2 smaller than that in helium gas. As shown in Fig. 5.15(a), the value of ξ obtained in water ($Pr=5.4$) is 0.68, which is in between the two values mentioned above. These measurements indicate that the value of ξ may depend on the Prandtl number of the convecting fluid Pr . It has been suggested [49, 10, 14] that the cut-off frequency f_c is determined by the size l_c of the smallest fluctuation in convection and the corresponding characteristic velocity u_c . If one chooses the thermal boundary layer thickness $\delta = H/(2Nu)$ [11] as l_c and the RMS velocity $v_{rms} = 2.2 \times 10^{-5} Ra^{3/7}$ at the cell center [12] as u_c , we have

$$\frac{f_c H^2}{\kappa} = \frac{v_{rms} H^2}{\kappa \delta} \approx 0.026 Ra^{5/7}, \quad (5.3)$$

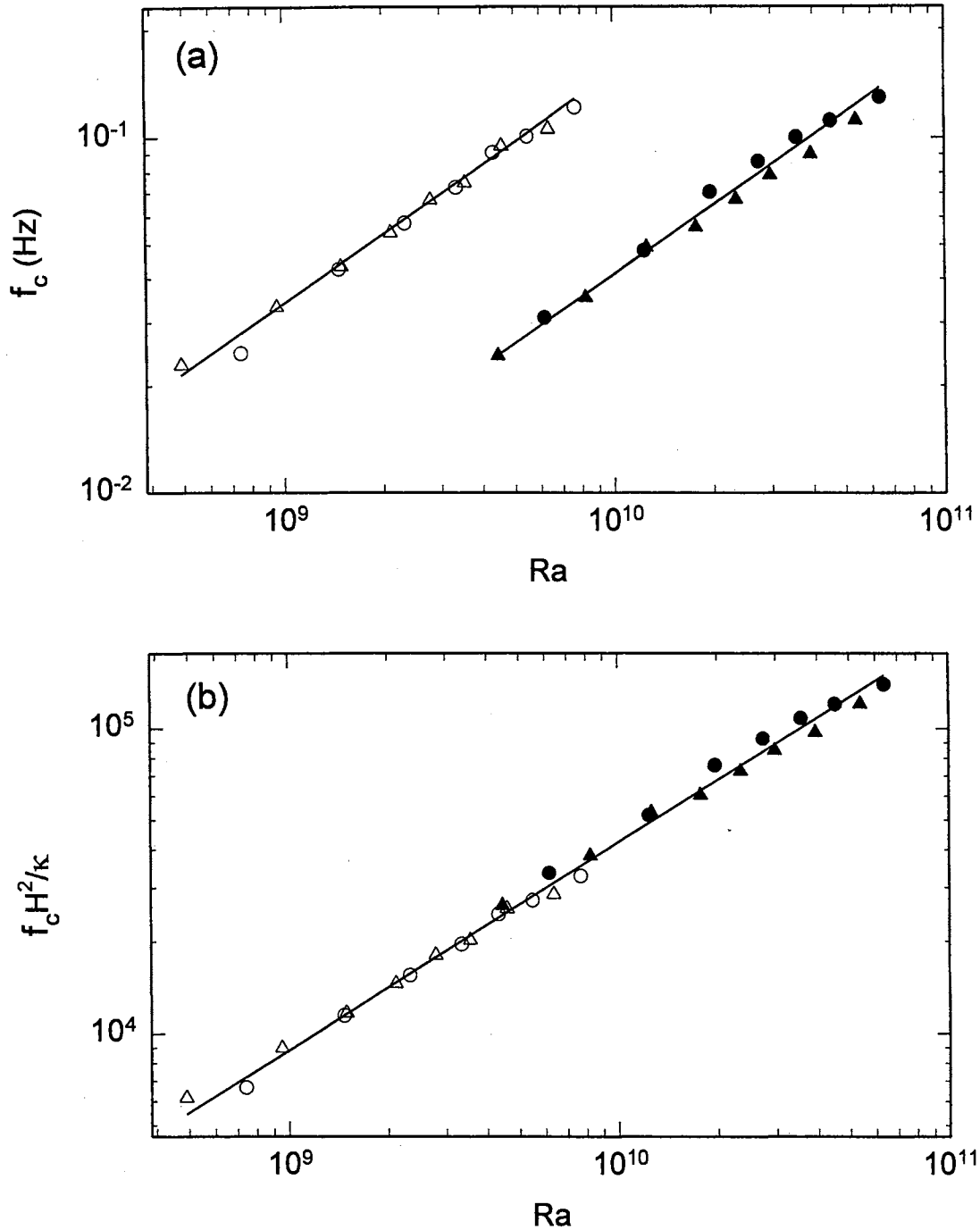


Figure 5.15 (a) Cut-off frequency f_c as a function of Ra in the smooth cells (circles) and in the rough cells (triangles). The solid symbols represent the data obtained from the $A=0.5$ cells, and the open symbols are from the $A=1$ cells. The left solid line is the power law fit $f_c = 4.8 \times 10^{-8} Ra^{0.68}$ and the right solid line shows $f_c = 1.3 \times 10^{-8} Ra^{0.68}$. (b) Normalized cut-off frequency $f_c H^2 / \kappa$ as a function of Ra . The solid line shows the power law fit $f_c H^2 / \kappa = 6.7 \times 10^{-3} Ra^{0.68}$.

where H is the cell height and κ is the thermal diffusivity of the fluid. In the above, we have used the experimental result, $Nu = 0.17Ra^{2/7}$, which was obtained from the same convection cell (see Chapter IV).

Figure 5.15(b) shows the normalized cut-off frequency $f_c H^2 / \kappa$ as a function of Ra . It is seen that the measured $f_c H^2 / \kappa$ in the smooth and rough cells with different aspect ratios can all be superposed onto a single master curve, indicating that the energy dissipation in these cells is determined by the same mechanism. The solid line in Fig. 5.15(b) shows the power law fit $f_c H^2 / \kappa = 6.7 \times 10^{-3} Ra^{0.68}$. The fitted exponent is very close to the calculated one in Eq. (5.3) and the amplitude is off only by a factor of 4. As discussed above, the numerical value of f_c may vary depending on how f_c is extracted. It should be pointed out that because there are several length scales and characteristic velocities involved in turbulent convection, the argument that leads to Eq. (5.3) may not be unique [49, 10, 14]. For example, if one chooses the Kolmogorov cut-off length $\eta \sim (\nu^3 / \varepsilon)^{1/4}$ as l_c and the smallest eddy velocity $v_\eta = (\varepsilon \eta)^{1/3}$ as u_c [51, 52], we have

$$f_c = \frac{v_\eta}{\eta} \approx \left(\frac{\varepsilon}{\nu} \right)^{1/2} \quad (5.4)$$

where ν is the kinematic viscosity of the fluid and $\varepsilon = \nu \langle |\nabla \mathbf{V}|^2 \rangle$ is the energy dissipation rate. Using the Navier-Stokes equation for thermal convection in a fluid layer heated from below, one can get an exact result [3]

$$Ra(Nu - 1) = \frac{\langle |\nabla V|^2 \rangle H^4}{\kappa^2} \quad (5.5)$$

Substituting Eq. (5.5) into Eq. (5.4), we find

$$\frac{f_c H^2}{\kappa} = [Ra(Nu - 1)]^{1/2} \approx 0.41 Ra^{9/14} \quad (5.6)$$

The calculated exponent in Eq. (5.6) is also close to the measured one shown in Fig. 5.15(b), but the amplitude is off by a factor of 60. It becomes clear now that to fully understand the temperature power spectrum $P(f)$, one needs to study the power spectra of velocity fluctuations as well as the temperature gradients.

CHAPTER VI

SUMMARY

Flow visualization and heat transport measurements are first performed in convection cells with rough upper and lower surfaces and the results are compared with those in the smooth cells. The measured heat flux as a function of the Rayleigh number Ra in the rough cells is found to obey a power law with an exponent being the same as that in the smooth cells but the amplitude is increased by more than 76%. The flow visualization reveals that the emission dynamics of thermal plumes over the rough surface is changed completely. It is found that the interaction between the horizontal shear flow due to the large-scale circulation and the rough surface creates a secondary flow (eddies) inside the grooves. This secondary flow together with the large-scale circulation enhance the detachment of the thermal boundary layer near the tip of the rough elements. Because the plume eruption over the rough surface is driven mainly by the large-scale flow rather than the buoyancy force, the vortex ring associated with the buoyancy acceleration disappears and thus most thermal plumes in the rough cell lose their mushroom cap.

To quantitatively characterize temperature fluctuations in turbulent convection, we have conducted systematic local temperature measurements over varying Rayleigh numbers and at various spatial positions near the rough surface. The near-wall temperature measurements together with flow visualization reveal that the emission of

the thermal plumes is greatly enhanced near the tip of the rough elements. The extra thermal plumes detached from the rough elements are responsible for the enhanced heat transport in the rough cells. The local temperature measurements indicate that the thermal boundary layer follows the contour of the rough surface. The boundary layer thickness δ near the tip is found to be reduced considerably, whereas in the groove region δ is increased when compared with that in the smooth cell. The small eddies trapped in the groove region produce a strong mixing effect, which suppresses the emission of the thermal plumes deep inside the groove, and at the same time creates large temperature fluctuations outside the boundary layer. This local dynamic process destroys the temperature homogeneity over the (cold) rough surface and produces a higher surface temperature at the tip of the rough elements. As a result, the rough surface is no longer an isothermal surface any more.

Local temperature measurements are also carried out at the center of the convection cells. The temperature fluctuations at the cell center are characterized by intermittent sharp spikes of variable heights. The measured temperature histogram $H(\delta T)$ in the $A=1$ cell is found to be of a simple exponential form and does not change with Ra , once δT is scaled by its RMS value σ . This scaling behavior suggests that the structure of the turbulent temperature field in the bulk region is invariant with Ra . In the $A=1$ rough cell, the temperature fluctuations are increased considerably, but the measured $H(\delta T)$ exhibits the same exponential shape and scales with $\delta T / \sigma$. This suggests that the structure of the turbulent temperature field in the rough cell remains the same as that in the smooth cell and is invariant with Ra .

Similar to the situation in the $A=1$ cells, the temperature fluctuations in the $A=0.5$ cells are characterized by sharp spikes of variable heights and are of intermittent nature. A new feature found in the $A=0.5$ cells is that the cold and warm spikes are superposed on a base line which changes with time slowly. It has been suggested that the slow base line variation is caused by the fact that the large-scale circulation becomes unstable in the $A=0.5$ cell. Because of the unstable large-scale circulation, the RMS value σ in the $A=0.5$ cells is found to be larger than that in the $A=1$ cells. The temperature histograms in the $A=0.5$ cells show a similar scaling behavior as those in the $A=1$ cells. However, because of the unstable large-scale circulation, the shape of the measured $H(\delta T)$ is no longer of a simple exponential form. Instead, it can be described by a stretched exponential function $H(\delta T) = H_0 \exp[-\kappa(\delta T/\Delta T)^{1.5}]$.

To understand the dynamics at small length scales, we studied the power spectrum $P(f)$ of the temperature fluctuations at the cell center. The lower-frequency part of the measured $P(f)$ exhibits a power-law decay, $P(f) \sim f^{-\alpha}$ with $\alpha \approx 1.3$. In the high frequency region, the measured $P(f)$ drops sharply and can be described by a stretched exponential function $P(f) = P_0 \exp[-(f/f_c)^{0.6}]$, where f_c is a cut-off frequency and P_0 is an amplitude. The measured f_c in the smooth cells obeys a power law $f_c \sim Ra^{-\xi}$, with $\xi = 0.68$. The measured power spectra in the rough cells are found to be of the same shape as those in the smooth cells and the cut-off frequency f_c also remains unchanged. It is found that the normalized cut-off frequency $f_c H^2/\kappa$ in both the smooth and rough cells with different aspect ratios can all be superposed onto a single master curve, $f_c H^2/\kappa = 6.7 \times 10^{-3} Ra^{0.68}$. This indicates that the energy dissipation in

these cells is determined by the same mechanism. There are several different ways to explain the observed scaling behavior of f_c on Ra . To fully understand the temperature power spectrum $P(f)$, one needs to further study the power spectra of velocity fluctuations as well as the temperature gradients.

BIBLIOGRAPHY

1. M.R. Raupach, R. A. Antonia, and S. Rajagopalan, *Appl. Mech. Rev.* **44**, 1 (1991).
2. H. Tennekes and J.L. Lumley, *A First Course in Turbulence*, (MIT Press, Cambridge, MA, 1972).
3. E. Siggia, *Annu. Rev. Fluid Mech.* **26**, 137 (1994).
4. F. Heslot, B. Castaing, and A. Libchaber, *Phys. Rev. A* **36**, 5870 (1987).
5. B. Castaing, G. Gunaratne, F. Heslot, L. Kadanoff, A. Libchaber, S. Thomae, X.-Z. Wu, S. Zaleski, and G. Zanetti, *J. Fluid Mech.* **204**, 1 (1989).
6. X. Wu, L. Kadanoff, A. Libchaber, and M. Sano, *Phys. Rev. Lett.* **64**, 2140 (1990).
7. T. H. Solomon and J. P. Gollub, *Phys. Rev. Lett.* **64**, 2382 (1990).
8. T. H. Solomon and J. P. Gollub, *Phys. Rev. A* **43**, 6683 (1991).
9. P. Tong and Y. Shen, *Phys. Rev. Lett.* **69**, 2066 (1992).
10. A. Belmonte, A. Tilgner, and A. Libchaber, *Phys. Rev. Lett.* **70**, 4067 (1993).
11. A. Belmonte, A. Tilgner, and A. Libchaber, *Phys. Rev. E* **50**, 269 (1995).
12. Y. Shen, K. -Q. Xia, and P. Tong, *Phys. Rev. Lett.* **75**, 437 (1995).
13. S. Cioni, S. Ciliberto and J. Sommeria, *J. Fluid Mech.* **335**, 111 (1997).
14. T. Takeshita *et al.*, *Phys. Rev. Lett.* **76**, 1465 (1996).
15. Y.-B. Xin, K.-Q. Xia and P. Tong, *Phys. Rev. Lett.* **77**, 1266 (1996).
16. X. Chavanne *et al.*, *Phys. Rev. Lett.* **79**, 3648 (1997).
17. E. E. Deluca *et al.*, *Phys. Rev. Lett.* **64**, 2370 (1990).
18. J. Werne, *Phys. Rev. E* **48**, 1020 (1993).
19. J. Werne, *Phys. Rev. E* **49**, 4072 (1994).
20. R. Kerr, *J. Fluid Mech.* **310**, 139 (1996).

21. B. I. Shraiman and E.D. Siggia, *Phys. Rev. A* **42**, 3650 (1990).
22. W. V. R. Malkus, *Proc. R. Soc. Lond.* **A225**, 185, 196 (1954).
23. L. N. Howard, *J. Fluid Mech.* **17**, 405 (1963).
24. Y. -M., Liu and R. E. Ecke, *Phys. Rev. Lett.* **79**, 2257 (1997).
25. S. Ciliberto, S. Cioni, and C. Laroche, *Phys. Rev. E*, **54**, 5901 (1996).
26. K. -Q. Xia and Siu-Lung Lui, *Phys. Rev. Lett.* **79**, 5006 (1997).
27. A. Belmonte, A. Tilgner, and A. Libchaber, *Phys. Rev. E* **51**, 5681 (1995).
28. H. Benard, *Ann. De Chimie et de Physique* **23**, 62 (1901).
29. Lord Rayleigh, *Phil. Mag.* **32**, 529 (1916).
30. D.J. Tritton, *Physical Fluid Dynamics*, second edition (Clarendon Press, Oxford, 1988).
31. A. Khurana, *Physica Today*, p.17, June 1988.
32. G. Zocci, E. Moses, and A. Libchaber, *Physica A* **166**, 387 (1990).
33. Y. Shen, Ph.D. thesis, Oklahoma State University (unpublished), 1996.
34. Y. Shen and P. Tong, *Phys. Rev. Lett.* **76**, 908 (1996).
35. YSI Precision Thermistors, *Yellow Springs Instruments Manual*, Yellow Springs, Ohio, 1977
36. P.G. de Gennes and J. Prost, *The Physics of Liquid Crystals*, second edition (Oxford University Press, Oxford, UK, 1993)
37. S. Cioni, S. Ciliberto, and J. Sommeria, *J. Fluid Mech.* **335**, 111 (1997).
38. H. Tanaka and H. Miyata, *Int. J. Heat Mass. Transfer* **23**, 1273 (1980).
39. Y.T. Chu and R. J. Goldstein, *J. Fluid Mech.* **60**, 141 (1973).
40. D. C. Threlfall, *J. Fluid Mech.* **67**, 17 (1975).
41. T.E. Faber, *Fluid Dynamics for Physicists* (Cambridge University Press, Cambridge, UK, 1995)
42. A. Tilgner, A. Belmonte, and A. Libchaber, *Phys. Rev. E* **47**, R2253 (1993).
43. X.Z. Wu, Ph.D. thesis, University of Chicago (unpublished), 1991.

44. X.Z. Wu and A. Libchaber, Phys. Rev. A 45, 842 (1992).
45. National Instruments Catalogue, National Instruments, Austin, TX, 1998.
46. R. Bolgiano, J. Geophys. Res. **64**, 2226 (1959).
47. A.M., Obukhov, Dokl. Akad. Nauk. SSSR **125**,1246 (1959).
48. M. Sano, X.-Z. Wu, and A. Libchaber, Phys. Rev. A. **40**, 6421 (1989).
49. I. Procaccia *et al.*, Phys. Rev. A **44**, 8091 (1991).
50. Cioni, S., Ciliberto, S., and Sommeria, J., Europhys. Lett. **32**, 413 (1995).
51. A. N. Kolmogorov, C. R. (Dokl.) Acad. Sci. USSR **30**, 301; **31**, 538 (1941).
52. U. Frisch, P. Sulem, and M. J. Nelkin, J. Fluid Mech. **87**, 719 (1978).

VITA

YIBING DU

Candidate for the Degree of

Doctor of Philosophy

Thesis: TURBULENT THERMAL CONVECTION IN A CELL WITH ROUGH
UPPER AND LOWER SURFACES

Major Field: Physics

Biographical:

Personal Data: Born in Taiyuan/Shanxi, China, on June 9, 1966, the daughter of Peizhi Huang and Yuemin Du.
Married Shenghong Yao, January 18, 1989.

Education: Received Bachelor of Science in Applied Physics from Tianjin University, Tianjin, China in July 1985. Received Master of Science in Applied Physics from Tianjin University, Tianjin, China in June 1988. Completed requirements for the Doctor of Philosophy Degree at Oklahoma State University in December 1999.

Professional Experience: Lecturer, Department of Physics, Tianjin Normal University, from March 1988 to August 1994; Teaching Assistant, Department of Physics, Oklahoma State University, from August 1994 to May 1995; Research Assistant, Department of Physics, Oklahoma State University, from May 1995 to May 1999.

Professional Membership: American Physical Society.